POLITECNICO DI MILANO

Scuola di Ingengeria Industriale e dell'informazione

Corso di Laurea Magistrale in Ingegneria Energetica

Numerical analysis of heavy liquid metal heat transfer experiment in a 19-rod bundle with grid spacers

Relatore: Prof. Luca Davide MAROCCO

Correlatore: mag. Ing. Damir RIGLER

Tesi di Laurea di:

Matteo CIABOTTI Matr.801550

Anno accademico 2015-2016

Acknowledgements
Ringraziamenti

Ringrazio prima di tutto la mia famiglia che mi ha sempre supportato sia nei momenti belli che in quelli difficili con tutti i mezzi e in tutte le mie scelte, stando sempre in un piano di confronto e apertura al dialogo.

A mio padre che mi ha sempre indicato la soglia e mostrato il valore della pazienza quando dovevo attraversarla.

A mia madre che mi ha sempre spronato a dare il massimo aiutandomi a capire il valore delle cose che faccio e che sono intorno a me, nei momenti in cui non lo riuscivo a vedere.

Un ringraziamento speciale va al Relatore Prof. Luca Marocco, che ha creduto in me e mi ha dato questa bellissima opportunita di lavorare con lui al KIT spingendomi sempre a dare il massimo.

Thanks to my Tutor Damir Rigler without your support this work would not be possible, I found a colleague and a friend, I hope to meet you again in future and talk with a coffee about past experiences.

Thanks to all the people at the KALLA laboratory this thesis would not be possible with your support, in particular to Prof. T. Wetzel who accepted me in the KALLA team for six month.

Un ringraziamento allargato a tutti gli zii e cugini, quando tornavo da Milano ho sempre ricevuto un'accoglienza più che calorosa dove ho sempre trovato la forza di tenere duro e continuare in questi anni.

A Gigi e Giovi, i fratelli che non ho mai avuto, alla Cami e alla Costi. Siete i migliori cugini con cui ho passato l'infanzia e sono cresciuto, al nostro rapporto che nonostante la distanza rimane stupendo e unico.

Alla "zia" Sonia, le ore passate a studiare in tua compagnia e a divagare sui lavori che portavi avanti negli archivi storici, perchè quelle ore sono state e rimangono sempre bei momenti.

A tutti gli amici che ho trovato a Milano in questi anni di università con cui ho avuto l'opportunita di crescere e confrontarmi.

In particolare al gruppo di studio con cui ho condiviso la stesura della tesi e gli ultimi esami vi ringrazio per il supporto e l'amicizia.

A Conso un collega e un amico, alle nostre serate e chiamate infinite che, tra gossip e studio mi hanno permesso di arrivare fino a questo punto.

A Teo e a tutti gli amici di Fano con cui, nonostante la distanza, mi sono sempre ritrovato in ottimi rapporti.

Table of contents

Sommario 1

Abstract 2

1. Introduction 3

1.1. Four generation of nuclear power technology 3

1.2. Liquid metal as a heat transfer fluid 4

1.3. Activity performed at KALLA 4

1.3.1. Main spacer families 5

1.4. Scope and content 6

2. Problem description 7

2.1. Experimental set up 7

2.1.1. The LBE test loop 7

2.1.2. Test section 8

2.2. Instrumentation 10

2.2.1. Temperature 10

2.2.2. Thermal power 10

2.3. The heat transfer in liquid metals 11

2.3.1. The Reynolds analogy 13

2.4. Problem description 17

3. The turbulence models 19

3.1. Turbulence modeling theory 19

3.2. Flow field turbulence models 20

3.2.1. Low Reynolds models 20

3.2.2. $k - \varepsilon\ AKN$ 21

3.2.3. $k - \omega\ SST$ 23

3.2.4. $k - \varepsilon - v^2 - f$ 25

3.3. Thermal turbulence models 26

3.3.1. X. Cheng and N.I. Tak turbulent Prandtl correlation 27

3.3.2. W. Kays turbulent Prandtl number 28

3.3.3. $k_\theta - \varepsilon_\theta$ model 28

4. The computational domain 31

4.1. Meshing the domain 31

4.1.1. Structured-grids 31

4.1.2. Unstructured-grids 32
4.2. Domain and boundary conditions 33
4.2.1. Central rod of the bundle 36
4.2.2. Complete grid 39
4.3. Fluent set up 43
5. Results 45
5.1. Validation of $k - \varepsilon - k_\theta - \varepsilon_\theta$ 45
5.2. Central bundle rod results 51
5.2.1. GCI study 59
5.3. Complete mesh results 67
6. Conclusions 77
Appendix A 79
Appendix B 87
Appendix C 88
List of figures 92
List of tables 95
Bibliography 96

Sommario

Nel presente lavoro di tesi è illustrata l'analisi numerica di uno scambiatore nucleare a fascio di barre distanziate da spaziatori a griglia e raffreddato con metallo liquido. Il regime di flusso del refrigerante è fortemente turbolento ed introduce forti stress meccanici alle barre le quali, caratterizzate da un'alta densità di potenza, potrebbero entrare in contatto e generare un aumento locale di temperatura. Tale aumento potrebbe eccedere il limite di sicurezza imposto dai materiali.

Lo spaziatore a tale scopo fissa le barre nella posizione definita in campo di progetto, ma introduce una rilevante perturbazione del flusso alterando consistentemente lo scambio termico identificato dal gruppo adimensionale di Nusselt. La campagna di dati sperimentali riguardanti lo scambiatore in esame è stata fornita del laboratorio KALLA dell'Istituto di Tecnologia di Karlsruhe (KIT) in [1]. Tali dati vengono usati nel presente lavoro di tesi per la validazione dell'analisi numerica.

Il meccanismo di scambio termico dei metalli liquidi è peculiare e differisce da quello dei fluidi più comuni aventi un numero di Prandtl vicino o superiore all'unità. L'analogia di Reynolds non è più valida per i metalli liquidi e di conseguenza diversi metodi per il numero di Prandtl turbolento sono stati utilizzati ed analizzati in questa tesi. Un modello a quattro equaizoni recentemente proposto in [2] e messo a punto per l'analisi numerica dei metalli liquidi. Sono state inoltre utilizzate due correlazioni per definire il numero Prandtl turbolento in [3] e in [4], accoppiate con tre modelli per il calcolo della viscosità turbolenta.

Le simulazioni svolte sono compiute su un singolo spacer. Il primo caso riguarda un fascio infinito di barre distanziate con lo spaziatore. Il secondo caso è la geoemetria completa dello spaziatore comprendente anche il tubo di contenimento del reattore il quale, è considerato adiabatico. I risultati così prodotti al variare del numero medio di Pèclet sono confrontati con i dati sperimentali tramite numeri di Nusselt e temperature adimensionali.

Parole Chiave: Metalli liquidi, CFD, Convezione turbolenta, Fascio di barre, Spaziatore, Scambio di calore, Scambiatore di calore.

Abstract

The increasing demand of energy requires a major supply which, coupled with a higher environment sensibility leads to study more sustainable energy production systems. The THINS project [5], in the nuclear power research area proposes several innovative four generation reactors with enhanced safety, economics, sustainability and non-proliferation features which need to be developed.

The KALLA laboratory of the Karlsruhe Institute of Technology (KIT) in Germany took part on the THINS project in developing thermal hydraulic feature on a nuclear reactor with ADS (accelerator driving system) cooled by liquid metals. The reactor design investigation leads to study the thermal dynamics performing several experiments.

In this thesis based on the experimental data produced by the KALLA laboratory is proposed a CFD study on the liquid metals heat exchange in a 19 rod bundle with grid spacers in [6]. A computational fluid domain has been developed in several steps simulating a single grid spacer to achieve a better understanding of the heat transfer phenomena happening inside the test section used at the KALLA laboratory.

The heat transfer analysis proposes a study on the main flow perturbation produced by the grid spacer which, is necessary to assure the rod stiffness avoiding the rods contacts which could generate a temperature increase over the materials security limits.

The analysis has been carried out for several flow regimes. It starts first from an infinite rod bundle with grid spacer which simulate the central rods of the bundle. Than the second step it consists on the discretization of a complete grid spacer with the external adiabatic wall, to realize differences on the heat exchange, how profiles vary from the central rod to the peripheral ones.

The numerical analysis is also complicated by the fact that the heat transfer mechanism of liquid metals differs from that of ordinary fluids. Consequently, the Reynolds analogy cannot be applied to these fluid flows.

A recently proposed four-equation turbulence model in [2], takes in account the dissimilarities between the thermal and dynamical turbulence fields. It has been selected to perform a part of the numerical analysis. It consists on two additional transport equations, namely one for the temperature variance and one for its dissipation rates, have been solved to determinate the turbulent thermal diffusivity. The turbulence model has been implemented on through User Defined Function in Fluent v.15 CFD code.

Two other semi empirical correlations computing the turbulent Prandtl number using the dynamical field properties have been launched using three different flow turbulent models. The results collected were thus compared with the experimental data, in order to find the best computational set up data fitting.

Keywords: Liquid Metals, CFD, Turbulent Convection, Rod Bundle, Spacer, Heat transfer, Heat exchanger.

Chapter 1

1. Introduction

1.1. Four generation of nuclear power technology

The increasing demand of energy requires a major supply that coupled with a higher environment sensibility leads to study more sustainable energy production systems. In the nuclear power research area there are several innovative four generation reactors using different coolants, kinds of nuclear reactions, and fuels [7], very high temperature reactor (VHTR), gas cooled fast reactor (GFR), sodium-cooled fast reactor (SFR), lead-cooled fast reactor (LFR), supercritical-cooled fast reactor (SFR), molten salt reactor (MSR).

The nuclear waste reduction is an important aspect of the new generation reactors in order to meet the demand of a more sustainable energy production. Extensive study in the last years brought to light the promising way of partitioning and transmutation the nuclear waste using accelerator driven system ADS [8].

Thermal hydraulics is than recognized as one of the main key aspects to develop the new reactor systems. The research is focused on unconventional heat transfer fluid. New sub-channel geometries are tested, which brings to new arrangements and different primary circuit layouts. The new working fluids have different behavior, microscopic and macroscopic that need to be investigated through new models, computational simulations and experiments [5].

In this scenario the European project THINS (www.ifrt.kit.edu/thins/) was developed from 2010 to 2014. It is a partnership between 24 institutions. The article European activities on crosscutting thermal-hydraulic phenomena for innovative nuclear systems [5], reports the THINS project main features, focused to develop the nuclear power reactor of generation IV with enhanced safety, economics sustainability and non-proliferation features. The design of new and innovative reactor cores require several experiments and computational simulations investigating the fluid dynamics to find the best solution for the fuel assembly.

The main working features of the project are:

- Advance reactor core thermal-hydraulics
- Single phase mixed convection
- Single phase turbulence
- Multi-phase flow
- Code coupling and qualification

Inside this project, the Karlsruhe Liquid Metal Laboratory (KALLA) of the Karlsruhe Institute of Technology (KIT) in Germany, was performed an experiment. A test section was built to study the behavior of lead bismuth eutectic (LBE) cooling an electrically heated 19-pin rod bundle with three grid spacers that are mounted in the existing THEADES LBE loop in Fig. 1.1.

Fig. 1.1 THEADES LBE loop at KALLA laboratory, [9].

1.2. Liquid metal as a heat transfer fluid

The first nuclear power facilities using liquid metals date back around 1950s, during the Cold War, USA and USSR started their research programs to power nuclear submarines. Both nations developed simultaneously pressurized water reactor and liquid metal cooled reactor. URSS started its work with lead-bismuth eutectic as a coolant while USA opted for sodium, the results was a prototype of submarine called 'Sea Wolf' that has been constructed by the USA. The only problem is that sodium reacts exothermically with water yielding sodium hydroxide (NaOH) and hydrogen gas. Thus the explosion risk didn't justify the use. USA studied also lead-bismuth coolants, but their high corrosion rate and the impurities contamination cause problems related to their control and doesn't repay the advantages. Despite all disadvantages studies were carry out in background till nowadays, where the technology allows more economical solutions.

There are many advantages of liquid metals compared to the more common coolants used in the primary circuit of nuclear application such as water or air. In particular considering the alloy lead-bismuth eutectic LBE (Pb is 44%, Bi is 56%) it has an high boiling point of (1670°C) which allows a low pressure in the primary circuit with an operating temperature of 400-500°C. The materials used to contain LBE such as the vessel are subjected to a lower mechanic stresses compared for example to supercritical or subcritical reactor cooled by water. The large thermal conductivity λ allows to a more efficient heat exchange in the primary circuit. The LBE low viscosity requires a lower hydraulic head from the pumps. In case of leakage from the primary circuit there is no combustion or explosion caused from the contact of LBE with air or water. All those conditions work together to meet more safety requirements and more efficient systems [10].

1.3. Activity performed at KALLA

In this scenario of increased interest in advanced fast reactor concept and accelerator driven-system, with the aim to achieve a better understanding on the thermal-hydraulic behavior of heavy liquid metals in a fuel-assembly of nuclear reactors representative geometries, the KALLA laboratory [1] performed an experiment.

It consists of an electrical heated 19-pin hexagonal rod bundle cooled by LBE in a typical reactor operating conditions in terms of temperature power density and mass flow rate. This rod bundle include three grid-spacers which both keep the rods in position and provide support for detailed temperature measurement at each axial position. The thesis is based on this particular experiment. It provides support to validate a numerical models. Database in this kind of application are not extensive and the experiments are really important but also expensive due to several issue aspects. Thus numerical models give support to an accurate and reliable planning.

The kind of reactor and its design is one of the project keys components, due to rods proximity, their high thermal power and completely turbulent developed fluid dynamic velocity profile, rod bundle undergoes severe mechanical stresses. Rods without any mechanical support may come in contact causing a coolant lack. In the contact zone there'll be a wall temperature increase over the safety limits imposed by materials. To supply this problem spacers provide keeping distance between fuels supports.

1.3.1. Main spacer families

There are two main spacer families. One is the helical spacer wires, it consists on a metal wire helically wrapped around each rod of the bundle providing the contact zones to the adjacent rods in Fig. 1.2.

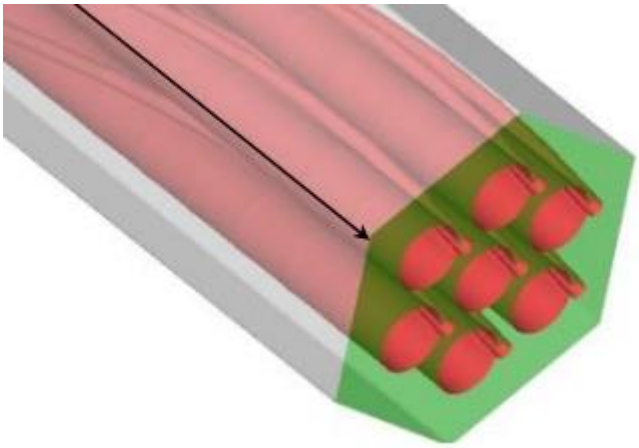

Fig. 1.2 7 Wire wrapped rods in a hexagonal lattice, [11] the black arrow is the main flow direction

Helical wire wrapped spacer introduces a periodical variation of the main flow properties. Taking a domain portion far enough from the rod bundle inlet section to be thermally and hydrodynamically fully developed, the proprieties expressed in function of the axial coordinate of the main flow direction, like friction factor and Nusselt number can be divided in to a constant value and a fluctuating one depending on the helical pitch, rods number and lattice distribution [12]. Fluctuations can be considered not consisted compared to the main constant quantities depending from case to case.

The second kind are the spacer grids like in Fig. 1.3. In the picture the hexagonal holes where are inserted rods are visible. The small dimples three for each hole are the only portion of spacer in contact with the rod wall. Dimples keep every rod in the correct position.

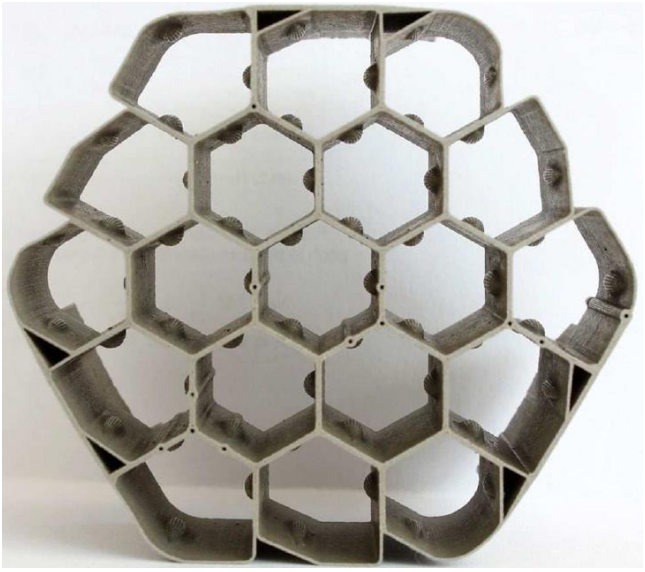

Fig. 1.3 Frontal view of the grid spacer used in [1].

These spacers represent only a small portion of the rod main axial length, in this specific case are three grid spacers in the entire rod bundle [1].

This kind of spacer introduce a concentrated pressure loss, instead of the distributed of the previous one. In the area close to the spacer the flow field is characterized by vortices and recirculation areas [13]. The thermal proprieties like the temperature and the Nusselt number have an exponential growth upstream the spacer followed by an exponential decaying trend [14]. The magnitude of this behavior depends from the main flow properties and the geometry.

1.4. Scope and content

Many authors developed semi-empirical correlations to analyze the heat transfer of liquid metals in a triangular lattice assembly in fully developed flow without spacers. They are briefly cited with their main conclusion in [15]. The spacer introduces significant changes on the main flow characteristic and on the heat exchange as descripted in Paragraph (1.3.1). Starting from the experiment performed at the KALLA laboratory in [1] many authors simulated the same phenomena using system code TRACE [14], and CFX [6].

This work pursues the aim to study the heat transfer phenomena of LBE using the CFD software Fluent v.15 and compare the results with the experimental data in [1]. Using existing models and correlations already developed, they are tested in the in the specific grid spacer geometry in Fig. 1.3. This work is focused on the assessment of several meshes to reproduce the spacer phenomena which characterize the heat exchange. Than it follows the error investigation to asses the computational domain independence.

Chapter 2

2. Problem description

2.1. Experimental set up

The experimental set up description from the instrumentation to the derivation of the main quantities is cited from [1]. Here follows first the description of the THEADES LBE loop, second the section test and at last the derivation of the main quantities used as a reference values in this thesis.

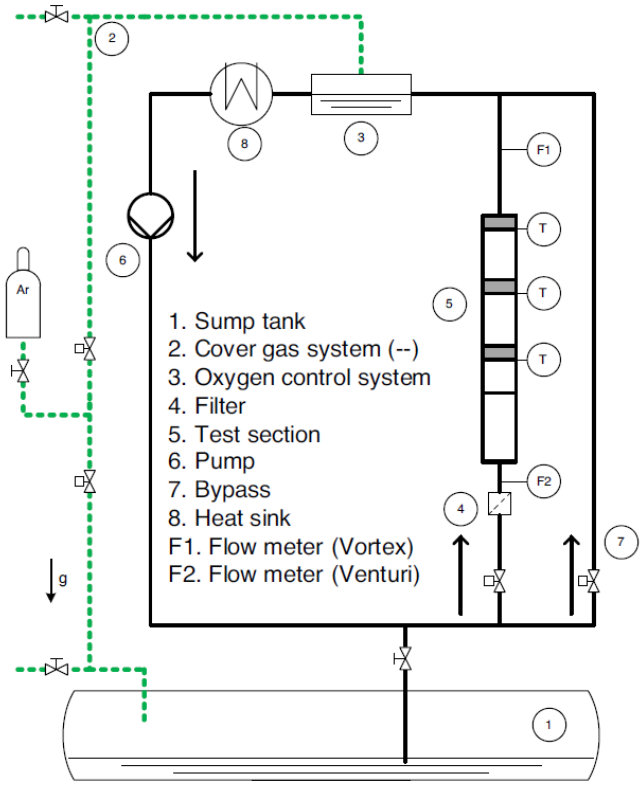

Fig. 2.1 Schematic representation of the THEADES LBE loop, its set-up for this experiment [1].

2.1.1. The LBE test loop

The experiment is performed at the KALLA laboratory [9] using the THEADES loop schematically represented in Fig. 2.1. Starting from the position 1 a sump tank contains the complete LBE stock, it amounts to $42\ tons$. The procedure to use the instrumentation consist in a loop preheating up to $200°\ C$, to avoid the solidification of LBE. Pressurizing the sump tank with the argon from the gas system in position 2 is possible to fill the THEADES loop with liquid metal. The inverse action allows to empty the loop .In case of emergency, opening all the valves, the loop disposition allows to drain all the LBE into the sump tank only with the Gravity force effect. In position 3 there is an oxygen control, it needs to prevent the lead oxide formation and the excessive corrosion rate. These are the conditions for the steady state operations up to $450°C$.

A filter in position 4 prevent the contamination of the test section located in position 5 by the lead oxide. A centrifugal pump is located in position 6, it allows a maximum volumetric flow rate of $42m^3/h$, in order to have a better flow rate control. In position 7 there is a bypass line controlled with by a valve. The heat sink in position 8 it is a an exchanger which use air as a coolant and have a maximum capacity of $500kW$. In position F1 and F2 are placed respectively a vortex flow meter and a Venturi one, in order to have an high measurement accuracy in a wide flow rates range [1].

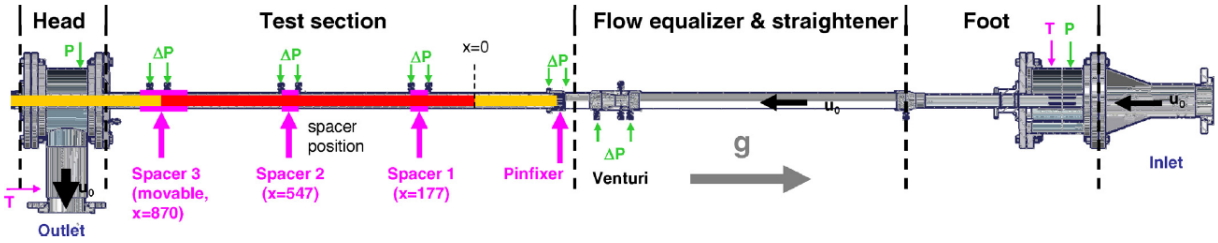

Fig. 2.2 Side view of the test section from [1].

2.1.2. Test section

Fig. 2.2 is the test section side view, it is composed by 19 rods inside an hexagonal pipe. Rods are located on a triangular lattice. The main flow is directed against the gravity, from the inlet follows an equalizer to stabilize the flow before the measurement with the Venturi flow meter, in order to obtain a more homogenous flow distribution over the section and thus a more accurate reading from this sensor. Downstream the Venturi nozzle a pin fixer keep the 19 rods in their position, there is also a pressure sensor to measure the pressure loss across the pin fixer. At $x = 0$ starts the heated zone, three grid spacers follows placed at $x_{sp,1} = 177mm$, $x_{sp,2} = 547mm$, and $x_{sp,3} = 870mm$. Across each spacer a pressure sensor measure the pressure loss of each one. Grid spacers give also support to the thermocouples which are placed in a plane upstream each spacer inlet section, orthogonally to the main flow direction. The third spacer is movable from its reference position to have a deeper understanding of the phenomena happening inside the section test.

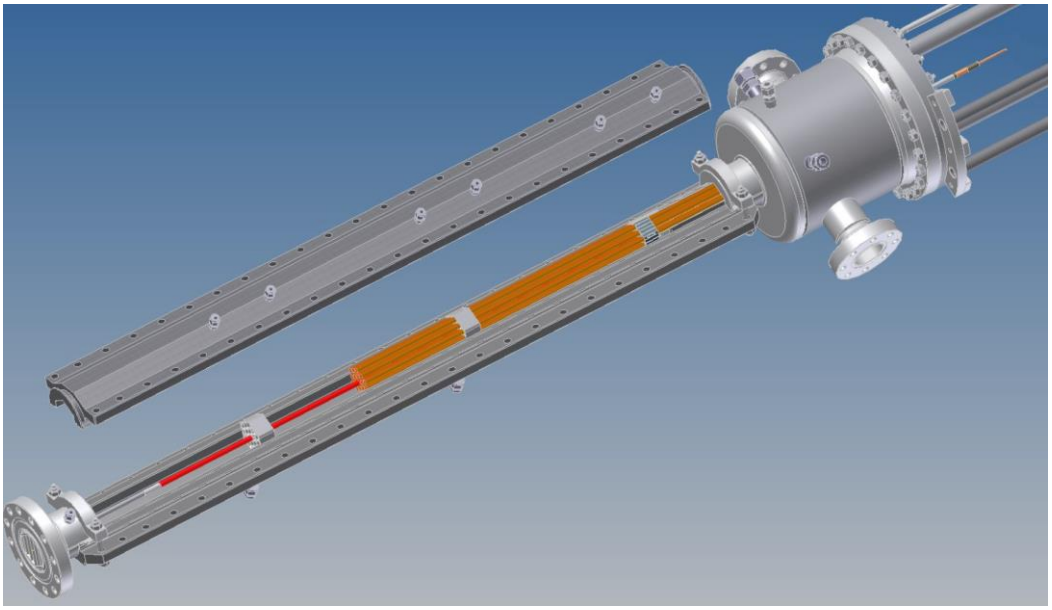

Fig. 2.3 Exploded view of the test section [1].

Fig. 2.3 is an exploded view of the test section, all rods except the central one are trunked. Table 2.1 gives the main technical parameters of the section test.

Table 2.1 Geometrical parameter of the section test [1].

Dimension	Symbol	Value
Heated rods		
Rod outer diameter	d	8.2mm
Rod total length	L_{tot}	1275mm
Rod heated length	L_{heat}	870mm
Triangular array of 19 rods		
Distance between rod centers (pitch)	p	11.48mm
Pitch-to-diameter ratio	p/d	1.4
Minimum distance to the channel wall	W	1.716mm
Hexagonal flow channel		
Apothem	A	25.7mm
Curvature at the corners	R	3mm
Flow area	A_{bdl}	1281.71mm^2
Wet perimeter	P_{bdl}	665.8mm
Hydraulic diameter	$d_{h,bdl}$	7.70mm
Inner sub channel		
Flow area	A_{sch}	30.66mm^2
Wet perimeter	P_{sch}	12.88mm
Hydraulic diameter	$d_{h,sch}$	9.52mm
Grid spacers		
Length	L_{sp}	25mm
Solidity	ϵ	0.29

2.2. Instrumentation

The instrumentation installed in the THEADES loop is necessary to control the section test boundary conditions and its correct operation. In the next paragraph is descripted the section test instrumentation which is useful to obtain the data used in this thesis. In particular are information about thermocouples and the thermal power control which is dissipated by the rods.

2.2.1. Temperature

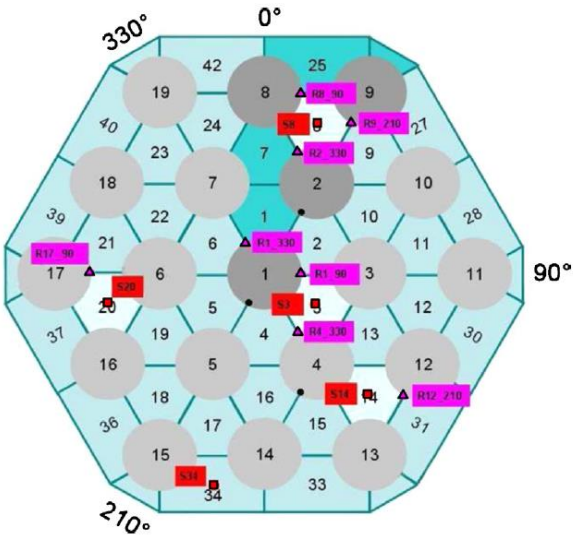

Fig. 2.4 Schematic representation of the thermocouples in the measuring plane upstream the three spacers [1].

46 thermocouples are used in the test section. To measure temperature at the entrance and exit two thermocouple are placed upstream and three downstream of the test section. Fig. 2.4 is the schematic thermocouple representation inside the measuring plane $2{,}5\ mm$ upstream each spacer. The magenta triangles indicate 24 thermocouples (8 in each spacer) placed to measure the heated wall temperature from outside the rod.

The fluid temperature is measured from thermocouples represented on the red squares, placed at the sub channels center. Five sub-channels, including a central channel, three symmetrical ones in the first ring and one in the edge are considered for the first two spacers. Four measurement are allowed in the third spacer due to space limitations. These thermocouples are placed as the same level as the measurement for the wall temperature from outside.

The black circles are three thermocouples only in the third spacer placed to measure the wall temperature from inside the rod, but in this thesis data from these thermocouple are not used.

2.2.2. Thermal power

Rods are built to dissipate uniformly heat flux longitudinally and circumferentially. A direct current-power supply powers the rods. Therefore, measuring independently voltage and current, the electrical power applied to the test section is obtained. From the experiments, it was noticed

that this value exceeds the thermal-energy balance results, presumably due to the power losses (both thermal and electrical) outside the test section [1].

2.3. The heat transfer in liquid metals

Table 2.2 Proprieties of Air, Mercury, and Water at 20°C.

		Mercury	Air	Water
ρ	kg/m^3	13 579	1.205	998.3
c_p	kJ/kgK	0.139	1.005	4.183
λ	W/mK	8.69	0.026	0.598
ν	(m^2/s)·10^{-6}	0.114	15.11	1.004
Pr		0.0249	0.71	7.02

Liquid metals are characterized by a higher thermal conductivity ($\lambda[W/mK]$) and a lower specific heat capacity ($cp[J/kgK]$) compared to the other heat transfer media. Table 2.2 gives an example of common fluids like air and water against mercury, the properties are measured at $20°C$, the kinematic viscosity of the firsts two $\nu = \mu/\rho \ \ [m^2/s]$ is much smaller. By combining thermal conductivity with the specific heat capacity is possible to obtain the characteristic number called Prandtl number Pr in Eq.(2.1). Thus in heat transfer problems it is an essential non-dimensional parameter

$$\mathrm{Pr} = \frac{c_p \cdot \mu}{\lambda} = \frac{\nu}{\alpha} \tag{2.1}$$

Prandtl number represents the weight of the momentum transport coefficient to that of thermal energy. In case of liquid metals is much smaller like showed in Table 2.2.

Prandtl number appears in the non-dimensional form of the energy equation. It is one of the conservation equations together with the continuity, and the momentum equation. These equations are used to solve the flow and the temperature fields. Liquid metals belong to the Newtonian Fluids category, (the viscous stressed are proportional to the deformation rates). They can be considered incompressible ($\rho = const.$). Here the dimensional transport equations:

$$\vec{\nabla} \cdot \vec{U} = 0 \tag{2.2}$$

$$\frac{D\vec{U}}{Dt} = \vec{f} - \frac{1}{\rho}\vec{\nabla}p + \nu\nabla^2\vec{U} \tag{2.3}$$

$$\rho c_p \frac{DT}{Dt} = \lambda\nabla^2 T + \mu\phi \tag{2.4}$$

$$\phi = 2\left[\left(\frac{\partial u}{\partial x}\right)^2 + \left(\frac{\partial v}{\partial y}\right)^2 + \left(\frac{\partial w}{\partial z}\right)^2\right] + \left(\frac{\partial v}{\partial x} + \frac{\partial u}{\partial y}\right)^2 + \left(\frac{\partial w}{\partial y} + \frac{\partial v}{\partial z}\right)^2 + \left(\frac{\partial u}{\partial z} + \frac{\partial w}{\partial x}\right)^2 \tag{2.5}$$

Eq.(2.2) is the continuity, Eq.(2.3) is the momentum transport, and the last Eq.(2.4) is the energy transport. Multiplying and dividing coefficients introducing also characteristic velocities, temperature and length are obtained the non-dimensional forms, respectively:

$$\vec{\nabla}^* \cdot \vec{U}^* = 0 \tag{2.6}$$

$$\frac{D\vec{U}^*}{Dt} = -\vec{\nabla}^* p^* + \frac{1}{Re}\nabla^{*2}\vec{U}^* \tag{2.7}$$

$$\frac{DT^*}{Dt} = \frac{1}{RePr}\nabla^{*2}T^* + \frac{Ec}{Re}\phi^* \tag{2.8}$$

The quantities marked by * are non-dimensional, Ec is the Eckert number and expresses the relationship between the flow kinetic energy and the enthalpy, it is negligible for incompressible fluids. If the pressure gradient can be also considered negligible, there is an analogy in the momentum equation Eq.(2.7) and the energy equation Eq.(2.8). The resulting temperature profile and velocity profile, with these specific approximations, will be directly proportional, connected by a constant which is known as the Prandtl number.

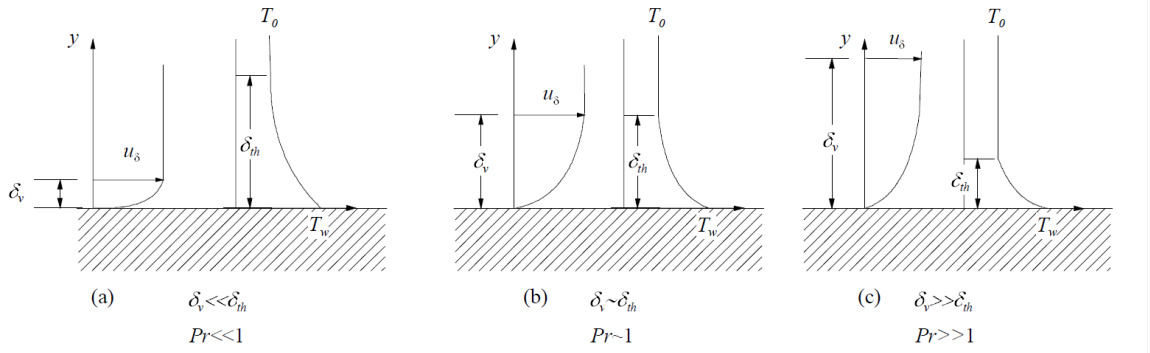

Fig. 2.5 Illustration of the influence of the Prandtl number on the magnitude of the viscous and thermal boundary layers in a two dimensional flow over a plate with constant wall temperature [16]

Like shows Fig. 2.5 with a Prandtl number close to unity the profiles are the same, this is called Reynolds analogy and it is not valid for liquid metals where $Pr \ll 1$ rather in the case of water or air.

2.3.1. The Reynolds analogy

The CFD analysis aim to solve the conservation equations presented in Paragraph 2.3 to obtain a velocity and temperature field. But a problem occurs because these equations have a non-linear term which can be analytically solved only in few cases. Thus CFD approach is based on a numerical solutions, it needs a spatial and temporal discretization, and the solution requires a domain mesh.

The flow inside the rod bundle is turbulent. Turbulence structures are eddies, their formation process begin subtracting energy from the main flow, thus the biggest eddies are formed, with a dimension comparable to the characteristic length of the geometry $l[m]$, these largest eddies are dominated by inertia effects and viscous effects are negligible. They can be considered inviscid and they conserve their angular momentum. Through a process called energy cascade the biggest eddies are divided in to smaller ones, their radius decreases and the angular velocity increases for the momentum conservation. The smallest representative scale is the Kolmogorov scale: $\eta \ll l\,[m]$, the smallest eddies kinetic energy is thus converted into internal energy with the viscous effects which are dominant in these scales [17].

The Reynolds number is a non-dimensional number it represent the ratio between the convective momentum transport and the laminar one, it indicates the turbulent intensity and it can be related to the ratio of the biggest and the smallest spatial scale:

$$\frac{\eta}{l} = Re_l^{-3/4} \tag{2.9}$$

High turbulent flows require a very fine discretization to catch the smallest scale and the computational effort is too high. The solution to this problem is to solve an other equations set derived form of the Eq.(2.6), (2.7), (2.8) decomposing the variables into a mean value and a fluctuating one, using Eq.(2.10). It is a time average which results are expressed in Eq. (2.11), (2.12), (2.13).

$$\begin{aligned} \varphi(\vec{x},t) &= \overline{\phi}(\vec{x}) + \varphi'(\vec{x},t) \\ \overline{\phi}(\vec{x}) &= \frac{1}{\Delta t}\int_t^{t+\Delta t} \varphi(\vec{x},t) \end{aligned} \tag{2.10}$$

$$\frac{\partial \overline{U}_i}{\partial x_i} = 0 \tag{2.11}$$

$$\frac{\partial \overline{U}_i}{\partial t} + \overline{U}_j \frac{\partial \overline{U}_i}{\partial x_i} = -\frac{1}{\rho}\frac{\partial \overline{p}}{\partial x_i} + \frac{\partial}{\partial x_i}\left(\nu \frac{\partial \overline{U}_i}{\partial x_j} - \overline{u'_i u'_j}\right) \tag{2.12}$$

$$\frac{\partial \overline{T}}{\partial t} + \overline{U}_i \frac{\partial \overline{T}}{\partial x_i} = \frac{\partial}{\partial x_i}\left(\alpha \frac{\partial \overline{T}}{\partial x_i} - \overline{u'_j T'}\right) \tag{2.13}$$

These equation, Eq.(2.11), (2.12), (2.13), are referred to the mean flow than require a coarser discretization in space and time. The new terms that appear in these equations are the turbulent stresses or Reynolds tresses Eq.(2.14) and the turbulent heat flux Eq.(2.15).

$$\tau_{ij}^{t} = \rho\, \overline{u'_i u'_j} \tag{2.14}$$

$$q''_t = -\rho\, c_p\, \overline{u'_j T'} \tag{2.15}$$

These quantities need other transport equations to be solved and find the solution of the conservation equations. The Boussinesque hypothesis is used in several models, also in the ones in this thesis, it is a way to compute the Reynolds stresses assuming that they are proportional to the mean flow rate deformation. The proportionality constants are the turbulent viscosity μ_t, and the turbulent thermal diffusivity α_t, Eq.(2.16), (2.17). These are the two quantities computed by the turbulence models.

$$\frac{\tau_{ij}}{\rho} = \nu \left(\frac{\partial \overline{U}_i}{\partial x_j} + \frac{\partial \overline{U}_j}{\partial x_i}\right) \longrightarrow \frac{\tau_{ij}^{t}}{\rho} = \nu_t \left(\frac{\partial \overline{U}_i}{\partial x_j} + \frac{\partial \overline{U}_j}{\partial x_i}\right) - \frac{2}{3} k \delta_{ij} \tag{2.16}$$

$$\frac{q''_j}{\rho c_p} = \alpha \frac{\overline{T}}{\partial x_j} \longrightarrow \frac{q''_{jt}}{\rho c_p} = \alpha_t \frac{\partial \overline{T}}{\partial x_j} \tag{2.17}$$

The following Chapter will explain the models that compute these two quantities. The Reynolds analogy states that $\nu_t = \alpha_t$, with these quantities can be defined a turbulent Prandtl number in Eq.(2.18). For common heat transfer fluids have the turbulent Prandtl number is close to unity or is generally smaller but for liquid metals is greater than the unity stating the different heat transfer mechanism.

$$Pr_t = \frac{\mu_t}{\rho\, \alpha_t} = \frac{\nu_t}{\alpha_t} \tag{2.18}$$

The turbulent viscosity and the turbulent thermal diffusivity have both time and space scale which are respectively similar under the Reynolds analogy hypothesis. These scales are not similar for liquid metals.

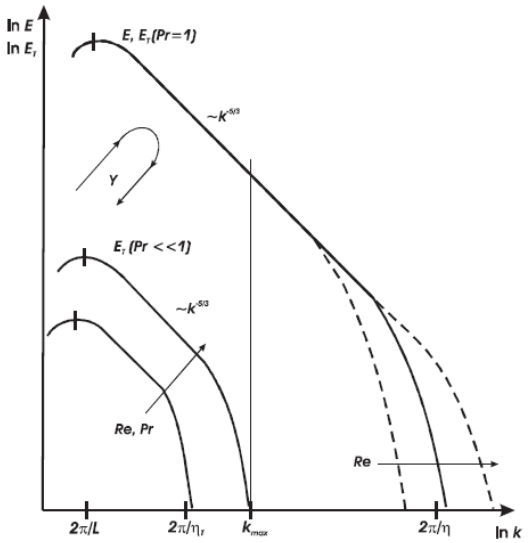

Fig. 2.6 Sketch of three dimensional energy spectra E(k) for velocity fluctuations and temperature fluctuations $E_T(k)$ in a forced channel flow at Pr<1, [18].

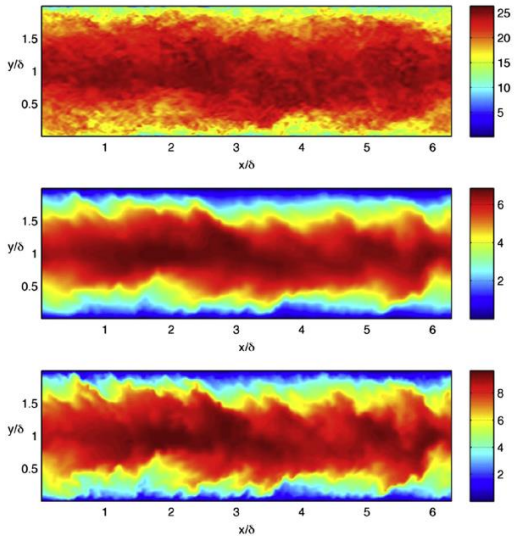

Fig. 2.7 LES at $Re_\tau = 2000$: Visualization of the instantaneous velocity field (top) θ field at Pr=0.01(middle) and at Pr=0.025(bottom) in an arbitrary x-y plane, all at the same time, [19].

Fig. 2.6 shows the energy spectra $E(k)$, as a function of the wave number $k = 2\pi/L$, L is the eddies wavelength. The spectral energy is the turbulent structures energy assigned respectively to the velocity fluctuations and to the temperature fluctuations. From the figure is clear that the largest eddies have the biggest energy amount that constantly decreases with the eddies dimension reduction.

The figure shows at low Prandtl number the temperature fluctuations are damped strongly at small scales due to the high thermal diffusivity which characterize the liquid metals. The biggest wavenumber where $E_T(k)$ is still significant is much smaller compared to the $E(k)$ evaluated at the same wavenumber. Taking the same turbulent spatial scale, the energy associated to the velocity fluctuations is much relevant compared to the temperature fluctuations.

Fig. 2.7 shows the instantaneous velocity and temperature field for two Prandtl number and is easily visible the complexity of the velocity field compared to the temperature field. The velocities shows much smaller turbulent structures, compared to the remaining two.

A brief explanation, considering a 2D shear flow having $\overline{U}_2 = 0$, Fig. 2.8

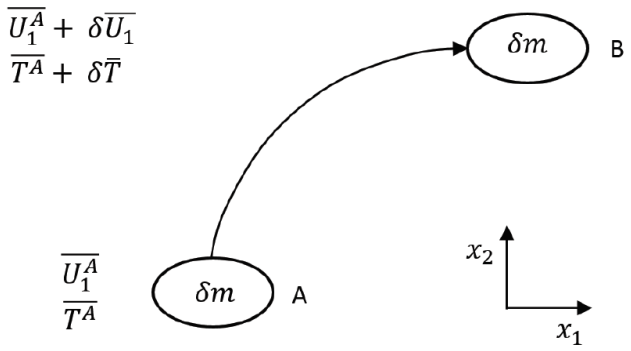

Fig. 2.8 Fluid packet moving in a 2D flow with $\overline{U}_2 = 0$

Considering δm an infinitesimal fluid parcel following its trajectory from A to B due to the turbulent fluctuations of velocity $\overline{u'^2_2}$. Momentum and energy change along the movement and in the position B the parcel is in equilibrium with the fluid around. In the final position of δm B the velocity and temperature are: $\overline{U}_{1B}^{\delta m} = \overline{U}_{1A}^{A} + \delta\overline{U}_1$ and $\overline{T}_B^{\delta m} = \overline{T}^A + \delta\overline{T}$. By assuming that the process take place continuously, the effective velocity in x_2 direction is proportional to $\overline{u'^2_2}$, $\left(C\sqrt{\overline{u'^2_2}}\right)$. The turbulent shear stress and heat flux are equal to the net rate $x_1 - momentum$ and energy across an area parallel to the x_1 direction, respectively:

$$\tau_t = C\sqrt{\overline{u'^2_2}}\rho\delta\overline{U}_1 \tag{2.19}$$

$$q''_t = C\sqrt{\overline{u'^2_2}}\rho c\delta\overline{T} \tag{2.20}$$

Considering l_{mix} small compared to other dimensions of the system, only the first term can be retained in the Taylor expansion of $\delta\overline{U}_1$ and $\delta\overline{T}$, obtaining then:

$$\frac{\tau_t}{\rho} = C\sqrt{\overline{u'^2_2}}\rho l_{mix}\frac{d\overline{U}_1}{dx_2} \tag{2.21}$$

$$\frac{q''_t}{\rho c_p} = C\sqrt{\overline{u'^2_2}}l_{mix}\frac{d\overline{T}}{dx_2} \tag{2.22}$$

By comparing Eq.(2.16) and Eq.(2.17), immediately appears that $\alpha_t = \nu_t$, than with the definition of turbulent Prandl number Eq.(2.18), $Pr_t = 1$. Thus molecular viscosity or molecular thermal diffusivity are considered negligible because this approach is based on the hypothesis that transfer mechanism for momentum and energy is the same.

However, turbulent eddies can transfer momentum not just only with the viscous forces but also with the pressure forces. One the other hand there is no mechanism other than molecular conduction whereby energy can be transferred to or from an eddy. Therefore the two transfer mechanism are not the same.

Thus is obvious that for liquid metals $Pr_t \neq 1$. The role played by the high thermal conductivity for liquid metals leads to lose eddies energy by conduction before it travel a distance compared to l_{mix}, a $Pr_t > 1$ menas that turbulent heat transfer is not comparable to the turbulent momentum transfer.

If is considered a fluid with $Pr > 1$ is possible to an eddy to loose the biggest amount of its $x_1 - momentum$ before travel the l_{mix} distance, so while still having velocity in the x_2 direction. Heat, in this case is carried to a greater distance than momentum, looking at the turbulent Prandtl number it'll be lesser than unity.

Generally the approach adapt Reynolds analogy, to the fluids with a Prandtl number around or greater than unity is common to assign a $Pr_t = 0.85$. This is not the methodology adopted for liquids metals.

Concluding this paragraph low-Prandtl number fluids like liquid metals are not suitable for Reynolds analogy, their turbulent heat transfer scales are too different from the turbulent momentum scales, thermal ones are much greater than the other. This lead to a temperature field too different from a case where Reynolds analogy is applied, whereby it must be chosen a model which take in to account these difference.

2.4. Problem description

For the liquid metal heat transfer descripted in Paragraph 2.3 the Reynolds analogy is not valid and introduces the necessity to use new models to predict the heat transfer in the geometry descripted in Paragraph 2.1. The rod bundle with a constant heat flux longitudinally and circumferentially cooled by liquid metals is a recurring theme widely studied as cited in this thesis introduction in Chapter 1.

The introduction of a grid spacer in the rod bundle geometry makes the problem peculiar differing from the normal cases without spacer [14] thus, it requires a specific study. Manservisi and Menghini [15] developed a new model to study the specific liquid metals heat transfer. The model will be tested in the rod bundle geometry with grid spacers and its results will be compared with the turbulent Prandtl correlations developed by W.M. Kays [4], and X. Chen, N.I. Tak [3]. The Chapter 3 describes the turbulent models used to solve the velocity and temperature field which are used in this thesis.

Chapter 3

3. The turbulence models

3.1. Turbulence modeling theory

The time averaged Navier Stokes equations Eq.(2.2), (2.3), (2.4) using Eq.(2.10) generate the new averaged set of Reynolds equations Eq.(2.11), (2.12), (2.13). The computational models that use these equations are named with the acronym RANS (Reynolds Averaged Navier Stokes), these equations compute the velocity and temperature of the mean flow. The RANS equations are divided in two main family the difference is the way used to compute the Reynolds stresses Eq.(2.19), and the turbulent heat flux Eq.(2.20), using the Boussinesque hypothesis respectively in Eq.(2.21), and Eq.(2.22). The Reynolds stresses became as (3.1), $k = 1/2\left(\overline{u'^2} + \overline{v'^2} + \overline{w'^2}\right)$. is the turbulent kinetic energy.

$$\bar{\bar{\tau}}_t = \begin{Bmatrix} \left(2\mu_t \frac{\partial \overline{U}_x}{\partial x} - \frac{2}{3}k\rho\right) & \mu_t\left(\frac{\partial \overline{U}_x}{\partial y} + \frac{\partial \overline{U}_y}{\partial x}\right) & \mu_t\left(\frac{\partial \overline{U}_x}{\partial z} + \frac{\partial \overline{U}_z}{\partial x}\right) \\ \mu_t\left(\frac{\partial \overline{U}_x}{\partial y} + \frac{\partial \overline{U}_y}{\partial x}\right) & \left(2\mu_t \frac{\partial \overline{U}_y}{\partial y} - \frac{2}{3}k\rho\right) & \mu_t\left(\frac{\partial \overline{U}_y}{\partial z} + \frac{\partial \overline{U}_z}{\partial y}\right) \\ \mu_t\left(\frac{\partial \overline{U}_x}{\partial z} + \frac{\partial \overline{U}_z}{\partial x}\right) & \mu_t\left(\frac{\partial \overline{U}_y}{\partial z} + \frac{\partial \overline{U}_z}{\partial y}\right) & \left(2\mu_t \frac{\partial \overline{U}_z}{\partial z} - \frac{2}{3}k\rho\right) \end{Bmatrix} \quad (3.1)$$

The Boussinesque hypothesis have also some approximations. The term $[2/3\,k\rho]$ in the tensor main diagonal ensure the correct value of the normal Reynolds stresses. The trace of the tensor is $-\left(\overline{u'^2} + \overline{v'^2} + \overline{w'^2}\right)$ and is equal to $-2\rho k$, under the incompressible fluid hypothesis the continuity equation is: $\partial \overline{U}_i/\partial x_i = 0$. The (3.1) trace without $[2/3\,k\rho]$ in the main diagonal would be equal to zero. The term added to ensure a correct physical value of the Reynolds stresses is isotropic, which is an approximation.

The turbulent viscosity μ_t is a scalar thus, the proportionality of the main deformation rate is the same in all the directions. This is the second approximation of the Boussinesque hypothesis, a more detailed theory of turbulence can be found in [20].

Generally turbulent models compute only the turbulent viscosity, since the most common fluids used in simulations submit the Reynolds analogy hypothesis, the turbulent Prandtl number is taken constant, set to a value of 0.85 and is possible to obtain the turbulent thermal diffusivity α_t from the Eq.(2.18). The peculiar liquid metals heat transfer requires a more suitable value of the turbulent thermal diffusivity since they don't submit the Reynolds analogy hypothesis, it is thus necessary a model to compute the heat transfer coefficient or the turbulent Prandl number.

3.2. Flow field turbulence models

In this work are used three flow turbulent models. First is the $k-\varepsilon$ AKN (presented by K. Abe, T. Kondoh and Y. Nagano). Second is the $k-\omega\ SST$ (shear stress model) developed by F.R. Menter. The last is a $k-\varepsilon-\overline{v^2}-f$. All models are all low Reynolds models, they differ from high Reynolds because they don't use a wall functions and the transport equations can be integrated down to the wall.

3.2.1. Low Reynolds models

The choice of low Reynolds models in this particular application that works with LBE is necessary. Close to the wall the local Reynolds number and velocity decrease till arrive to quantities close to zero, in that region is possible to define non-dimensional quantities: u^+ in Eq.(3.2), y^+ in Eq.(3.3) and θ^+ in Eq.(3.4).

$$u^+ = \frac{u}{u_\tau}; \quad u_\tau = \sqrt{\frac{\tau_w}{\rho}} \tag{3.2}$$

$$y^+ = \frac{u_\tau\, y}{\nu} \tag{3.3}$$

$$\theta^+ = \frac{T_w - T}{T_\tau}\ ; \quad T_\tau = \frac{q''}{u_\tau \rho c_p} \tag{3.4}$$

In Fig. 3.1 the first region from the wall is for $y^+ < 5$ and is a linear region where non dimensional velocity u^+ in Fig. 3.1 is equal to non-dimensional distance from wall y^+, and is called viscous sub layer. In this region the momentum transport is determined only by viscous stresses. The next region is called buffer layer where turbulent effects have the similar magnitude of viscous ones, in a y^+ between 5 and 30. Than in a range of y^+ between 30 and 500 the fluid zone is called logarithmic region and are dominant turbulent effects.

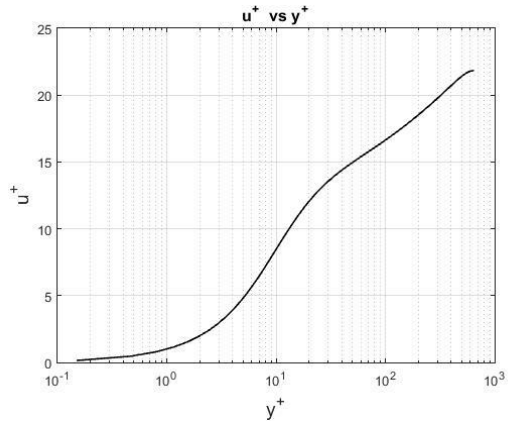

Fig. 3.1 DNS data of u plus against y plus in a channel flow with $Re_\tau = 640$ and Pr= 0.025, from the Kawamura database [21]

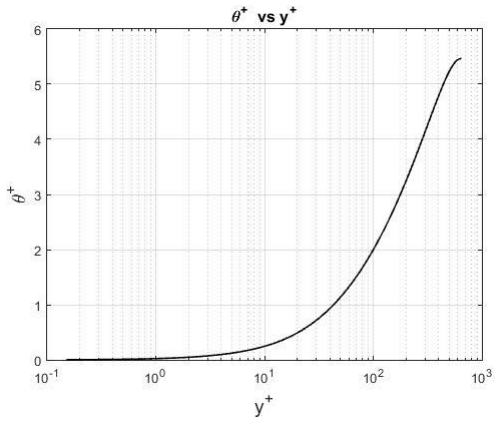

Fig. 3.2 DNS data of theta plus against y plus in a channel flow with $Re_\tau = 640$ and Pr= 0.025, from the Kawamura database [21]

High Reynolds turbulent models use a wall function. The wall function reproduces the inner layer profile because it is universal and is not any more necessary to integrate the model down to the wall.

Considering a fluid with a Prandtl number across unity the variable θ^+ close to the wall where the thermal energy transport is dominated by laminar molecular diffusivity α the profile is linear for an $y^+ < 5$(linear sub-layer). The buffer layer and the log law is similar in the same velocity range respectively: for $5 < y^+ < 30$ the thermal energy transport is dominated by laminar effects due to α and by turbulent effects due to α_t both of equal magnitude. The last region of the inner layer for an $30 < y^+ < 500$ is dominated only by turbulent energy transport. Thus the $\theta^+$and u^+ profile match each other under the Reynolds analogy hypothesis.

If is considered a low Prandtl number fluid such as LBE $Pr = 0.025$ in Fig. 3.2, the Reynolds analogy is not valid anymore, in this case the molecular diffusivity α is much more important and its effect makes the linear temperature profile much more longer. The linear region and the buffer layer are extended up to $y^+ \simeq 300$. This peculiarity makes normal wall functions not suitable for these fluids, this is why is better to use low Reynolds models which integrate their turbulent equations down to the wall without using wall functions.

3.2.2.$k - \varepsilon$ AKN

This model has been developed by K. Abe, T. Kondoh and Y. Nagano, it is a two equations $k - \varepsilon$ low Reynolds model, the additional partial differential equation for k: turbulent kinetic energy k $[m^2/s^2]$ and the other for the turbulent dissipation rate ε $[m^2/s^3]$.

$$k = \frac{1}{2}\left(\overline{u'^2} + \overline{v'^2} + \overline{w'^2}\right) \tag{3.5}$$

$$\varepsilon = 2\nu \overline{\frac{\partial u_i'}{\partial x_j}\frac{\partial u_i'}{\partial x_j}} \tag{3.6}$$

AKN model is based on the Buossinesque hypothesis, the turbulent viscosity $\nu_t[m^2/s]$ is defined as a product of a turbulent velocity scale $\vartheta\ [m/s]$, a turbulent leght scale $l\ [m]$ and a constant term:

$$\nu_t = C\vartheta l \tag{3.7}$$

$$\vartheta = k^{1/2}; \quad l = \frac{k^{3/2}}{\varepsilon}; \quad \nu_t = C_\nu \frac{k^2}{\varepsilon} \tag{3.8}$$

This model use damping function which are derived from the Kolmogorow velocity scale $u_\varepsilon = (\varepsilon\nu)^{1/4}$instead of the friction velocity. The friction velocity is equal to zero in the separating and reattaching points where $\tau_w = 0$, these are singularity points.

The Kolmogorow velocity instead avoids singularities because has a non-zero value on the wall and on separating and reattaching points. These damping functions which are based on the Kolmogorow velocity, are suitable to model the near wall behavior of the flow. Than the model defines a local dynamical characteristic time scale that takes into account the correction in to the wall region τ_{lu} in order to compute the turbulent viscosity in Eq.(3.9).

$$\tau_u = \frac{k}{\varepsilon} \rightarrow \nu_t = C_\mu k \tau_{lu} \tag{3.9}$$

The partial differential equations for the transport of the turbulent kinetics energy is Eq.(3.10), and the turbulent dissipation rate is Eq.(3.12):

$$\frac{\partial k}{\partial t} + (\boldsymbol{u}\cdot\nabla)\mathrm{k} = \nabla\cdot\left[\left(\nu + \frac{\nu_t}{\sigma_k}\right)\nabla k\right] + P_k - \varepsilon \tag{3.10}$$

$$P_k = -\overline{u_i' u_j'}\frac{\partial u_i}{\partial x_j} \tag{3.11}$$

$$\frac{\partial \varepsilon}{\partial t} + (\boldsymbol{u}\cdot\nabla)\varepsilon = \nabla\cdot\left[\left(\nu + \frac{\nu_t}{\sigma_\varepsilon}\right)\nabla\varepsilon\right] + C_{1\varepsilon}\frac{\varepsilon}{k}P_k - C_{2\varepsilon}\frac{\varepsilon^2}{k}f_\varepsilon \tag{3.12}$$

$$f_\varepsilon = \{1 - exp(-0.3226R_\delta)\}^2\{1 - 0.3exp(-0.0237{R_t}^2)\} \tag{3.13}$$

Than completing the initial equation of turbulent viscosity Eq.(3.9).

$$\tau_{lu} = \left(f_{1\mu}A_{1\mu} + f_{2\mu}A_{2\mu}\right) \tag{3.14}$$

$$f_{1\mu} = \left[1 - exp(-0.0714R_{\delta})\right]^2 \tag{3.15}$$

$$A_{1\mu} = \tau_u = \frac{k}{\varepsilon} \tag{3.16}$$

τ_u is the dynamical characteristic time of the turbulence.

$$A_{2\mu} = \tau_u \frac{5}{R_t^{3/4}} \tag{3.17}$$

$$R_t = \frac{k^2}{\nu\varepsilon}; \quad R_{\delta} = \frac{y(\varepsilon\nu)^{1/4}}{\nu} \tag{3.18}$$

The values of the constants are in (3.19).

$$C_{\mu} = 0.09; \quad \sigma_k = 1.4; \quad \sigma_{\varepsilon} = 1.4; \quad C_{1\varepsilon} = 1.5; \quad C_{2\varepsilon} = 1.9 \tag{3.19}$$

The $k-\varepsilon$ AKN model is already implemented in Fluent v.15, but constants are different and they need to set up correctly. The proper boundary conditions to set up in to the wall are in (3.20).

$$\left.\frac{dk}{dy}\right|_w = \frac{2k}{y}; \quad \varepsilon|_w = \nu\frac{2k}{y^2} \tag{3.20}$$

Further details are available in [22].

3.2.3. $k-\omega$ SST

An alternative to the standard $k-\varepsilon$, is the Wilcox's model it uses the turbulence frequency $\omega = \varepsilon/k \ \left[1/s\right]$ as a second variable instead of turbulent dissipation rate ε. The turbulent viscosity Eq.(3.21) is always defined as a product of a velocity scale and a length scale depending from k and ω.

$$\nu_t = k/\omega \tag{3.21}$$

This model is interesting because it doesn't require wall damping function in low Reynolds number applications. The value of the turbulent kinetic energy at the wall is zero. The frequency ω tend to infinity at the wall but is possible to specify a very large value from the formulation of ν_t which tends to 0. The boundary conditions of ω in a free stream where turbulent kinetic energy $k \to 0$ and turbulence frequency $\omega \to 0$, is the most problematic feature. Eq.(3.21) shows that turbulent eddy viscosity isn't determinate or tends to infinity. The model is dependent on the assumed free stream value of ν_t.

Menter (1992) noted that results of $k-\varepsilon$ model are much less sensitive to the assumed values in the free stream, but its near wall performance is unsatisfactory for boundary layers with adverse pressure gradients. This led him to suggest a hybrid model called $k-\omega\ SST$ (shear stress transport) using a transformation of the $k-\varepsilon$ model in to a $k-\omega$ model in the near wall region and the standard $k-\varepsilon$ model in the fully turbulent region far from the wall.

The other equations for k and ω are:

$$\frac{\partial(\rho k)}{\partial t} + \nabla\cdot(\rho k\boldsymbol{u}) = \nabla\cdot\left[\left(\mu + \frac{\mu_t}{\sigma_k}\right)\nabla k\right] + P_k - \beta^*\rho k\omega \tag{3.22}$$

$$P_k = \left(2\mu S_{ij}\cdot S_{ij} - \frac{2}{3}\rho\omega\frac{\partial U_i}{\partial x_j}\delta_{ij}\right) \tag{3.23}$$

$$\begin{aligned}\frac{\partial(\rho\omega)}{\partial t} + \nabla\cdot(\rho\omega\boldsymbol{u}) \\ = \nabla\cdot\left[\left(\mu + \frac{\mu_t}{\sigma_{\omega,1}}\right)\nabla(\omega)\right] + \gamma_2 P_k^* - \beta_2\rho\omega^2 + 2\frac{\rho}{\sigma_{\omega,2}\omega}\frac{\partial k}{\partial x_k}\frac{\partial\omega}{\partial x_k}\end{aligned} \tag{3.24}$$

The model peculiarity is the blending function, because numerical instabilities may be caused by differences in the computed values of the eddy viscosity with the standard $k-\varepsilon$ model in the far field and the transformed $k-\varepsilon$ model near the wall. Blending functions are used to achieve a smooth transition between the two models.

The other change introduced by Menter is in the definition of the turbulent viscosity in Eq.(3.25):

$$\nu_t = \frac{a_1 k}{\max(a_1\omega,\ SF_2)} \tag{3.25}$$

This definition bound the turbulent viscosity and improves the performance in flows with adverse pressure gradients and wake regions, and the turbulent kinetic energy production is limited to prevent the increase of turbulence in stagnation regions.

$$S = \sqrt{2S_{ij}S_{ij}};\quad a_1 = const.;\quad F_2 = blending\ function \tag{3.26}$$

$$P_k^* = min\left(10\beta^*\rho k\omega, \qquad 2\mu S_{ij}\cdot S_{ij} - \frac{2}{3}\rho k\frac{\partial U_i}{\partial x_j}\delta_{ij}\right) \tag{3.27}$$

Further details are available in [17].

3.2.4. $k-\varepsilon-v^2-f$

The v^2-f model is a four-equation model based on transport equations for the turbulence kinetic energy k in Eq.(3.29), it's dissipation rate ε in Eq.(3.30), a velocity scale $\overline{v^2}$ in Eq.(3.31), and an elliptic relaxation function f in Eq.(3.32). v^2-f model is different from a standard $k-\varepsilon$ because uses the velocity scale, $\overline{v^2}$, instead of the turbulent kinetic energy k, to evaluate the eddy viscosity in Eq. (3.28).

$$\nu_t = C_\mu\overline{v^2}T \tag{3.28}$$

This velocity scale can be thought as a velocity fluctuations of the normal streamlines, it has shown to provide the right scaling in representing the damping turbulent transport close to the wall.

The variable f is the solution of the elliptic relaxation equation in Eq.(3.32), the elliptic operator is necessary to compute a term analogous to the pressure strain correlation of the RSM. Ellipticity is characterized by a modified Helmholtz operator, which introduces wall effects via linear differential equation.

$$\frac{\partial\rho k}{\partial t} + \nabla\cdot(\rho\boldsymbol{u}k) = P - \rho\varepsilon + \nabla\cdot\left[\left(\mu + \frac{\mu_t}{\sigma_k}\right)\nabla k\right] + S_k \tag{3.29}$$

$$\frac{\partial\rho\varepsilon}{\partial t} + \nabla\cdot(\rho\boldsymbol{u}\varepsilon) = \frac{C'_{\varepsilon1}P - C_{2\varepsilon}\varepsilon\rho}{T} + +\nabla\cdot\left[\left(\mu + \frac{\mu_t}{\sigma_\varepsilon}\right)\nabla\varepsilon\right] + S_\varepsilon \tag{3.30}$$

$$\frac{\partial\rho\overline{v^2}}{\partial t} + \nabla\cdot\left(\rho\boldsymbol{u}\overline{v^2}\right) = \rho k f - 6\rho\overline{v^2}\frac{\varepsilon}{k} + \nabla\cdot\left[\left(\mu + \frac{\mu_t}{\sigma_k}\right)\nabla\overline{v^2}\right] + S_{\overline{v^2}} \tag{3.31}$$

$$f - L^2\nabla\cdot(\nabla f) = (C_1 - 1)\frac{\frac{2}{3} - \overline{v^2}/k}{T} + C_2\frac{P}{k\rho} + \frac{5\overline{v^2}/k}{T} + S_f \tag{3.32}$$

$$P = 2\mu_t S^2, \quad S^2 \equiv S_{ij}S_{ij}, \quad S_{ij} = \frac{1}{2}\left(\frac{\partial u_j}{\partial x_i} + \frac{\partial u_i}{\partial x_j}\right) \tag{3.33}$$

The turbulent time scale T and length scale L are defined respectively in (3.34) and (3.35).

$$T' = max\left[\frac{k}{\varepsilon}, 6\sqrt{\frac{\overline{v}}{\varepsilon}}\right]; \qquad T = min\left[T', \frac{\alpha}{\sqrt{3}}\frac{k}{\overline{v^2}C_\mu\sqrt{2S^2}}\right] \tag{3.34}$$

$$L' = min\left[\frac{k^{3/2}}{\varepsilon}, \frac{1}{\sqrt{3}}\frac{k^{3/2}}{\overline{v^2}C_\mu\sqrt{2S^2}}\right]; \qquad L = C_L max\left[L', C_\eta\left(\frac{v^3}{\varepsilon}\right)^{1/4}\right] \tag{3.35}$$

The constants of the model are in (3.36) where $\sigma_k$and σ_ε are turbulent Prandtl numbers respectively for k and ε. $S_k, S_\varepsilon, S_{\overline{v^2}}, S_f$, are user-defined source terms.

$$\begin{gathered} C_\mu = 0.22; \quad \sigma_k = 1; \quad C_{1\varepsilon} = 1.4; \quad C_{2\varepsilon} = 1.9; \quad C_l = 1.4; \quad C_2 = 0.3; \quad C_\eta = 70; \\ C_L = 0.23; \quad \sigma_\varepsilon = 1; \quad \alpha = 0.6; \quad C_{\varepsilon 1}^* = C_{\varepsilon 1}\left(1 + 0.045\sqrt{k/\overline{v^2}}\right) \end{gathered} \tag{3.36}$$

To activate this model which is already implemented in Fluent follow the guide in [23].

3.3. Thermal turbulence models

Enabling the energy equation in Fluent automatically the value of the turbulent Prandtl number is already set up to a constant value: $Pr_t = 0.85$, it is constant in all the spatial and time domain.

This is the strongest limitation, because it means that turbulent thermal diffusivity depends only on a constant by the turbulent viscosity, as is shown in Eq.(2.18). The turbulent viscosity is defined by the turbulence models and is not constant in the domain. Performing the approach of the constant turbulent Prandtl number set up to 0.85 is a good approximation for fluids which have a Prandtl number close to unity or greater like air $(Pr = 0.71)$, or water $(Pr = 7.01)$.

Considering liquid metals this approximation is no more suitable, there are other way to calculate turbulent Prandtl number with models or correlations. Two semi-empirical correlations are used in this work. First requires average properties of the momentum equations to give a constant turbulent Prandtl number (X. Cheng and N. I. Tak). The second correlation works with the local proprieties of the momentum equations to give a turbulent Prandtl number depending also from the spatial coordinates (W. M. Kays).

The other way to compute the turbulent Prandtl number is with a model. $k_\vartheta - \varepsilon_\vartheta$ model developed by S. Manservisi and F. Menghini which calculates the turbulent thermal diffusivity to use in the Eq.(2.18) and obtains the turbulent Prandtl number value in each point.

3.3.1.X. Cheng and N.I. Tak turbulent Prandtl correlation

$$Pr_t = \begin{cases} 1.5, & Pe \leq 2000 \\ 2.5 - 0.0005Pe, & 2000 \leq Pe \leq 3000 \\ 1, & Pe \geq 3000 \end{cases} \tag{3.37}$$

The correlation in Eq.(3.37) is developed by X. Cheng and N. I. Tak, (2006) it relates the mean turbulent Prandtl number to the mean Péclet number $Pe = Pr \cdot Re$, it is developed for liquid metals, in particular for mercury. This means that the Prandtl number is constant or within a range around the mercury value which also includes the LBE. The correlation validity is checked by the results of Maresca and Dwyer which performed several experiments in a vertically arranged triangular rod bundle cooled by mercury. The test section has 13 rods inside a cylindrical shell, data where measured only on the central rod. It was assumed that the thermal hydraulic behavior around this rod was the same as that around a rod of a rod bundle with infinite rods.

Results in Fig. 3.3 where than matched to the ones performed by Cheng and Tak using CFX code, reproducing the same case of an infinite rod bundle in fully developed conditions, analyzing the Nusselt number behavior varying the Turbulent Prandtl number. Starting from a Péclet lower than 2000 the turbulent Prandtl number matching with the experimental data is 1.5, increasing the mean Peclét the turbulent momentum exchange gain more importance compared to the turbulent heat transfer, this lower the Péclet till a value of one for a turbulent Prandtl number greater than 3000.

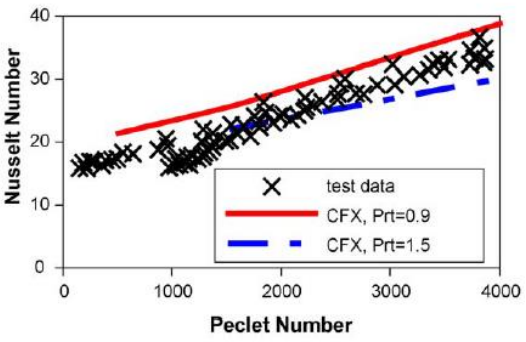

Fig. 3.3 Comparison of CFX results with test data in Mercury, [18]

The pitch to diameter p/d is the most important parameter to describe rod bundle geometry (p is the distance between two rod center and d is diameter of a rod). The correlation presented can be used for $p/d \geq 1.3$ in the triangular lattices or $p/d \geq 1.6$ in square lattices. A more detailed description can be found in [3].

3.3.2. W. Kays turbulent Prandtl number

The turbulent Prandtl definition presented by Kays showed in Eq.(3.38) comes from a study of a numerical simulation (DNS) in a channel heated by constant heat flux. Results show that turbulent Prandtl curves collapse in one considering as a variable the turbulent Péclet number: $Pe_t = Pr\frac{\nu_t}{\nu}$.

This variable takes in account the effect of a different fluid with the number of the linear Pr and the kind of momentum transport depending also from the wall distance due to the turbulent viscosity ratio.

The curve which represents the function in Eq.(3.38) To great Pe_t values approaches the turbulent Prandtl number value of 0.85, it is consistent with the experimental data in the literature.

$$Pr_t = 0.85 + \frac{0.7}{Pe_t} \tag{3.38}$$

At very low values of Pe_t, turbulent Prandtl become very high, consistent with the observation of liquid metal in the log region. This correlation introduces less approximations compared to Cheng and Tak turbulent Prandtl correlation.

In the W.M. Kays article it is also stated that comparing several experimental test data performed in a pipe with liquid metal fluid as a coolant, in a fully developed regime, the equation in (3.38) fits the data with a coefficient of 2 instead of 0.7. But is also said that there is a considerable scatter of the data. More details are available in [4].

Kays Pr_t is based on local quantities that are computed at every iteration. A UDF function is coupled to the code Fluent v.15 in order to set the correct value in every point at every iteration, the UDF function is available in Appendix B.

3.3.3. $k_\theta - \varepsilon_\theta$ model

Manservisi and Menghini $k_\theta - \varepsilon_\theta$ model has an other approach to the problem, this model works like a normal $k - \varepsilon$ low Reynolds, thus calculate turbulence scales for turbulent thermal diffusivity which coupled with turbulent dynamic viscosity from the momentum turbulence model gives the turbulent Prandtl number in $Eq.\,(2.18)$. The two additional transport equation are for the temperature variance and its dissipation rate.

$$\kappa_\theta = \frac{1}{2}\overline{(T')^2} \tag{3.39}$$

$$\varepsilon_\theta = \alpha\overline{\left(\frac{\partial T'}{\partial x_i}\right)^2} \tag{3.40}$$

Now turbulent thermal diffusivity and turbulent dynamic viscosity are not directly related, this is a better approximation compared to the two correlations in Paragraph 3.3.1 and 3.3.2, but there are two more equations to solve, means a further computational effort.

K. Abe, T. Kondoh and Y. Nagano developed their $k_\theta - \varepsilon_\theta$ to predict the heat transfer. This model was calibrated with air ($Pr = 0.71$).Manservisi $k_\theta - \varepsilon_\theta$ model is based on the AKN $k_\theta - \varepsilon_\theta$, than needs the flow field computed by the AKN $k - \varepsilon$ model in Paragraph 3.2.2.

The model had been specifically calibrated for liquid metals. The constants used to derive it, in fact come from an other two equation turbulence model for the temperature field presented in: [24]. This model was developed to work with every kind of fluid varying the Prandtl number including the very low ones, according with the theory presented before in Paragraph 3.2.

The additional transport equations are Eq.(3.41) and Eq.(3.42), where $-\overline{u_i T'}$ is modelled using the expression q_t'' in Eq.(2.17).

$$\frac{\partial k_\theta}{\partial t} + \overline{U}_j \frac{\partial k_\theta}{\partial x_j} = \frac{\partial}{\partial x_j}\left\{\left(\alpha + \frac{\alpha_t}{\sigma_{k\theta}}\right)\frac{\partial k_\theta}{\partial x_j}\right\} + P_\theta - \varepsilon_\theta \tag{3.41}$$

$$\begin{aligned}\frac{\partial \varepsilon_\theta}{\partial t} + \overline{U}_j \frac{\partial \varepsilon_\theta}{\partial x_j} = \frac{\partial}{\partial x_j}\left\{\left(\alpha + \frac{\alpha_t}{\sigma_{\varepsilon\theta}}\right)\frac{\partial \varepsilon_\theta}{\partial x_j}\right\} - \frac{\varepsilon_\theta}{k_\theta}\left(C_{p1}P_\theta - C_{d1}\varepsilon_\theta\right) \\ + \frac{\varepsilon_\theta}{k}\left(C_{p2}P_K - C_{d2}\varepsilon\right)\end{aligned} \tag{3.42}$$

$$P_\theta = -\overline{u_i T'}\frac{\partial \overline{T}}{\partial x_j} \tag{3.43}$$

The turbulent thermal diffusivity is than computed in Eq.(3.44).

$$\alpha_t = C_\theta k \tau_{l\theta} \tag{3.44}$$

$$\tau_{l\theta} = (f_{1\theta}B_{1\theta} + f_{2\theta}B_{2\theta}) \tag{3.45}$$

$$f_{1\theta} = \left[1 - exp\left(-0.0526\sqrt{Pr}R_\delta\right)\right][1 - exp(-0.0714R_\delta)] \tag{3.46}$$

$$B_{1\theta} = \tau_u Pr_{t\infty} \tag{3.47}$$

$$f_{2\theta}B_{2\theta} = \tau_u\left(f_{2a\theta}\frac{2R}{R + C_\gamma} + f_{2b\theta}\sqrt{\frac{2R}{Pr}}\frac{1.3}{\sqrt{Pr}R_t^{3/4}}\right) \tag{3.48}$$

$$f_{2a\theta} = f_{1\theta}\exp(-4 \times 10^{-6} R_t^2) \tag{3.49}$$

$$f_{2b\theta} = f_{1\theta}\exp(-2.5 \times 10^{-5} R_t^2) \tag{3.50}$$

The constants values are:

$$C_\theta = 0.1; \quad \sigma_{k\theta} = 1.4; \quad \sigma_{\varepsilon\theta} = 1.4; \quad C_\gamma = 0.3;$$
$$Pr_{t\infty} = 0.9; \quad C_{p1} = 0.925; \quad C_{d1} = 1; \quad C_{p2} = 0.9$$

$$C_{d2} = \left[1.9\left(1 - 0.3exp(-0.0237R_t^2)\right)\right][1 - exp(-0.1754R_\delta)]^2$$

The damping function of the Manservisi $k_\theta - \varepsilon_\theta$ model contain quantities referred both to the turbulent scales of velocity and temperature. These are reported in (3.51) and (3.52).

$$\tau_u = \frac{k}{\varepsilon}; \qquad \tau_\theta = \frac{k_\theta}{\varepsilon_\theta}; \qquad \tau_m = \frac{\tau_u 2R}{R + C_\gamma} \tag{3.51}$$

$$R_t = \frac{k^2}{\nu\,\varepsilon}; \qquad R_\delta = \frac{y u_\varepsilon}{\nu}; \qquad R = \frac{\tau_\theta}{\tau_u} \tag{3.52}$$

These are three characteristic time scale: τ_u dynamical time, τ_θ dynamical thermal time, τ_m the mixed time. R is the ratio between the thermal time and appears in the damping function to model the behavior of the turbulent thermal diffusivity within the linear sub layer and the buffer layer. The proper boundary condition to set at the wall for an imposed heat flux are in (3.53).

$$k_\theta|_w = 0; \qquad \varepsilon_\theta|_w = \alpha \frac{2k_\theta}{y^2} \tag{3.53}$$

The present model is not available in the FLUENT v15 code, so it needs to be implemented with a UDF it is available in the Appendix A. Model has been presented in [15] and [2].

Chapter 4

4. The computational domain

4.1. Meshing the domain

The CFD approach is based on a numerical solution such as it is explained in Paragraph 2.3, this requires the domain discretization which is the mesh and it is made up by an amount of elements, the cells, in which every set of equations (continuity, momentum, energy and turbulence) are solved. The equations are solved for every cell center and the remaining points are an approximation of the surrounding cells center. Thus thinking ideally to fill the geometry with an infinite number of infinitesimal cells the equations solution is known in every point belonging to the domain. This is actually not possible due to the computational effort. The building mesh work consist to find a good compromise with the solution accuracy and the computational time necessary to have satisfactory convergence. It means place the lowest number of cells possible to solve the equations with reliable solutions.

There are two main meshes families, structured-grid and unstructured-grid. The following section will describe the mesh choice highlighting the advantages and disadvantages.

4.1.1.Structured-grids

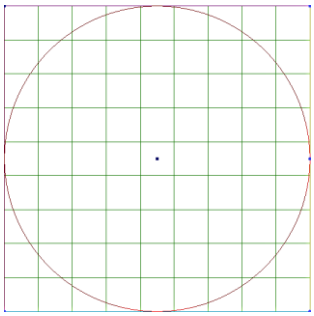

Fig. 4.1 Cartesian grid of a circle

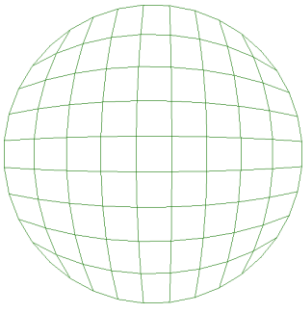

Fig. 4.2 body fitted grid of a circle.

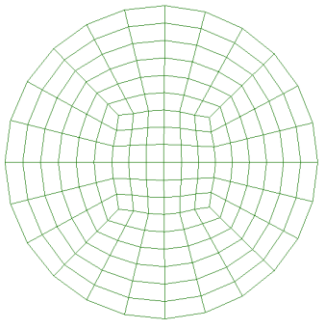

Fig. 4.3 Block-structured grid of a circle (5 blocks).

The methods to solve transport equations are based on orthogonal coordinate system which can also be transposed into cylindrical or spherical, for complex geometry such as in engineering applications orthogonal coordinates in two or three dimension are more suitable. Thus, in this work, in every cell where equations are solved need to be defined in an orthogonal coordinates system.

The process to mesh a circle starts overlapping a Cartesian grid to the geometry in Fig. 4.1, the circle boundary doesn't coincide with the grid. Than it is necessary to consider only the cells inside the circle and on its boundary. It isn't a good geometry approximation, one solution in this

case could be to make the grid more fine increasing the resolution close to the boundary but are necessary more cells. The other solution is to move the grid points close to the boundary from their original position on the boundary obtaining a body fitted grid such as shows Fig. 4.2. This is the simplest way to mesh a complex geometry with a structured grid. A structured grid can be thus defined with the following main feature from [17]:

- Grid points are placed at the intersection of the co-ordinates lines.
- Interior grid points have a fixed number of neighboring grid points.
- Grid points can be mapped in to a matrix, their location in the grid structure and in the matrix is given by indices ($\boldsymbol{i}, \boldsymbol{j}$ in two dimension and $\boldsymbol{i}, \boldsymbol{j}, \boldsymbol{k}$ in three dimension).

The body fitted mesh has still some problems because some peripheral cells are highly deformed from the original square contour, there isn't the possibility to increase the number of cells in to the center area leaving a coarse resolution on the boundary or the opposite. To overcome this problem cells can be divided in macro-areas called blocks. The cells inside a block respect the structured mesh main features. The grid in Fig. 4.3 has five blocks one in the center surrounded by other four in contact with the circle boundary. The cell distribution inside is more homogenous with a lower cell distortion compared to Fig. 4.2.

Structured grids use square in the plane cases and tetrahedral elements in the space, the blocks distribution is a manual operation there still isn't a commercial algorithm able to do it automatically.

4.1.2. Unstructured-grids

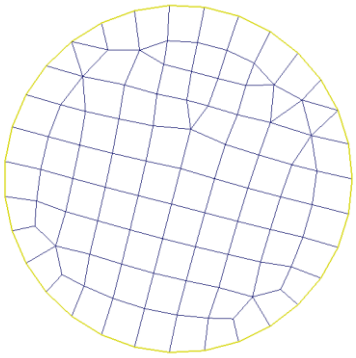

Fig. 4.4 Unstructured grid of a circle.

In complex geometries it may be necessary to use many different shapes blocks. The logical extension of this idea is the unstructured mesh. An example is in Fig. 4.4, where each cell is considered a block. The advantage is that the main feature of the structured mesh are not respected. Fig. 4.4 has some internal points where converge four or five lines and the cells are mainly square but also triangle shape. The mesh can be refined in every zone without influencing the remaining parts.

Every cell type is allowed with every geometry in two dimension cases and in three dimension ones, including the generic polyhedral shapes. Specific algorithm were developed to create automatically these mesh without spending user's time. The saved time on the grid construction is the best advantage using these grids.

Despite the unstructured grids description seems to be the better choice and sometimes also the only way, in this thesis have been used only block structured grids. The advantage using only hexahedral cells well-disposed following a precise coordinate system is on cell surfaces, which can be disposed orthogonally to the main flow and to the main gradients. It reduces the gradient

cross-diffusion term, which appears defining the generic quantity gradient on the cell boundary and it represents a source of uncertainty. A detailed explanation is available in [17].

4.2. Domain and boundary conditions

As descripted in Paragraph 2.1.1 the experimental set up, measuring planes are placed $2.5\ mm$ upstream of the spacers, the position of each thermocouple is showed in Fig. 2.4. At each measuring plane, a local heat transfer coefficient α is defined as in Eq(4.1), where $\langle T_w \rangle$ and T_b are the mean wall and bulk temperatures respectively. On the other hand, T_b is derived from an energy balance throughout the test section (from the inlet to the outlet), considering a temperature dependent heat capacity as in Eq.(4.2).

$$\alpha = \frac{q_w}{\langle T_w \rangle - T_b} \tag{4.1}$$

$$Q\frac{x}{L} = \dot{m}\int_{T_{in}}^{T_b} c_p(T)dT \tag{4.2}$$

Based on the measurements, geometrical parameters and mean physical properties, non-dimensional local Nusselt and Péclet are formed as in Eq.(4.3) and Eq.(4.4) respectively. In this case physical properties (λ, c_p) are evaluated at the mean value between the inlet and local bulk temperatures. With λ, c_p at $(T_{in} + T_b)/2$.

$$Nu = \frac{\alpha\, d_{h,sch}}{\lambda} \tag{4.3}$$

$$Pe = \frac{\dot{m}}{A}\frac{d_{h,sch}\, c_p}{\lambda} \tag{4.4}$$

$$d_h = d\left[\frac{2\sqrt{3}}{\pi}\left(\frac{p}{d}\right)^2 - 1\right] \tag{4.5}$$

Analyzing the Nusselt number results from the experimental campaign in Fig. 4.5 can be noticed the differences for each Péclet number between the first spacer and the other two with a lower Nusselt number. The second and third spacers have the same Nusselt number value. This is because the first measuring point is relatively close to the heated zone beginning $(x_1/d_{h,sch} = 17.02)$ from Fig. 4.5, the flow is in the thermally developing region. In fact Maresca and Dwyer [25], have observed that following the flow development after a perturbation, the

Nusselt number continuously decrease axially up to $x/d_{h,sch} = 25$. The other two measuring point according with Fig. 4.5 are beyond this limit and thus correspond to a fully developed region.

The experimental setup allows to move the third spacer up to $+90\,mm$ and $-120\,mm$ around its reference position $\left(x_{sp,3,ref} = L_{heat} = 870\,mm\right)$. The investigation results keeping all the other parameters constant are shown in Fig. 4.6 for two different flow rates, corresponding to $Pe = 778 \pm 9$ and $Pe = 2680 \pm 30$ (statistical deviation). Thus it confirms, the flow is a fully developed region.

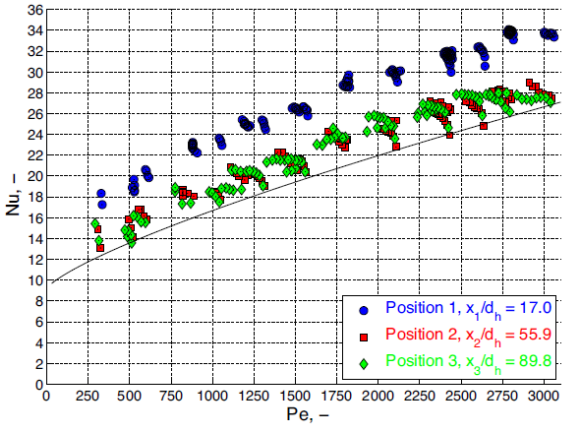

Fig. 4.5 Result of Nusselt number from the experimental campaign at KALLA laboratory, the line is the Mikityuk(2009) correlation for Nu in fully developed flow [1].

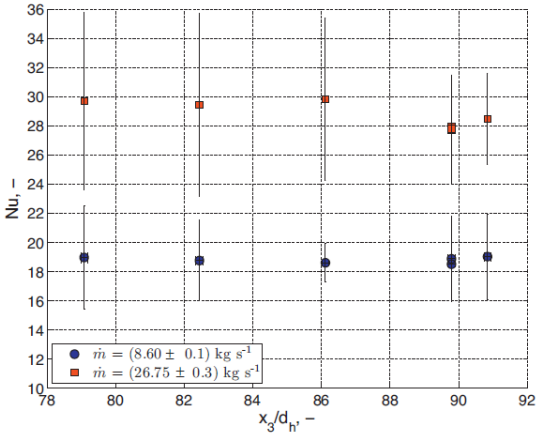

Fig. 4.6 Result for Nusselt number moving the third spacer [1].

The line in Fig. 4.5 is the Mikytiuk correlation for the fully developed flow interpolated from experimental data, fit a wide range $1.1 < p/d < 1.95$ and $30 < Pe < 5000$. The correlation results underestimate the measured Nusselt value of the 15%.

$$Nu = 0.047\left(1 - e^{-3.8\left(\frac{p}{d}-1\right)}\right)\left(Pe^{0.77} + 250\right) \tag{4.6}$$

In a developing flow, heat transfer coefficient is expected to decrease asymptotically in the flow direction downstream of a perturbation, such as the duct entrance or the grid spacers. As a reference, when the differences in Nusselt are smaller than 5%, the flow is said to be fully developed [1]. Although the result presentment in Fig. 4.6 indicate some differences in Nu (up to 6.8% for the largest flow rate), it should be noted that these are smaller than the experimental uncertainties. Under these conditions, the flow can be assumed fully developed.

The mesh domain, is created to simulate one spacer located in the fully developed region, since the second and third spacers have the same value of non-dimensional temperature and Nusselt number. The domain schematically represented in Fig. 4.7, starts with the heated rod $z_{in}/d_h = -10.54$, the spacer inlet is at $z_{in-sp}/d_h = 0$, it ends at $z_{out-sp}/d_h = 2.23$, the end of the heated rod is at $z_{out}/d_h = 32.39$.

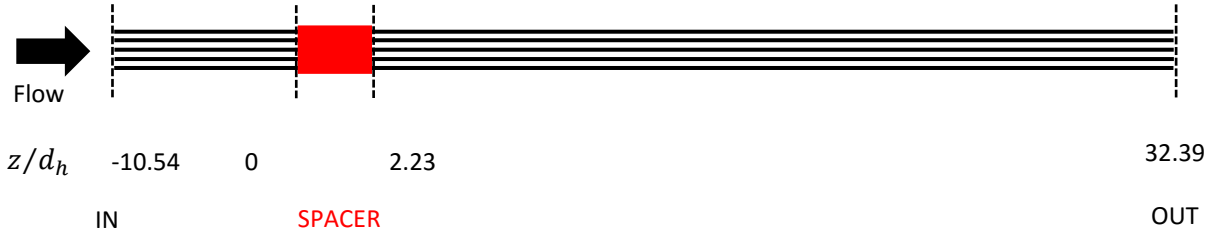

Fig. 4.7 Longitudinal domain representation.

Boundary condition at inlet and outlet of the domain are periodic, in a turbulent flow the fully developed hydrodynamic condition is in Eq.(4.7). Considering the thermal standpoint the fully developed flow is verified in Eq.(4.8), and if in the boundary condition at the wall is imposed a constant heat flux, this implies Eq.(4.9), whereT_b is the bulk temperature.

$$\frac{\partial u}{\partial x} = 0 \tag{4.7}$$

$$\frac{\partial}{\partial x}\left(\frac{T_w - T}{T_w - T_b}\right) \tag{4.8}$$

$$\frac{dT}{dx} = \frac{dT_b}{dx} = \frac{dT_w}{dx} = const; \qquad Nu = f(Re, \mathrm{Pr}) \tag{4.9}$$

Thus in Fluent v.15 code periodic boundary conditions are set. The assumption of periodicity implies that the velocity components repeat themselves in space after a periodic length $\boldsymbol{L}$ in Eq.(4.10). Pressure can't be treated as the velocity but the pressure drop is the same after a periodic length $\boldsymbol{L}$ in Eq.(4.11). Thus also temperature behave such as the pressure having a periodic increase of bulk temperature σ after a periodic length $\boldsymbol{L}$ in Eq.(4.12).

$$\boldsymbol{u}(\boldsymbol{r}) = \boldsymbol{u}(\boldsymbol{r} + \boldsymbol{L}) = \boldsymbol{u}(\boldsymbol{r} + 2\boldsymbol{L}) = \cdots \tag{4.10}$$

$$\Delta p(\boldsymbol{r}) = p(\boldsymbol{r}) - p(\boldsymbol{r} + \boldsymbol{L}) = p(\boldsymbol{r} + \boldsymbol{L}) - p(\boldsymbol{r} + 2\boldsymbol{L}) = \cdots \tag{4.11}$$

$$\sigma = \frac{T(\boldsymbol{r} + \boldsymbol{L}) - T(\boldsymbol{r})}{L} = \frac{T(\boldsymbol{r} + 2\boldsymbol{L}) - T(\boldsymbol{r} + \boldsymbol{L})}{L} \tag{4.12}$$

$$\sigma = \frac{Q}{\dot{m} c_p L} = \frac{T_{b,out} - T_{b,in}}{L} \tag{4.13}$$

4.2.1. Central rod of the bundle

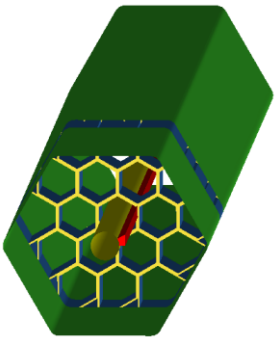

Fig. 4.8 Spacer rendering, only one rod is visible for displaying purpose, the red part is the domain.

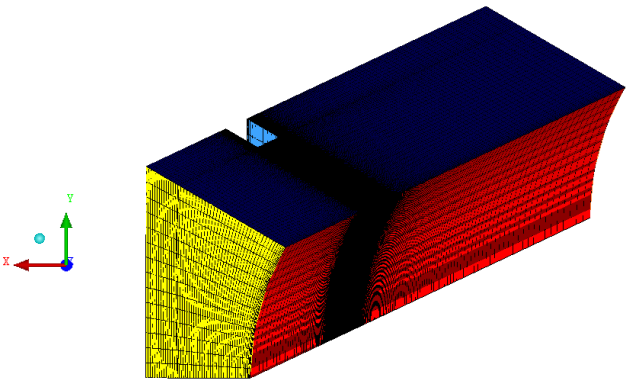

Fig. 4.9 Mesh domain is the red fluid zone in Fig. 4.8.

The first mesh is to study the fluid domain around the central rod of the bundle. Fig. 4.8 shows the entire spacer inside the hexagonal pipe. It is visible only the central rod for displaying purpose, the red zone next to the rod is the fluid domain. A domain detailed view showing the grid is available in Fig. 4.9. The yellow surface is the inlet, the red surface is the rod wall, the blue zone is one of the symmetry surfaces. The black part is the fluid zone close to the spacer wall, colors are not visible because the mesh lines become too thick. The top edge of the blue surface is interrupted by a little light blue step which is the spacer wall.

The dimples inside the spacer channels visible in Fig. 1.3 necessary to hold up rods are not used as shown in [14]. It reports the Nusselt number perturbation to the thermal field in an LBE cooled fast reactor gave from a grid spacer is not influenced by the presence of the pin fixers in the grid spacer, thus the choice to simplify the grid and build it without dimples.

The central rod channel passing through the honeycomb spacer is axial-symmetric, this allows to reduce fluid volume to a 30° angle of the entire rod. The fluid domain is a block structured mesh. Five blocks are necessary to have continuity to the surface nodes of each block. The block distribution is showed in Fig. 4.10. The shared surface which connect two blocks needs the same grid distribution, each cell on a surface of adjacent blocks needs to correspond to an other one in the adjacent block. This represents a problem, because it is difficult to mesh complicated geometries with block structured grids. The nodes number and their distribution in one block depends on the adjacent one and the blocks need also to be insert into the geometry.

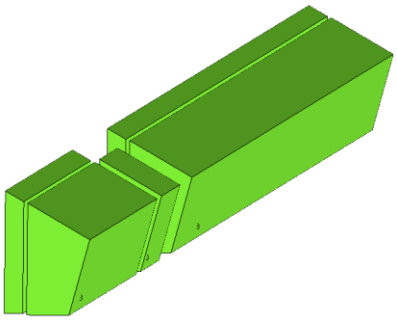

Fig. 4.10 Block distribution from the mesh showed in Fig. 4.9.

The models used in this thesis descripted in Chapter 3 are low Reynolds models, they require a cell center distance which corresponds to an $y^+ < 1$ in the first cell adjacent to the wall. Thus the mesh needs a refinement close to the rod surface which is visible in the yellow inlet section

in Fig. 4.9 and in the spacer wall. The y is predicted from the main flow characteristic using Eq.(4.14), where y is the first cell center distance, $u^*$is the friction velocity, $\tau_w$is the wall shear stress, $u_b$is the bulk velocity and $C_f$is the friction factor coefficient from the P. R. H. Blasius correlation for the pipe geometry in Eq.(4.15) the Reynolds number is calculated using the hydraulic diameter from Eq.(4.5).

$$y = \frac{y^+ \nu}{u^*}; \quad u^* = \sqrt{\tau_w/\rho}\ ; \quad \tau_w = \frac{1}{2}\,\rho\, C_f\, u_b^2 \tag{4.14}$$

$$C_f = \frac{0.316}{Re^{0.25}} \tag{4.15}$$

After the first evaluation of the wall cell thickness the other corrections are performed using the y^+ point value computed by Fluent. The critical points to evaluate the y^+ are inside the spacer channel, where the flow area decreases compared to the inlet surface area. Thus decreasing the flow area velocity increases and turbulence effect gains more relevance requiring a lower first cell thickness adjacent to the wall. From equations in (4.14), the bulk velocity u_b^2 increases, the Reynolds number increases too in Eq.(4.15) but its magnitude is not comparable to the velocity one, because they have different exponential factors, than the τ_w and consequently u^*increase. Leaving the remaining parameters constant, the y belonging to the cells adjacent to the spacer walls decreases. All simulations are performed with an $y^+ < 1$.

The geometry has an $\boldsymbol{x}$ and $\boldsymbol{y}$ extension two order of magnitude lower than the $\boldsymbol{z}$ extension, from the rendering in Fig. 4.8 and Fig. 4.9 is not visible the domain depth because is showed with an orthographic point of view and not prospective.

The near walls cell thickness is the y value which is obtained from the equations in (4.14). It is five order of magnitude lower than the domain main dimension ($\boldsymbol{z}$). Using an unstructured grid, cells, composed by prism and tetrahedral geometries, have all the three dimensions proportionate. Building the grid with these cell types the domain requires a cell number over $10e^6$, it is too much to perform several simulations in a short time with the available instrumentation. The alternative is to use hexahedral cells with a structured mesh. A cell can have a predominant dimension compared to the other two leaving all its boundary normal to the gradient and flows directions. This is not possible with tetrahedral or pyramidal cells because increasing only one cell dimension the cross-diffusion term gains too relevance compared to the gradient value.

The grid aspect ratio is one of the most used parameter used to define the cell distortion, considering a quadrilateral cell in the plane like in Fig. 4.11 with its edge named respectively a, b, c and d the aspect ratio (AS) is defined in Eq.(4.16), where for quadrilateral $n = 2$, for hexagonal $n = 3$ and $e_1 = (a + c)/2$ and $e_1 = (b + d)/2$.

$$AS = \frac{max(e_1, e_2, \dots, e_n)}{\min(e_1, e_2, \dots, e_n)} \tag{4.16}$$

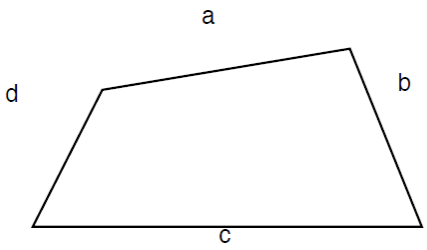

Fig. 4.11 Quadrilateral cell in the x-y plane.

The aspect ratio is equal to one when the cell respects the proportion of an ideal geometry (a square in this case), or it can rises to very high value when adjacent sides have different length. Taking the Icem definition in [26], it is the size of the minimum element edge divided by the size of the maximum element edge. The values are scaled and the default range of values is 1–20, such that an Aspect ratio of 1 indicates a regular element. The displayed result of the mesh in Fig. 4.9 is in Fig. 4.12.

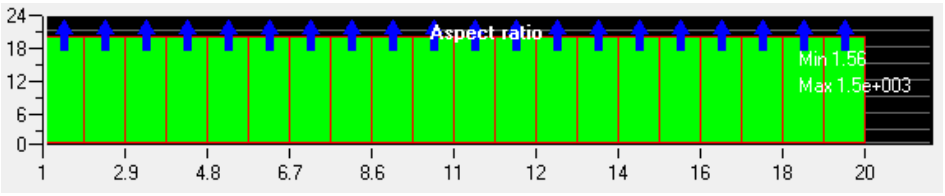

Fig. 4.12 Icem Aspect Ratio of the grid in Fig. 4.9.

According with the Aspect ratio criteria is clear that cell quality is not satisfying, but it isn't relevant. Hexahedral cells in this case have a predominant dimension along the main flow direction. The main mass flow, crossing these cells, is in a region far enough from the spacer to be said fully developed. This justifies the high Aspect ratio.

Thus, to ensure the mesh quality a different criteria is used for the Aspect ratio. It is the Quality criteria implemented by default in Icem [26]. In case of hexahedral cells: the Quality is a weighted diagnostic between Determinant (between -1 and 1), Max Orthogls (normalized between -1 and 1; if deviation from orthogonality is greater than 90 degrees, then the normalized value will be smaller than 0) and Max Warpgls (normalized between 0 and 1; warpage of 0 degrees is 1, warpage of 180 degrees is 0). The minimum of the 3 normalized diagnostics will be used. In case of prism cells: the Quality is calculated as the minimum of the Determinant and Warpage. Warpage is normalized to a factor between 0 to 1, where 90 degrees is 0, and 0 degrees is 1.

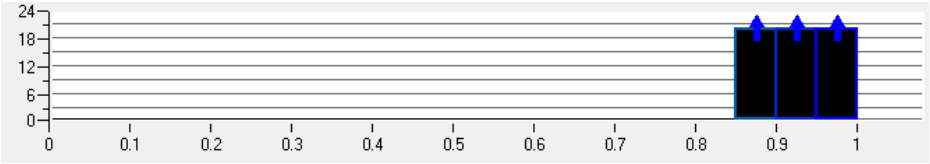

Fig. 4.13 Icem, Quality criteria applied to the grid in Fig. 4.9.

In Fig. 4.13 the ordinate axis shows the cells number, the arrow at the top of the columns means that it goes over the axis limit: every cell is displayed in the range between 0.85 and 1. According with the description at the paragraph beginning the grid in Fig. 4.9 has an excellent quality.

4.2.2. Complete grid

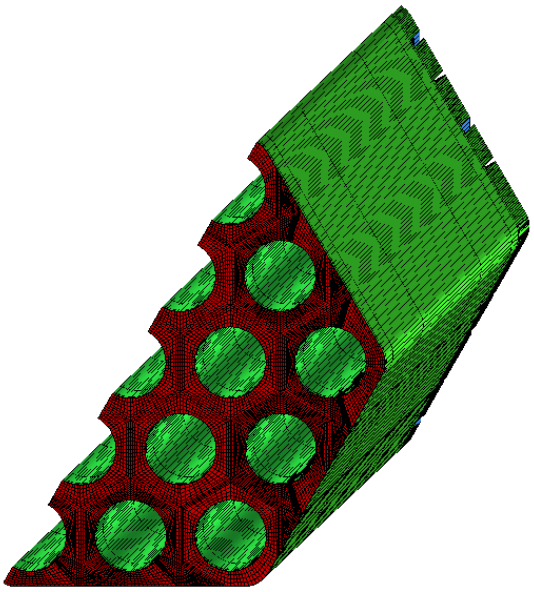

Fig. 4.14 First structured spacer grid.

The initial mesh is shown in Fig. 4.14. It isn't conceived to have an $y^+ < 1$ on the walls, with a cell thickness increase from the walls to the channels center. The blocks disposition doesn't allow a uniform cell distribution it can be seen at the inlet section in Fig. 4.14 there are some dark areas which mean a high cell concentration. It is also evident the minimal symmetric geometry isn't used, it can be still divided in three identical parts.

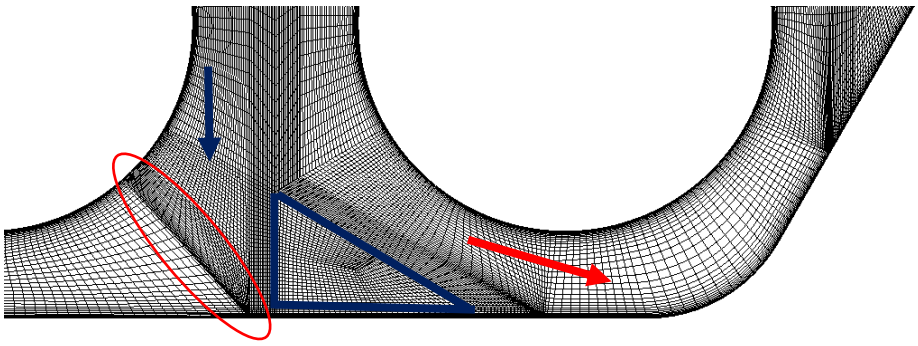

Fig. 4.15 Detailed grid of the bottom right corner of Fig. 4.14.

The view in Fig. 4.15 is the bottom right corner of Fig. 4.14. It has been set a $y^+ < 1$ on the rods walls and on the external wall. It's a main errors representative zone contained inside the grid.

1. Generally on the walls cells are denser compared to the remaining mesh areas. In Fig. 4.15 there are three zones, one of these is marked by a red ellipse which contains a dense cells area. These zones are inevitable in this approach. A high cells concentration in that position can compromise the simulation results. In this case simulations diverged after few iterations.

This happens when a block share only one point with a wall surface which has an $y^+ < 1$ refinement.

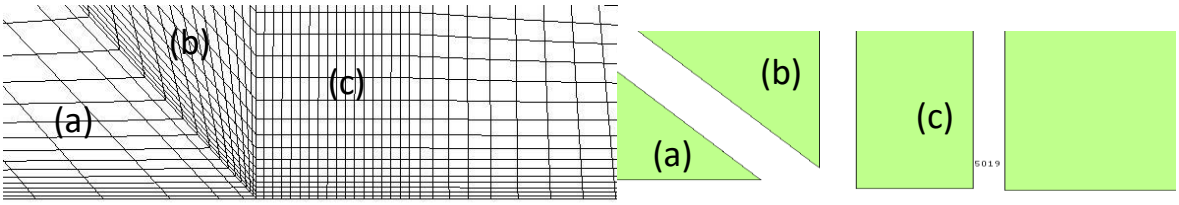

Fig. 4.16 detailed view of the highlighted area in Fig. 4.15.

In Fig. 4.16 blocks (a), (b) and (c) are highlighted. Blocks (a) and (c) have the bottom sides on the external wall with an imposed grid distribution. These blocks are connected to block (b), (they have the same nodes distribution on the shared side). It means that block (b) has its nodes distribution on both visible sides already determined by the neighboring blocks. The grid refinement is imposed by blocks (a) and (c) on block (b), thus the dense cells zone inside the domain highlighted by the ellipse in Fig. 4.15 is formed.

2. The red arrow in Fig. 4.15 crosses a dense mesh area and a coarse one successively. These areas are related to two different blocks the first shares one side with the rod wall, the second shares one side with the rod wall at the top and the opposite side with the external wall at the bottom. Those blocks are connected, they have the same nodes number at the interface. While the first block needs to supply only one wall refinement the second needs to supply two walls refinements using the same nodes number. This explains the two different cells density areas.
3. The blue arrow in Fig. 4.15 crosses two blocks and it marks a sudden grid refinement change. The denser block pointed out by the arrow is connected to the blocks inside the blue triangle. Those blocks need a high cells number which it's imposed to the block pointed out by the arrow. The blue triangle contains the grid which crosses the spacer inside the triangular channel visible in Fig. 4.8.

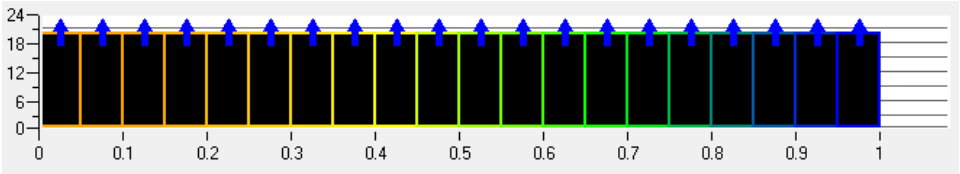

Fig. 4.17 Icem mesh Quality criteria from the mesh showed in Fig. 4.14.

The histogram in Fig. 4.17 shows a very low grid quality. The first columns inside the range from 0 to 0.2 are due to a wrong blocks associations, these columns represent cells with collapsed edges or with negative volumes. Blocks need to be correctly associated to the geometry surfaces, lines and points in order to reproduce all the geometrical details.

The new block disposition is made of 276 blocks instead the 210 of the previous one, the changing process brigs to have a more uniform grid visible in Fig. 4.19.

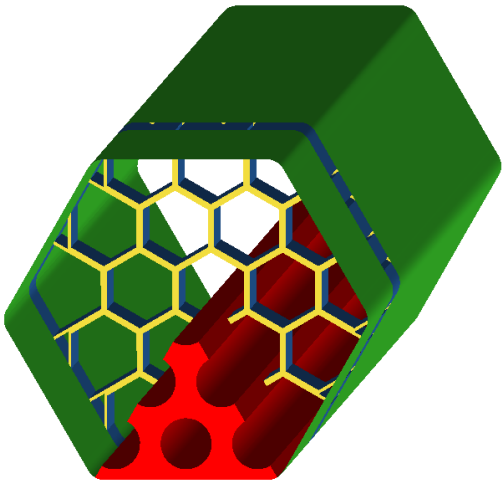

Fig. 4.18 spacer rendering with the new fluid domain which is the red part inside, rods are not displayed for viewing purpose.

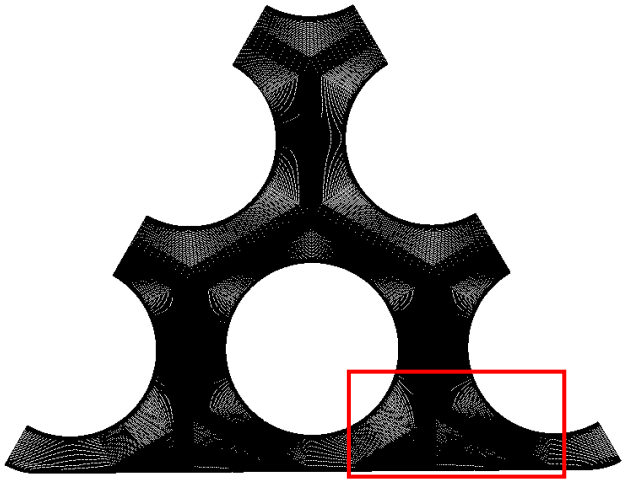

Fig. 4.19 frontal grid view of the red fluid domain in Fig. 4.18Fig. 4.19.

In Fig. 4.18 is showed the spacer grid inside its containing pipe, the red part is the new fluid domain, the spacer grid is axisymmetric every 60°, this allows to use three time less the cell number used in the first grid. The grid dense areas narrow and long in the fluid domain center of Fig. 4.19 are blocks placed in front of the spacer wall which is the yellow zone in Fig. 4.18. These areas need a thicker grid because the spacer wall has also a grid refinement with the $y^+ < 1$.

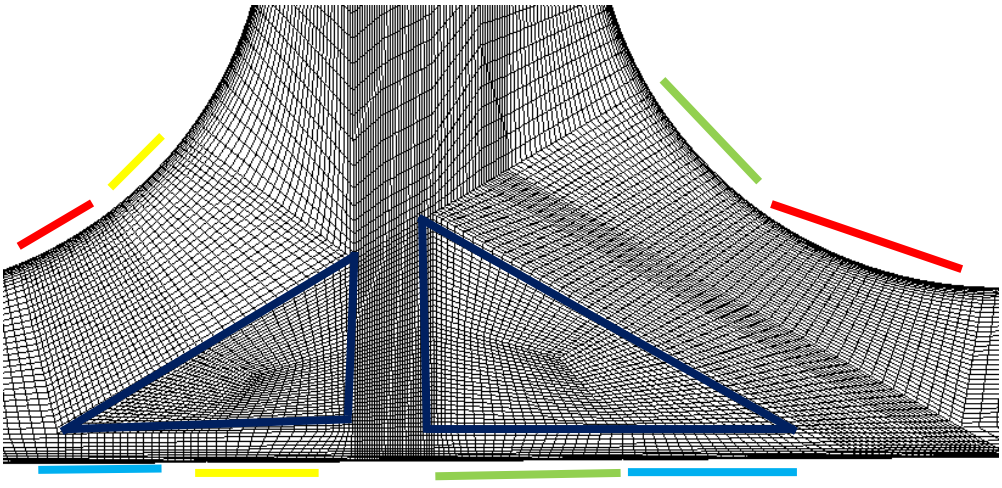

Fig. 4.20 Detailed view of Fig. 4.19 contained in the red rectangular.

The critical grid zone is the one contained in the red rectangular in Fig. 4.19. Here the changes for a more uniform grid distribution:

1. The solution of points 1 and 2 is to add a blocks layer on the external wall at the bottom side of Fig. 4.20. This allows an independent cell distribution close to the wall by the mesh above. Thus every boundary block facing with a wall in the domain have only a grid refinement in one direction.
2. In Fig. 4.20 the highlighted triangle on the right side is the same in Fig. 4.15, the one in the left side is added to give a more uniform grid distribution. Thus all the blocks surrounding the rods walls have a more uniform trapezoidal contour. The grid distribution become more symmetric. It also can be noticed the symmetry from the nodes number, lines with the same colors have the same nodes number in the blocks facing the boundaries.

The second solution is based on the block surface transformation in the x-y plane from structured mesh to unstructured. The surface is meshed with triangular and quadrilateral cells than is extruded along z direction, thus hexahedral and prismatic cells are formed. The mesh remain similar to the one showed in Fig. 4.19 except for the part inside the red rectangle which is showed in Fig. 4.21.

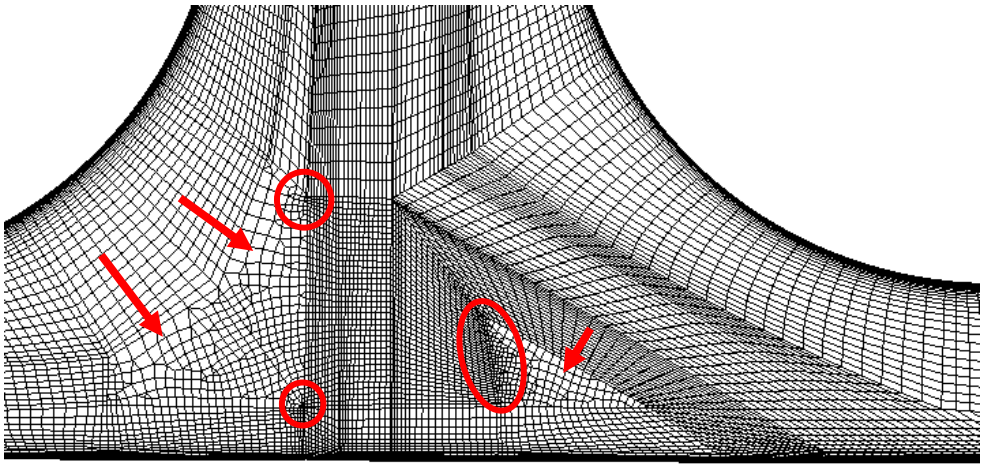

Fig. 4.21 Detailed view of Fig. 4.19 contained in the red rectangular, three central blocks are unstructured.

The advantage in unstructured blocks is that every block side can have different nodes number or have different geometrical contour. In Fig. 4.21 there is one triangular and two quadrilateral pointed out with the arrows. These blocks simplify the assembly breaking all connections highlighted with different colors in Fig. 4.20 making blocks independent by the adjacent blocks nodes number.

The problem of these kind of blocks is that the only control is the nodes number on each edge. On the blocks sides pointed by the arrows cells change their structures, they became suddenly bigger. In a good mesh every changes should be gradual. On the block side highlighted by the red circles the cell density is much higher compared to the neighboring structural mesh. The mesh quality in these zones isn't satisfying compared to the rest of the mesh. In Fig. 4.22 the columns inside the range from 0.2 to 0.4 represent the cells on the highlighted parts belonging to the unstructured blocks.

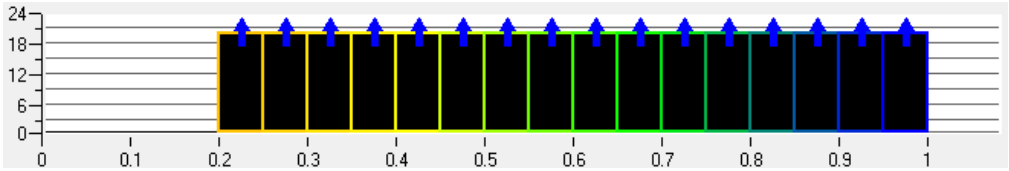

Fig. 4.22 Icem mesh Quality from the mesh showed in Fig. 4.21.

The Quality criteria from the grid in Fig. 4.20 is the one below in Fig. 4.23, is the best compromise found working on the grid the only other way to reduce the cells distortion without change the block disposition is to increase the cells number but going over the limits of 10 million cells simulations became too much slow.

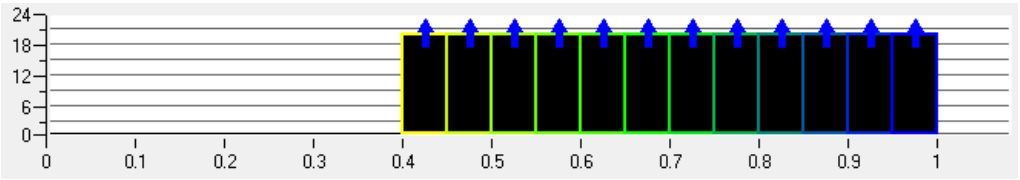

Fig. 4.23 Icem Mesh Quality from the mesh showed Fig. 4.20.

4.3. Fluent set up

The numerical simulations performed in this work have been computed assuming a steady-state. For the pressure and velocity coupling has been used SIMPLE algorithm.

The FLUENT 15 is set on pressure based solver. The diffusion terms are discretized with a central difference scheme and a second-order upwind scheme is used for the convective terms.

Buoyancy forces have been neglected and thermo-physical properties are considered constant. This hypothesis allows to decouple momentum equations from the energy one. First the simulation is computed only with momentum equations, when the convergence is reached is possible to compute energy equation with the turbulence energy model or correlations, keeping frozen the velocity field, k and ε. The solutions are considered converged when the following conditions are satisfied:

- Steady drag coefficient on the walls.
- Steady Nusselt number on the walls.
- Scaled residuals of continuity, momentum and turbulence parameters below 10^{-7}.

Velocity and temperature field have been considered fully developed, therefore at the inlet and outlet sections than were imposed periodic boundary conditions. For periodic condition has been imposed a specified mass flow rate in order to set the bulk velocity of each case.

Chapter 5

5. Results

The study on the rod bundle with grid spacer has been performed using several turbulence models to compute the flow field: the $k-\varepsilon\ AKN$ in Paragraph 3.2.2, the Menter $k-\omega\ SST$ in Paragraph 3.2.3 and the $k-\varepsilon-v^2-f$ in Paragraph 3.2.4. The Manservisi $k-\varepsilon-k_\theta-\varepsilon_\theta$ in Paragraph 3.3.3 has been used for the thermal field and the two correlations for the turbulent Prandtl Number respectively Kays in Paragraph 3.3.2 and Cheng in Paragraph 3.3.1.

The thermal turbulence model $k-\varepsilon-k_\theta-\varepsilon_\theta$ developed by Manservisi and Menghini has been tested against the DNS data in the channel and in the pipe geometry demonstrating a good data reproducibility. Results are showed in [2].

5.1. Validation of $\boldsymbol{k-\varepsilon-k_\theta-\varepsilon_\theta}$

Here follows $k-\varepsilon-k_\theta-\varepsilon_\theta$ validation previously performed by Manservisi and Menghini in [15]. Is the simple case of infinite rod bundle without spacers in periodic conditions at the inlet and outlet sections. A constant uniform imposed heat flow at the rods, in order to achieve a fully developed flow both thermal and hydrodynamic.

The geometry is based on a triangular array with a $p/d=1.3$ as showed in Fig. 5.1. The flow field is computed only with the AKN turbulence model from Paragraph 3.2.2, such as the simulations performed in the article where the energy turbulence model $k_\theta-\varepsilon_\theta$ is presented. In order to analyze the solution behavior, the solution T of the fully developed flow in Eq.(5.1), is usually written a sum of three terms:

$$T=\theta+T_c+\Delta T_m\ z \tag{5.1}$$

T_c is the constant temperature at the center of the triangular rod bundle $z=0$ and ΔT_m, the linear increase of temperature per unit of length in the vertical direction. In fully developed flow with constant heat flux on the wall, the temperature grows uniformly on horizontal section and linearly along the vertical direction. The slope of linear growth ΔT_m, can be easily computed with an energy balance as $\Delta T_m=\ \dot{q}/c_p\dot{m}$, where $\dot{q}$ is the heat flux on the wall and $\dot{m}$ the mass flux through the triangular bundle. Thus the non-dimensional temperature value is obtained in Eq.(5.2), where q is the heat surface flux.

$$\theta^*=\theta\frac{\lambda}{qD_{eq}} \tag{5.2}$$

The non-dimensional variable θ^* resemble the inverse of the local Nusselt number. Fig. 5.1 shows the lines where the temperature profile is plotted. Starting from vertical line (ab) the second and over the horizontal line (bc). The temperature is set to 0 in the coldest fluid domain point (a), till arrive to the maximum in the rod wall following the lines (ab) and (bc). The reference value in the plots legend are results of $k-\varepsilon-k_\theta-\varepsilon_\theta$ taken from [15] computed by the authors.

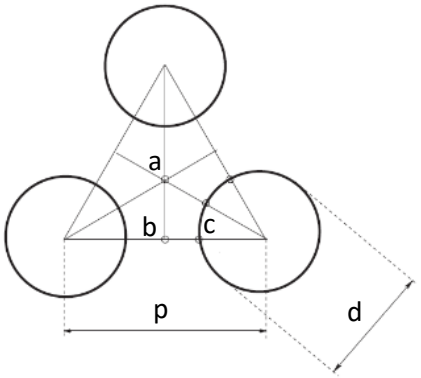

Fig. 5.1 Ab, bc and cd lines on a triangular rod bundle lattice.

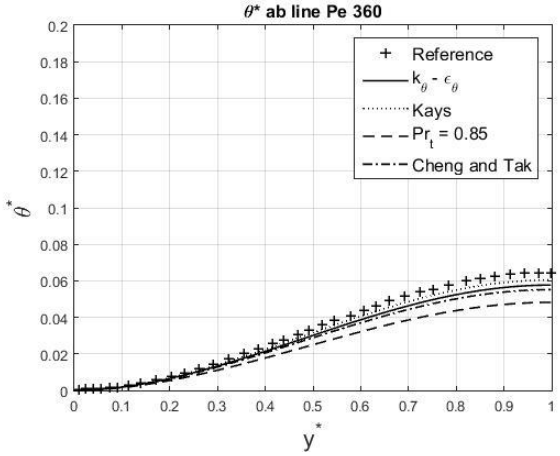

Fig. 5.2 Theta star, ab line Pe=360, p/d=1.3.

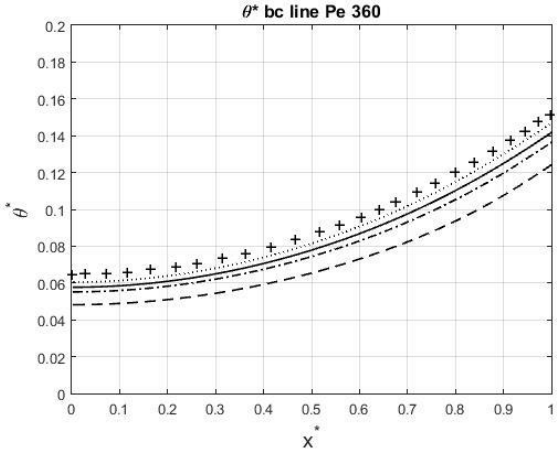

Fig. 5.3 Theta star bc line Pe=360, p/d=1.3.

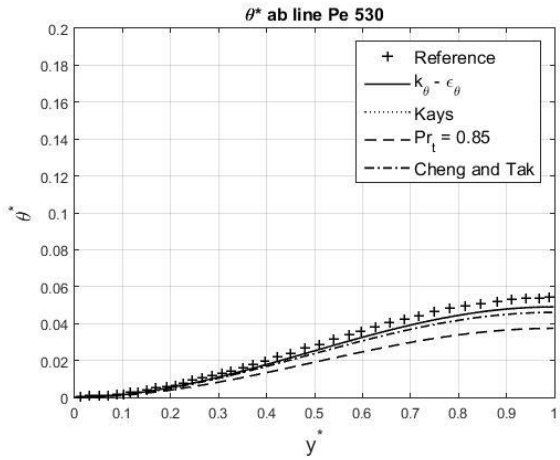

Fig. 5.4 Theta star ab lin,e Pe=530, p/d=1.3.

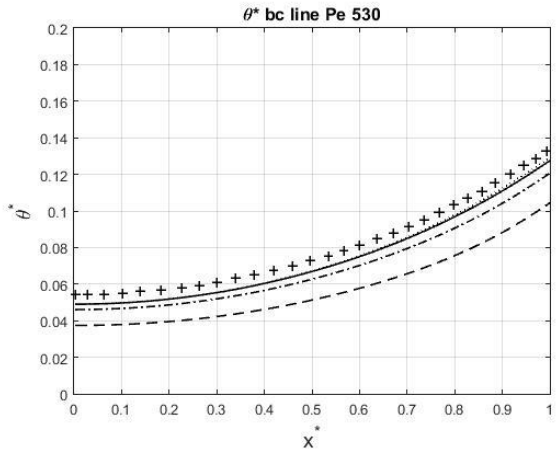

Fig. 5.5 Theta star, bc line Pe=530 p/d=1.3.

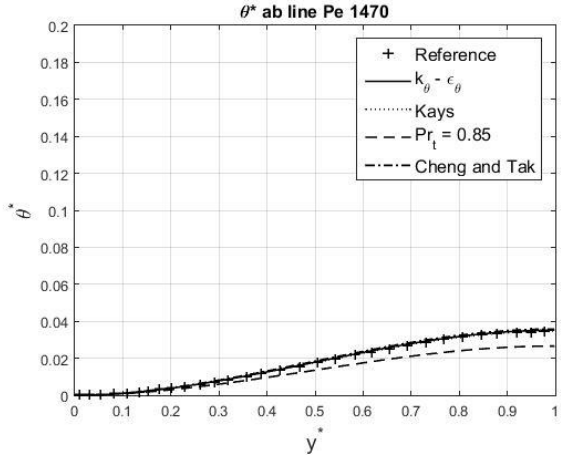

Fig. 5.6 Theta star, ab line Pe=1470, p/d=1.3.

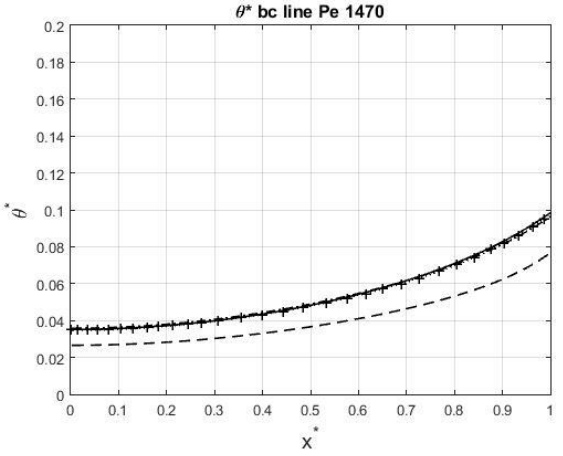

Fig. 5.7 5.8 Theta star, bc line Pe=1470 p/d=1.3.

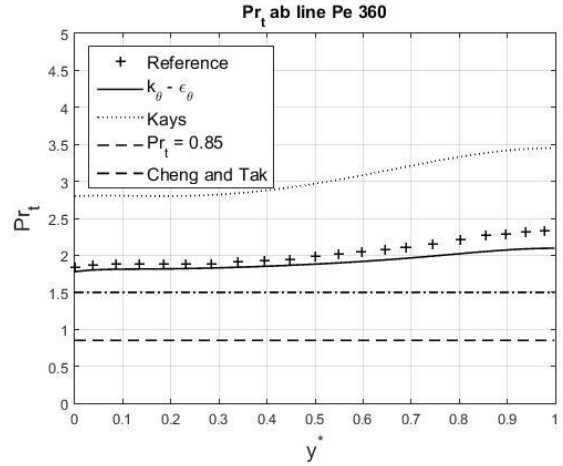

Fig. 5.9 5.10 Turbulent Prandtl ab line Pe=360 p/d=1.3.

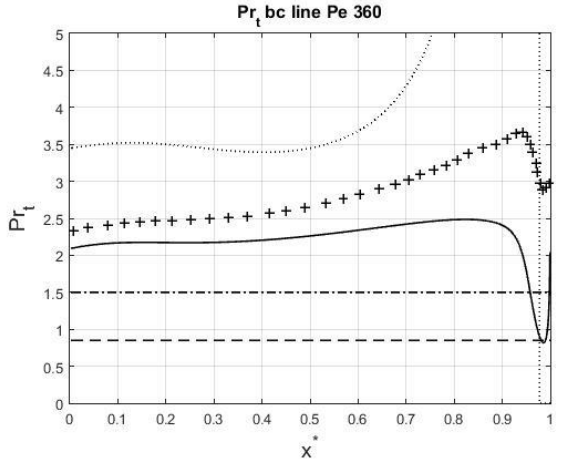

Fig. 5.11 Turbulent Prandtl line Pe=360 p/d=1.3.

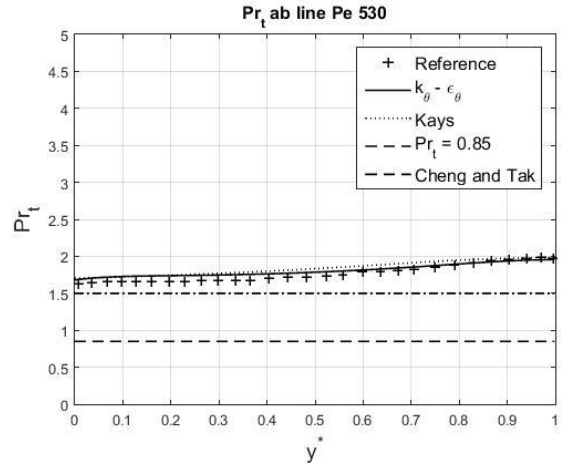

Fig. 5.12 Turbulent Prandtl ab line Pe=530 p/d=1.3.

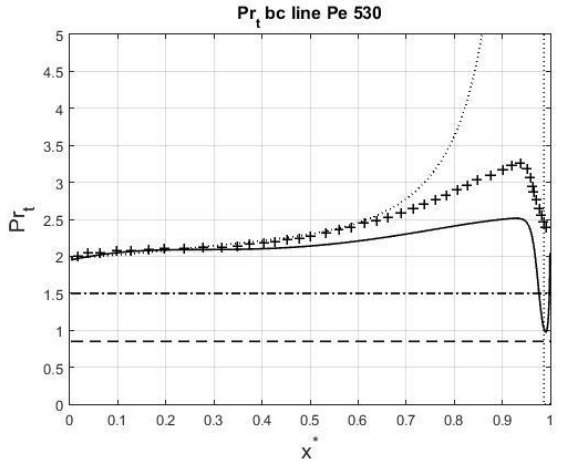

Fig. 5.13Turbulent Prandtl bc line Pe=530 p/d=1.3.

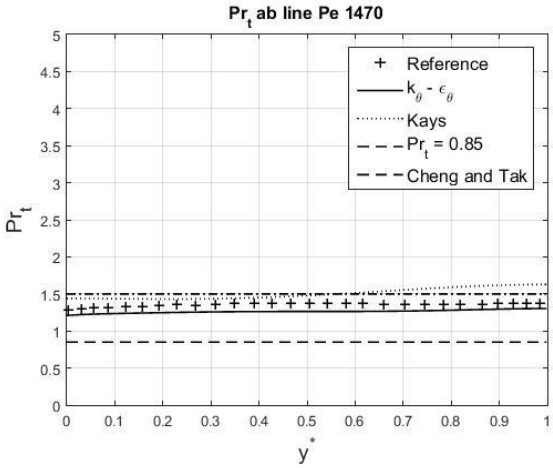

Fig. 5.14 Turbulent Prandtl ab line Pe=1470 p/d=1.3.

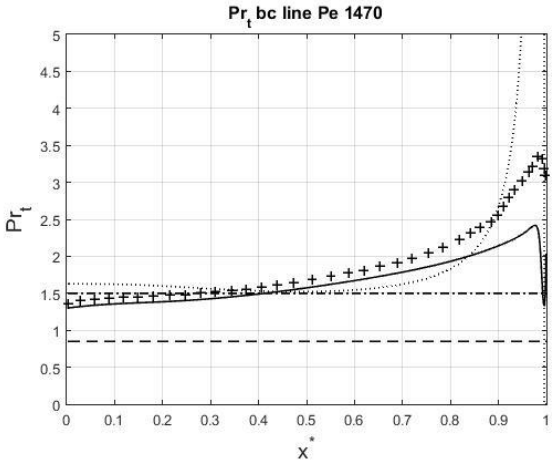

Fig. 5.15 Turbulent Prandtl bc line Pe=1470 $p/d = 1.3$

Simulation have been computed for three different Péclet numbers, respectively ($Pe = 360, 530, 1470$). The energy equation has been launched a posteriori, thus each Péclet number case has an identical velocity profile varying the turbulent thermal models. The greatest turbulent Prandtl values are visible for the lowest turbulent flow regime. In the low Péclet numbers case the influence of laminar conductivity is more relevant compared to the turbulent effects. Fig. 5.9 and Fig. 5.11 show the turbulent Prandtl number for the Pe=360, the greatest value is given by the Kays correlation and is the 66% greater than the value computed by the model $k_\theta - \varepsilon_\theta$ it is considered the rod bundle central zone on the ab line because close to the wall it diverges to infinite. The near wall turbulent Prandtl trend is not relevant because is a fluid region dominated by laminar effects which have a greater magnitude compared to the turbulent ones. The value reported in the article computed by Manservisi and Menghini differs at maximum of the 14% in the ab line. The turbulent Prandtl number computed by Cheng and Tak is constant in all the domain and underestimate the $k_\theta - \varepsilon_\theta$ 28% of its maximum value in the ab line. The turbulent Prandtl number of 0.85 is lower than the half of the value in the ab line.

The temperature profiles for the $P\acute{e} = 360$ are visible in Fig. 5.2 and Fig. 5.3 while the Cheng and Kays correlations differ of -4% and $+4\%$ respectively from the $k_\theta - \varepsilon_\theta$, in the temperature maximum value on the wall $x^* = 1$. The temperature profile computed with a $Pr_t = 0.85$ differs from 13.5%. Taking into account the $P\acute{e} = 530$, the turbulent Prandtl number profiles in Fig. 5.12 and Fig. 5.13 have a lower value compared to the previous ones. Analyzing the ab line in detail the one computed using Kays correlation and the one computed by Manservisi fit well the $k_\theta - \varepsilon_\theta$ model. The Cheng correlation give the same value of the previous case which differs from the $k_\theta - \varepsilon_\theta$ of the 25% in $y^* = 1$. The $Pr_t = 0.85$ differs from the 57.5% in the same point.

The related temperature profiles are in Fig. 5.4 and Fig. 5.5, taking the $k_\theta - \varepsilon_\theta$ as a reference profile, the Kays profile fit perfectly, the one computed by Manservisi is the 4% greater, while the Cheng correlation gives a 5% lower profile always considering the warmest point in $x^* = 1$.

In the last $P\acute{e} = 1470$ case the turbulent Prandtl profiles in Fig. 5.14 and Fig. 5.15 show the lowest profile values compared to the previous cases, the values on the $y^* = 1$ vary form a

maximum of 1.7 from the Kays correlation to a minimum of 1.3 from the $k_\theta - \varepsilon_\theta$. The relative temperature profiles are in Fig. 5.6 and Fig. 5.7, except the one from the turbulent Prandtl set to 0.85 the others fit perfectly with an univocal trend. The Péclet number increase correspond to a turbulence rate increase and the different Turbulent Prandtl numbers predicted decrease and collapse together till ideally reach 0.85 value. The temperature profiles decrease and collapse too. These results show that Kays and Cheng correlations give both a reliable turbulent Prandtl number profiles such as the $k_\theta - \varepsilon_\theta$.

Results quality is still confirmed from the average Nusselt number reported in Table 5.1, derived using Eq.(4.3).

Table 5.1 Nusselt number varying the Péclet number and the models.

$Nu(Pé)$	$k-\varepsilon-k_\theta-\varepsilon_\theta$	$Kays$	Cheng and Tak	$Pr_t = 0.85$
$Pe = 360$	12.7541	12.3888	13.0935	14.1075
$Pe = 530$	13.7847	13.5462	14.4872	16.2229
$Pe = 1470$	17.4173	17.6515	18.1672	22.1574

The Kays correlation result showed in [15] is much different. The predicted Nusselt for a Pé=1470 is 29.64. Fig. 5.16 and Fig. 5.17 show the R form equations in (3.52), it is the ratio between the thermal turbulent characteristic time and the dynamical turbulent characteristic time. It is displayed in the ab and bc lines of Fig. 5.1. The plots show the three Péclet number cases computed with the $k_\theta - \varepsilon_\theta$ and the respective three cases computed by Manservisi. On the ab line the trend show a local maximum value at the center plot, while the absolute maximum is in the near wall region on the bc line. The increased turbulence rate causes an upper profile translation emphasizing the maximum value compared to the two relative minimum values. Tacking into account same Péclet numbers cases profile are not coincident. The maximum variation is in the greatest Péclet number case in the near wall region. That region is dominated by laminar effects and differences can be neglected. On the central channel ab line the greatest differences are in $y^* = 1$ In the Pé=360 the difference is the 37% of the computed value for Pé= 530 the difference is the 35% and the greatest Pé=1470 is the 20%.

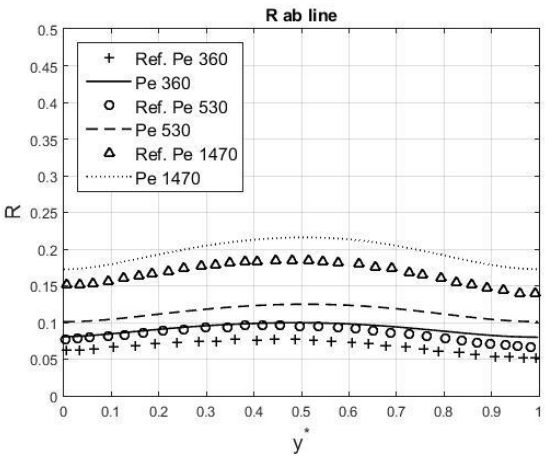

Fig. 5.16 R, ab line, p/d=1.3.

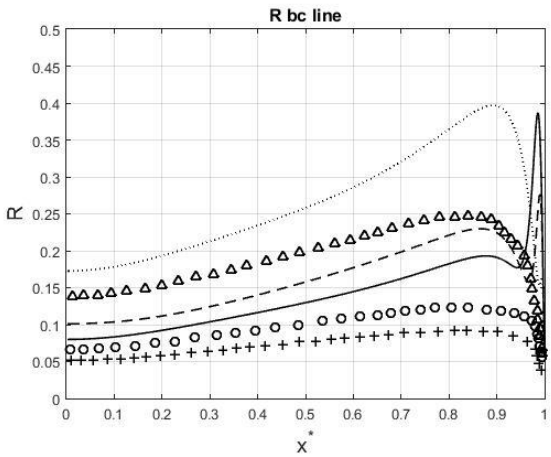

Fig. 5.17 R, bc line, p/d=1.3.

The non-dimensional root mean square temperature is defined Eq.(5.3), where k_θ is the average square temperature fluctuations in Eq.(3.39).

$$\theta_{rms} = \lambda \frac{\sqrt{2k_\theta}}{qD_h} \tag{5.3}$$

The profiles in Fig. 5.18 and Fig. 5.19 are shown respectively along the ab and bc lines. On the ab line profiles show a relative maximum value at the line center, with two minima values on $y^* = 0$ and $y^* = 1$, while on the bc line profile starts with a relative minimum on the $x^* = 0$, grows till reach an absolute maximum and decrease till becomes 0 on the rod wall in $x^* = 1$. The profile are for three different Péclet numbers $Pe = 360, 530, 1470$, the last profile are the Mnaservisi's results for the $Pe = 530$, which are visible onlu in Fig. 5.19 close to $x^* = 1$. Its results magnitude are 10 times greater than the ones computed in this thesis it is probably due to an error in the dimensionless process. The Pe=360 and Pe=1470 results match on the ab line while on the Pé=530 has a greater value. On the bc line the trend is similar in the central channel region from $x^* = 0$, to $x^* = 0.5$. Afther that region from $x^* = 0.5$, to $x^* = 1$ the trend values decreases with the Péclet number.

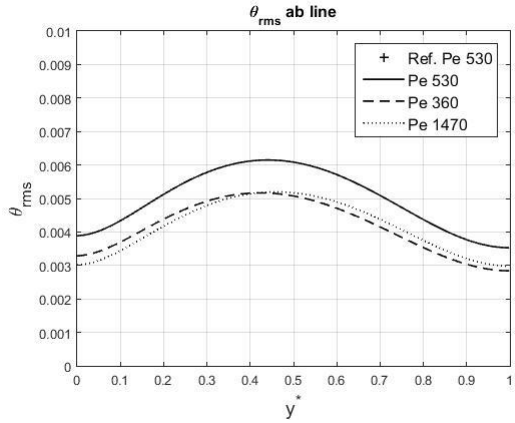

Fig. 5.18 Theta rsm, ab line, p/d=1.3.

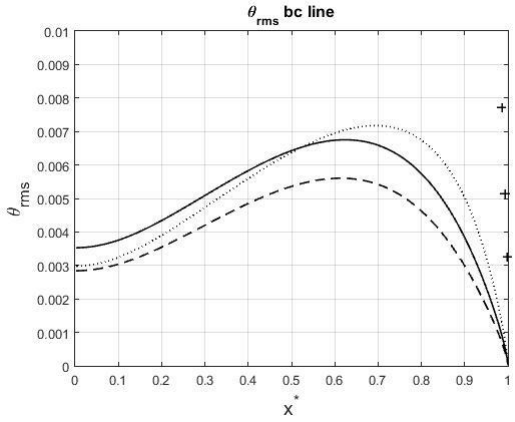

Fig. 5.19 Theta rsm, bc line, p/d=1.3.

5.2. Central bundle rod results

Here follows the results computed from the mesh descripted in Paragraph 4.2.1. The flow field has been computed using the three models in Paragraph 3.2, the results show the non-dimensional velocity u/u_{bulk} and the turbulent viscosity ratio ν_t/ν against the non-dimensional $x-coordinate\ x^+$ from Eq.(3.3). Values are taken in a fully developed region upstream the spacer, in the Fig. 5.1 ab line, which is orthogonal to the rod surface.

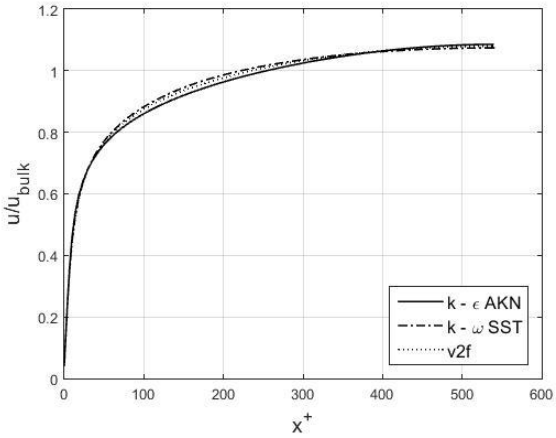

Fig. 5.20 Dimensionless velocity against x plus ,Pe=1500, bc line, infinite rod bundle with spacer, z/Dh=-5.

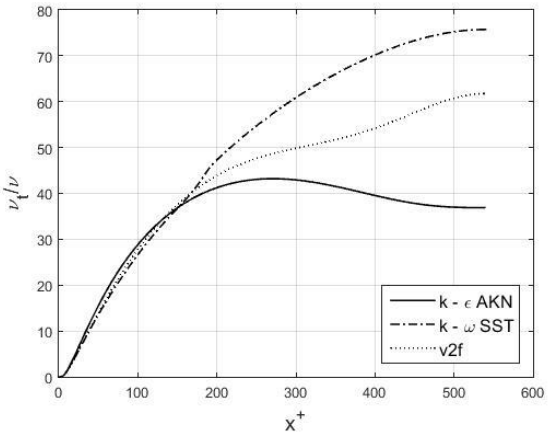

Fig. 5.21 Turbulent viscosity ratio against x plus, Pe=1500, bc line infinite rod bindle with spacer, z/Dh=-5.

Fig. 5.20 is the velocity profile and the turbulent viscosity ratio is in Fig. 5.21. To a flatter velocity profile corresponds a greater turbulent viscosity value. The profile computed by the v2f model has been taken as references. The models differ in the log region where the turbulence become relevant. In x^+range between 0 and 300 there are the greatest difference: the $k-\varepsilon$ AKN underestimate the v2f of the 4.1% while the $k-\omega\ SST$ is the 1.09% greater. On x^+=400 the trend is inverted the $k-\varepsilon$ AKN computes the greater and the $k-\omega\ SST$ the smaller values.

The turbulent viscosity ratio trend in Fig. 5.21 is univocal for the three models in an x^+ range between 0 and 160, after that all the three curves diverge, the greatest difference between the v2f and the $k-\varepsilon$ AKN is 40% while the greatest difference between the v2f and the $k-\omega\ SST$ is the 29%.

In the same flow section follow the non-dimensional temperature from Eq.(5.2) and the turbulent Prandtl number from Eq.(2.18) in the ab, bc and cd lines showed in Fig. 5.1.

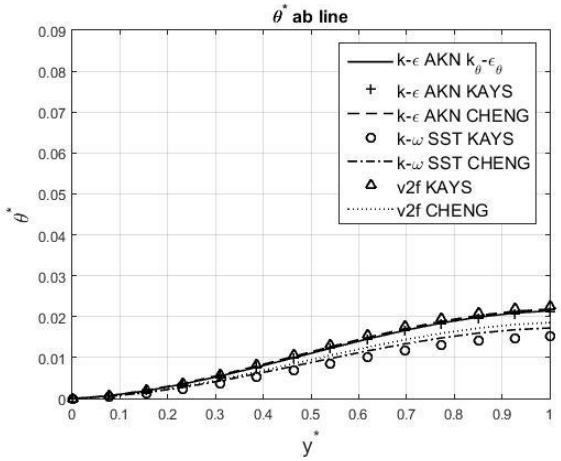

Fig. 5.22 theta star ab line Pe=1500, infinite rod bundle with spacer z/Dh=-5.

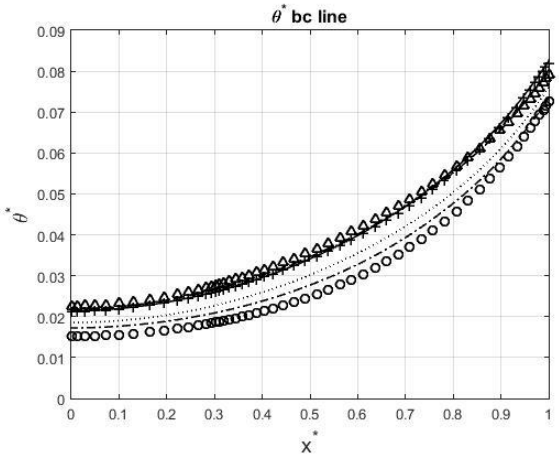

Fig. 5.23 Theta star bc line Pe=1500, infinite rod bundle with spacer, z/Dh=-5.

Fig. 5.22 is the temperature profile on the ab line, the $y^* = 0$ on the point a is the coldest point into the channel center. $T(y^* = 1) = T(x^* = 0)$, is the b point belonging to both lines. The temperature profile increases to the rod wall intersection in b which corresponds to the warmest lines point. The $k - \varepsilon\ AKN\ k_\theta - \varepsilon_\theta$, $k - \varepsilon\ AKN\ KAYS$, $k - \varepsilon\ AKN\ CHENG$ and $v2f\ KAYS$ have an univocal, the greatest difference is computed by the $k - \omega\ KAYS$.

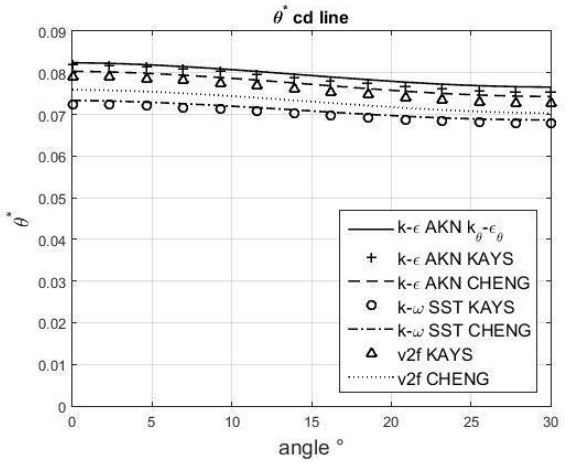

Fig. 5.24 Theta star, *cd line, Pe=1500, infinite rod bundle with spacer, z/Dh=-5.*

On the wall line cd in Fig. 5.24, $T(angle\ 0°) = T(x^* = 1)$. The temperature profiles show a different temperature distribution on the wall from the warmest point in $angle\ 0°$ temperature decrease up to the coldest wall point on $angle\ 30°$

Fig. 5.25 and Fig. 5.26 show the turbulent Prandtl value respectively on the ab and bc lines. The Cheng correlation being function of the mean Péclet number which is the same for every simulation (Pe=1500) gives a constant turbulent Prandtl for each flow turbulent model equal to 1.5. Kays correlation is function of the turbulent viscosity ratio thus is a space dependent turbulent Prandtl. The $k - \varepsilon\ AKN\ KAYS$, the $v2f\ KAYS$ and CHENG have a similar trend varying from 1.45 to 1.7 on the ab line while the $k - \varepsilon\ AKN\ k_\theta - \varepsilon_\theta$ and $k - \omega\ SST\ KAYS$ have a lower value trend varying from 1.2 to 1.3 always in the ab line.

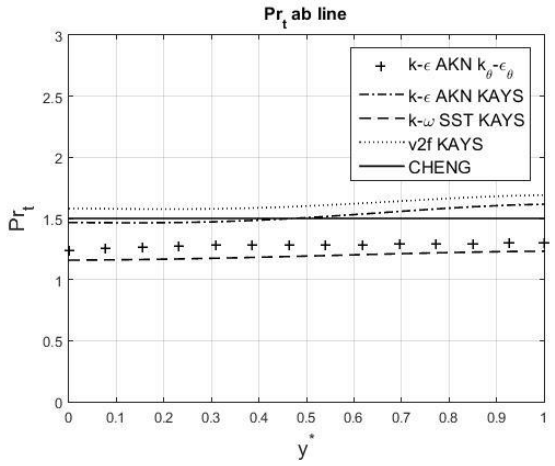

Fig. 5.25 Turbulent Prandtl ab line Pe=1500, infinite rod bundle with spacer, z/Dh=-5.

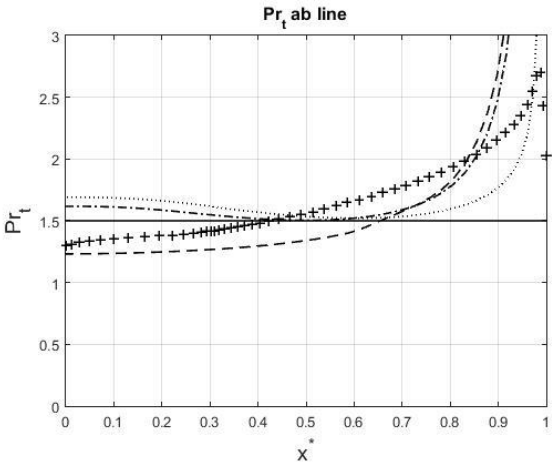

Fig. 5.26 Turbulent Prandtl number bc line Pe=1500, infinite rod bundle with spacer, z/Dh=-5.

Fig. 5.27 and Fig. 5.28, show the non-dimensional temperature profile respectively on the ab and bc lines. The displayed model is the $v2f\ KAYS$, the temperature profile is displayed varying the mean Péclet number and leaving all the remaining parameters constant. Increasing the Peclét number the temperature values decreases with an exponential law, the profile trend becomes flatter. The warmest point on the c point $(y^* = 1)$ has a $\theta^* = 0.106$ value belonging to the $Pe = 500$, while the warmest point relative to the maximum Péclet number $(Pe = 2500)$ is $\theta^* = 0.067$.

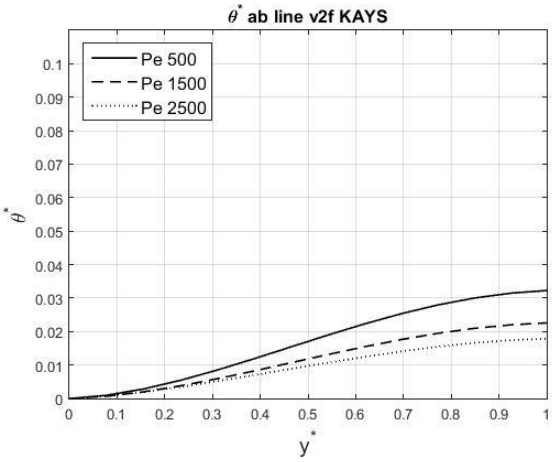

Fig. 5.27 Theta star ab line v2f KAYS, infinite rod bundle with spacer, z/Dh=-5.

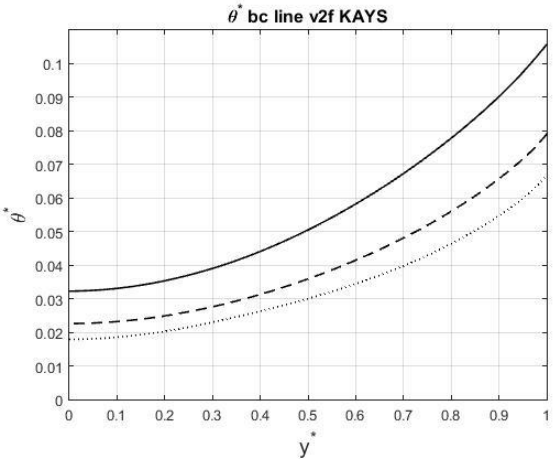

Fig. 5.28 Theta star bc line v2f KAYS, infinite rod bundle with spacer, z/Dh=-5.

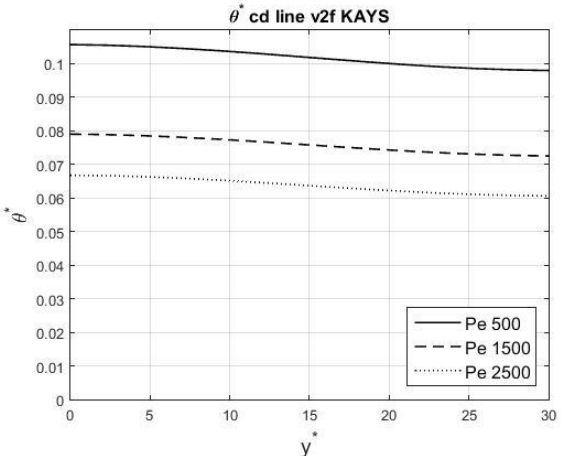

Fig. 5.29 Theta star bc line v2f KAYS, infinite rod bundle with spacer, z/Dh=-5.

Fig. 5.29 is the wall temperature profile varying the Péclet number. Such as in the ab and bc lines the trend profile becomes more flat increasing the Pé number, the greatest rod temperature difference with a $Pe = 500$ is $\Delta\theta^* = 0.067$, while the greatest Péclet number difference is $\Delta\theta^* = 0.061$.

Fig. 5.30 is the rod wall temperature plotted along the main flow direction which is pointed out by the arrow in Fig. 4.7. The axial coordinate 0 has been set on the spacer inlet and the temperature 0 value has been set at the domain inlet, at $z/D_h = -10.54$. The grey zone highlights the axial spacer length, the dotted green line identify the plane 2.5 mm upstream the spacer where thermocouples are placed in the experiment performed at KALLA laboratory.

The wall temperature plotted is the integral temperature calculated at each axial coordinate z. Dimensional temperature T has been transformed to non-dimensional using the Eq.(5.2) where $\theta = T - T(z/D_h = -10.54)$. In Fig. 5.30 flow turbulence models are grouped with the same colors and thermal turbulence model are grouped with the same line type.

The temperature profiles start with an univocal trend. Upstream the spacer in the green line intersection the temperature profiles show a local maximum point. The temperature sampled by thermocouples is in region influenced by the spacer. Inside the spacer every temperature profiles have a different local minimum point. Every model gives different values. Downstream the spacer temperature profiles converge again in a univocal trend.

The wall temperature inside the spacer decreases because inside the spacer the flow area decreases, the mean velocity increases with the turbulence rate and this process emphasize the convective heat exchange which makes the rod colder.

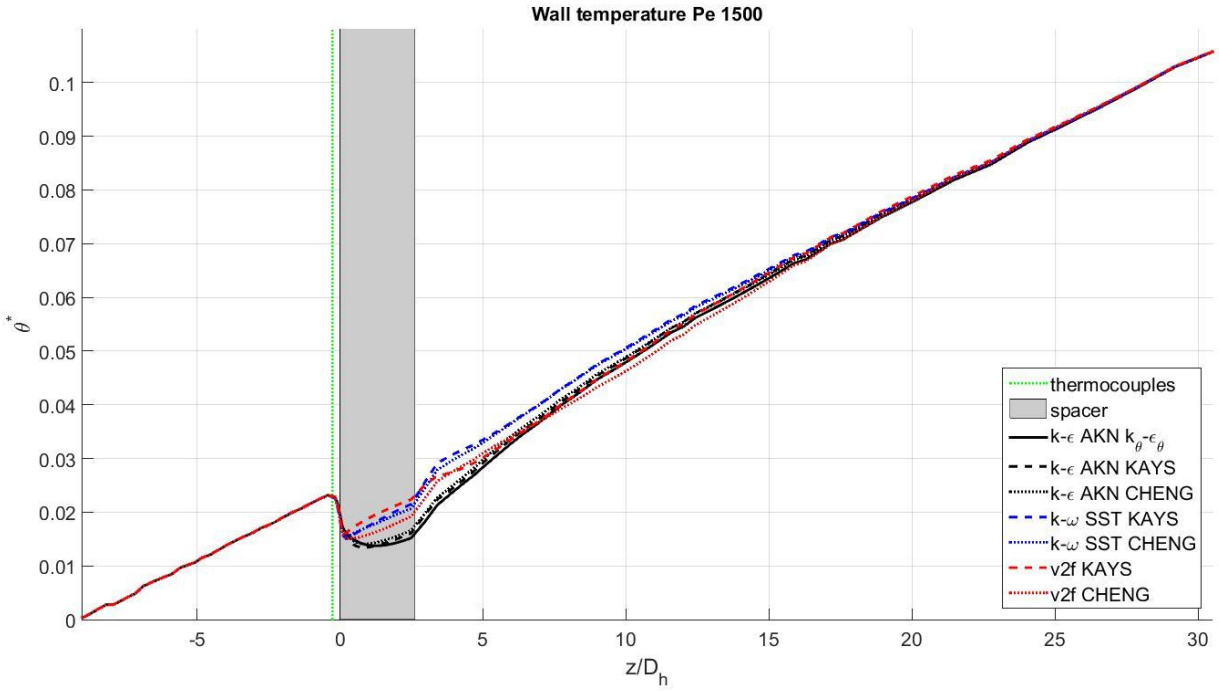

Fig. 5.30 Wall non-dimensional temperature profiles z-coordinate, Pe 1500 infinite rod bundle with spacer.

Fig. 5.31 is the local Nusselt number computed using Pe=1500, is plotted along the main flow direction z. The Nusselt number is derived from Eq.(4.3), and Eq.(4.1). Upstream the spacer the Nu has a flat profile, it confirms that the temperature field is fully developed, thus also the velocity field. The intersection between Nusselt profiles and the green line has a value slightly greater than the undisturbed value, the maximum variation is lower than 1.5%, compared to the undisturbed value. It isn't relevant compared to the maximum variation visible using different models. The greatest Nusselt number belonging to the $k-\omega\ KAYS$ is 20.81, the smallest from $k-\varepsilon\ AKN\ k_\theta-\varepsilon_\theta$ is 19.05, taking the values on the green line intersection. Inside the spacer every model has different values but same flow turbulence models have a similar trend profiles.

The $k-\varepsilon\ AKN$ is plotted with the black profiles it has a monotonous growth from the spacer inlet section and it reaches an absolute maxima values on the spacer outlet section. Dowstream the spacer the Nusselt profiles have a monotonous decrease. The CHENG correlation shows a completely flat profile passed $z/D_h = 20$, while the $k_\theta-\varepsilon_\theta$ model still decreases slightly of about 1.3% the value measured on the green line intersection, passed the 20 hydraulic diameters. The KAYS correlation has a little increasing trend after 20 hydraulic diameters lower than 0.5%.

The $k-\omega\ SST$is plotted with the blue profiles, on the CHENG case it has a relative maxima value close to the spacer inlet section and one absolute value close to the outlet section, KAYS has the relative one on outlet section and the absolute one on the inlet section. Downstream the spacer the KAYS correlation shows a relative minimum and maximum value file across $z/D_h = 5$ therefore decreases and becomes flat again close to the grid outlet section. The CHENG correlation instead show a monotonic decreasing Nusselt profile. Passed $z/D_h = 20$ the variation are lower the 2% the reference value on the green line intersection

The $v2f$ Nussel profiles results which are plotted with the red profiles, on the KAYS correlation it has a double maximum inside the spacer close to the inlet and outlet section which are approximately of the same magnitude. Downstream the spacer a relative maximum and minimum values respectively on $z/D_h = 4\ and\ 3$, thereafter the profile decreases and becomes flat after $z/D_h = 20$ with a damped oscillation lower than 4% the value of the reference value. The case using the CHENG correlation has a monotonic growth form the spacer inlet section with an absolute maximum value near the spacer outlet section, after that it show a monotonic decrease trend which become completely a flat profile passed the 20 hydraulic diameters. From a general point of view passed the 20 hydraulic diameter the Nusselt profiles can be considered flat, they still have a residual damped oscillation lower than 4% into the worst case.

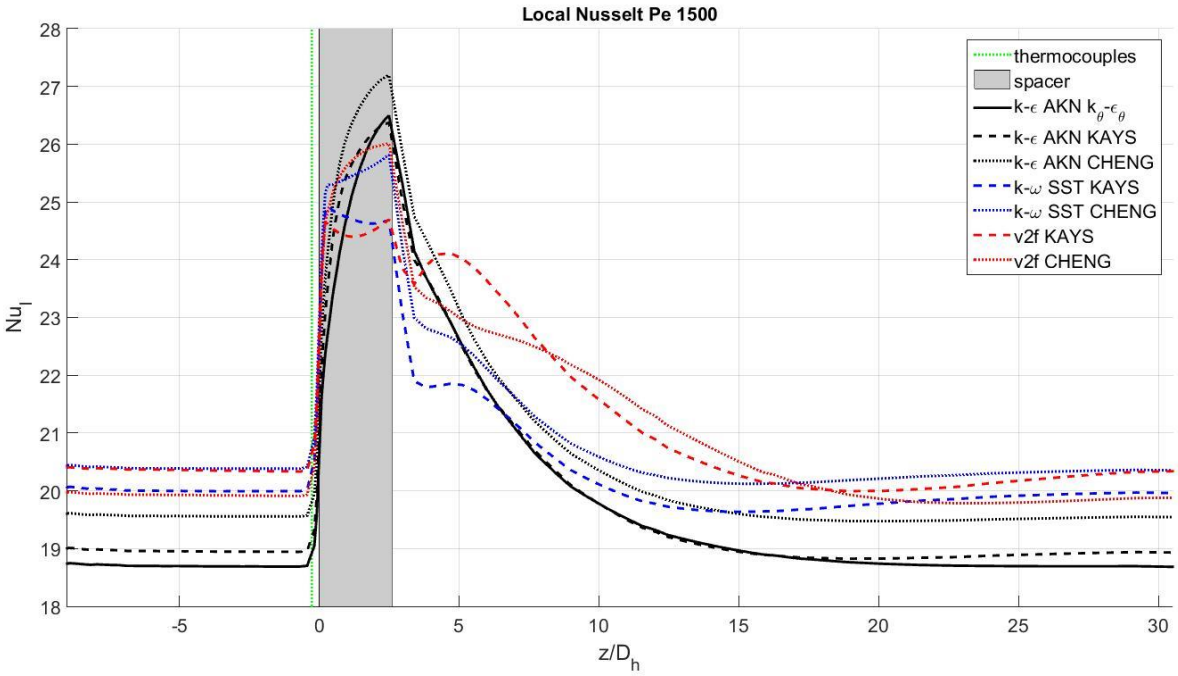

Fig. 5.31 Local Nusselt number Pe 1500, infinite rod bundle with spacer.

Fig. 5.32 are Nusselt profiles using the same models with a Péclet number of 500. The maximum variation measured on the green line varies from a minimum of 14.4 belonging to the $k-\varepsilon\ AKN\ KAYS$ and a maximum value of 15.98 belonging to $v2f\ KAYS$.

The $k-\varepsilon\ AKN$ plotted with the black profiles respects the trend descriped in the previus case ($Pe = 1500$). The difference inside the spacer can be noted on the Nusselt maximum value which, for KAYS and the $k_\theta - \varepsilon_\theta$ in Fig. 5.31 is similar and in this case the $k_\theta - \varepsilon_\theta$ is much closer to the CHENG maximum value. The Nusselt profiles downstream the spacer decrease and became completely flat passing $z/D_h = 15$, the remaining damped oscillations are lower than 0.1% the value measured on the green line interseciton.

The $k-\omega\ SST$ profiles have a trend similar to the $k-\varepsilon\ AKN$ with a single maximum close to the spacer outlet section which is reached after a monotonic growth, downstream the spacer the Nusselt profile decrease and became flat at $z/D_h = 13$.

The v2f on the gren profile shows only with the KAYS correlation a double maxima values one realtive and one absolute inside the spacer, downstream the spacer become flat after $z/D_h = 15$. The CHENG correlation has a monotonic growing profile with the maximum close the spacer outlet section and the Nusselt profile become flat passing $z/D_h = 20$.

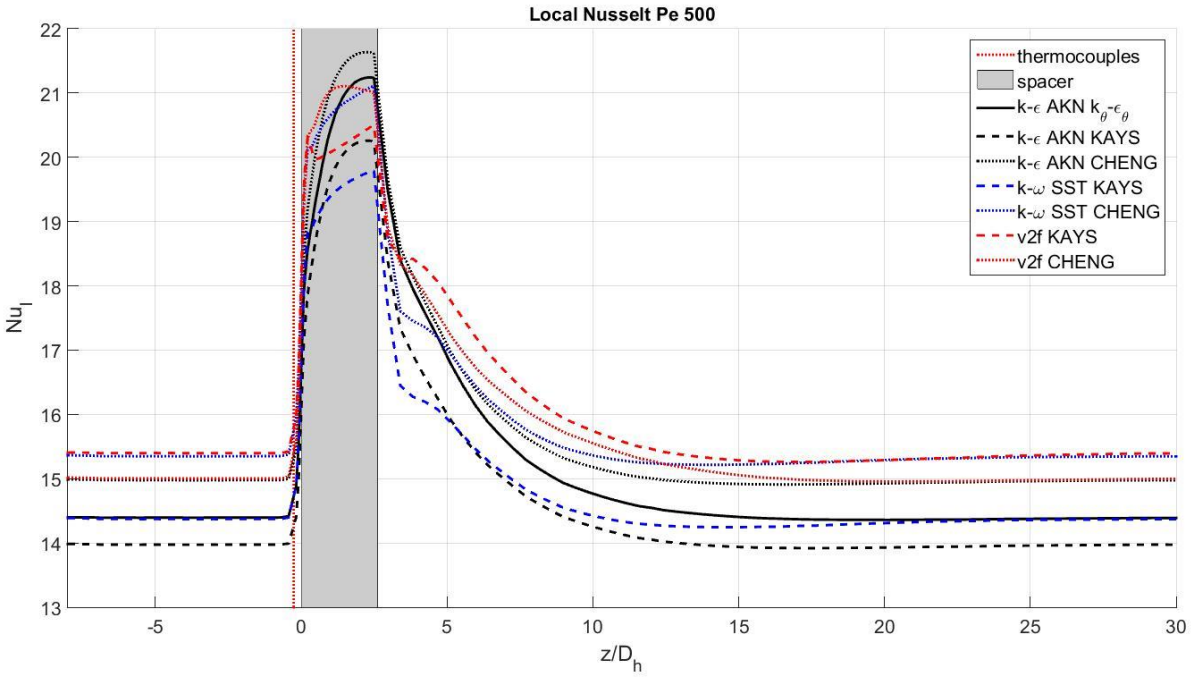

Fig. 5.32 Local Nusselt number Pe 500, infinite rod bundle with spacer.

Fig. 5.33 shows the Nusselt profiles on a Péclet number of 2500. It appears evident the difference on the green line intersection, all models are included on a wider Nusselt values range, compared with the two others Péclet numbers in Fig. 5.31 and Fig. 5.32. The greatest value of 26.6 is computed from the $k-\omega\, SST\ CHENG$ while the lowest of 22.1 is computed by the $k-\varepsilon\ AKN\ k_\theta-\varepsilon_\theta$. In this case the difference between each flow model is more emphasized due to the different approach to the turbulence visible in Fig. 5.21. Every model give different turbulent viscosity values which become more relevant with the mean Reynolds number increases.

The $k-\varepsilon\ AKN$ maintains its trend inside the spacer a monotonic Nusselt profile growth followed by a monotonic decrease downstream the spacer, in this case the CHENG correlation is the one which have the greatest Nusselt values in all the points of the profile, such as in the previous two Péclet cases. In this case the $k_\theta-\varepsilon_\theta$ computes the lowest values. Passing the $z/D_h = 20$ the KAYS and CHENG correlations reach a local minimum thereafter is noted a smooth Nusselt growth lower than 3% compared to the value at the green line intersection. The $k_\theta-\varepsilon_\theta$ haven't this damped oscillation trend downstream the spacer the profile decreases without any concavity change.

The $k-\omega\ SST$ plotted on the blue profile has a double maximum values inside the spacer, downstream the spacer it shows a relative maximum and minimum only with the KAYS correlation on a range across 5 hydraulic diameter thereafter an absolute minimum at $z/D_h = 15$ and a slight growth which is at the maximum the 4% the value on the green line. The CHENG case downstream

the spacer decreases up to the absolute minimum in $z/D_h = 15$ and increases slightly of about 4% the value on the green line intersection.

The $v2f$ has a double maximum value inside the spacer for both the correlation used and downstream it and in the range across 5 and 8 hydraulic diameter a relative minimum and maximum value respectively. The absolute minimum value is on $z/D_h = 20$ than the Nusselt profile grows of about the 3% the value measure on the green line intersection.

Inside the spacer in every case analyzed the CHENG Nusselt values are greater than the KAYS one. In the rest of the domain is not always true.

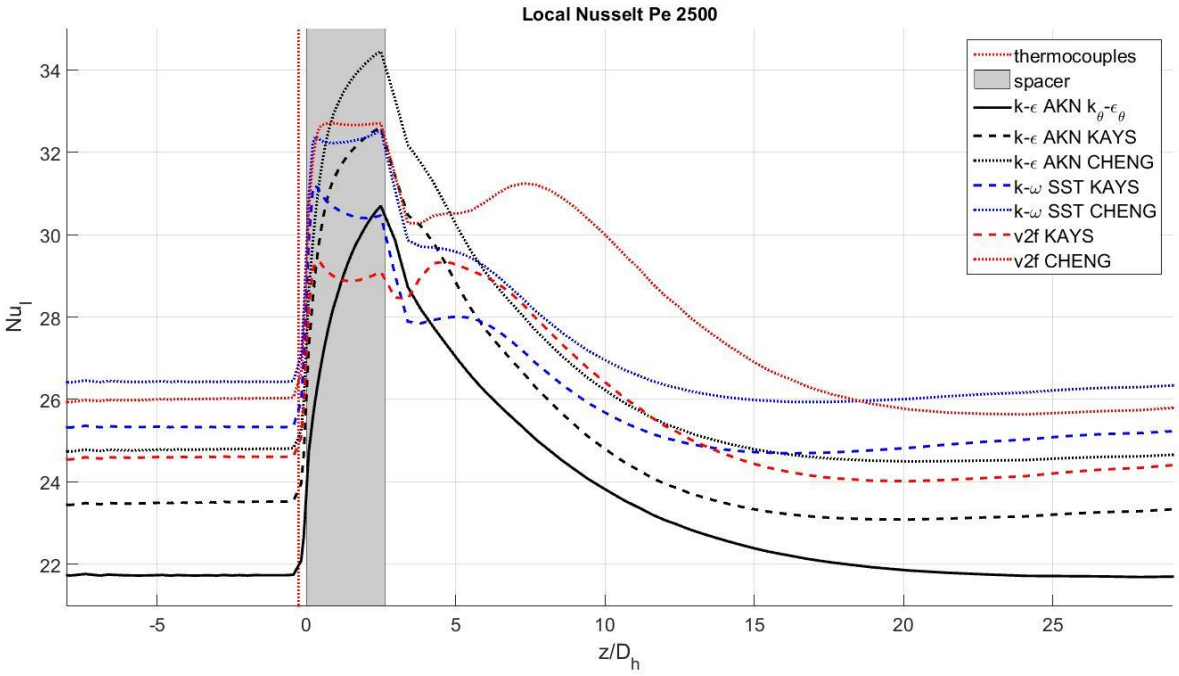

Fig. 5.33 Local Nusselt number Pe 2500, infinite rod bundle with spacer.

Fig. 5.34 is the Nusselt value from the green line interseciton varying the Peclét number.The red circles are the experimental data with their uncertainties hilighted by the red error bars from [1]. The filled square connected by the green line are the Mikityuk Nusselt correlation results for fully developed flow from Eq.(4.6). It should be rememberd that experimental Nusselt number has been computed using the warmest wall temperature instead the mean wall temperature value. It corresponds graphically to the c point in Fig. 5.1. From Fig. 5.29 the wall temperature distribution varies on about 7% from its mean value, Nusselt number computed using the maximum wall temperature are thus lower than the ones computed using the mean wall temperature. In Fig. 5.34 all Nusselt value are computed using Eq.(5.4) intesad of Eq.(4.1).

$$\alpha = \frac{q_w}{T_{max,w} - T_b} \tag{5.4}$$

It appears evident that experimental results are spread on a wide range and models don't match at all, thus the infinite rod bundle hypothesis is not so satysfing for the entire rod bundle Nusselt. Most of the models are in the experimental range and all of them give a result lower than

the mean experimental values. Following the lines whcich connect each result varing the Peclét number is clear to note that models don't respect a precise order. The ones which match better the results are $k-\omega\ SST\ CHENG$ and $v2f\ CHENG$, the worst ones are $k-\varepsilon\ AKN\ KAYS$ and $k-\varepsilon\ AKN\ k_\theta-\varepsilon_\theta$ which in the Pe=500 and Pe=2500 are out of the experimental range. The flow turbulence models coupled with the CHENG corelation give results which don't reverse their trends and are the most similar to the mean experimental values.

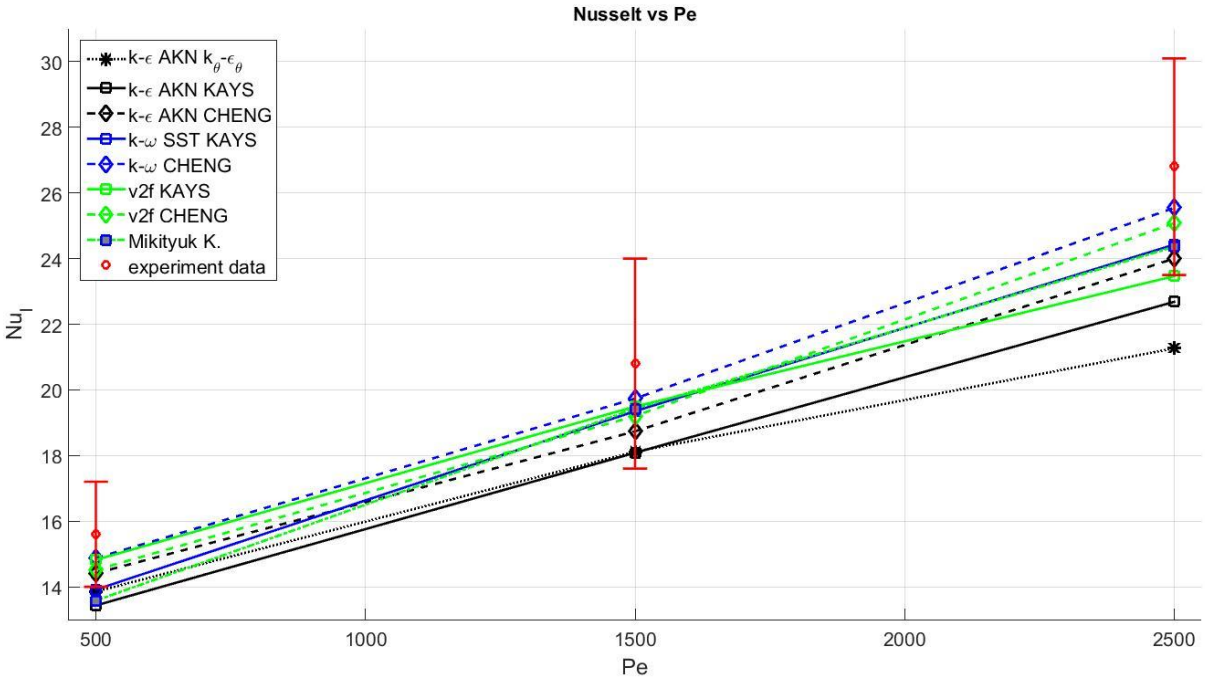

Fig. 5.34 Nusslet number value on the green line intersection varying the Peclét number.

5.2.1. GCI study

To ensure the consistency of results in Paragraph 5.2, has been performed an analysis based on the Richardson extrapolation that quantify the results validity.

The main computational errors source is the discretization. In steady-state problems, using double precision with strong convergence criteria, and when the code is free from programming errors and bugs, the remaining error is caused by the geometric discretization and the numerical discretization which is the numerical scheme. In order to quantify these errors, two different parameters are adopted: h, which is representative of the mesh spacing in Eq.(5.5), N is the entire cells amount and ΔV_i is the sigle cell volume. The other representative parameter is p in Eq.(5.9)(5.9), which stands for the order of the numerical scheme accuracy. The h-refinement treatment is commonly used to reduce the grid discretization errors in finite volumes techniques (the numerical scheme is fixed and the mesh is refined). In these studies the Richardson extrapolation can be adopted as a formally upper order extrapolated solution estimator and as an error estimator.

$$h = \left[\frac{1}{N}\sum_{i=1}^{N}\Delta V_i\right]^{1/3} \tag{5.5}$$

Taking a domain point $\boldsymbol{x}$, according to the Richardson extrapolation theory, when the solution of two or more simulations which is solved on a h-refinement criteria it is in the asymptotic range, the extrapolated value with an higher solution accuracy order can be found within Eq.(5.6), and its relative error is in Eq.(5.8), while the approximate relative error belonging to the fine solution grid is in Eq.(5.7) .

Thus, with three problem solutions ($\phi_1(x)$, $\phi_2(x)$, and $\phi_3(x)$) obtained performing an h-refinement treatment on the grids $h_1 = h_2/r_{21}$, (fine grid) $h_2 = h_3/r_{32}$, (middle grid) and h_3 (coarse grid), these equations take form:

$$\phi_{ext}^{21} = \frac{r_{21}^{p}\phi_1 - \phi_2}{r_{21}^{p} - 1} \tag{5.6}$$

$$e_a^{21} = \left|\frac{\phi_1 - \phi_2}{\phi_1}\right| \tag{5.7}$$

$$e_{ext}^{21} = \left|\frac{\phi_{ext}^{12} - \phi_1}{\phi_{ext}^{12}}\right| \tag{5.8}$$

Where the accuracy order p in Eq.(5.9) is assumed to be dependent on the position $\boldsymbol{x}$, and r is the refinement ratio. $\varepsilon_{21} = \phi_2(x) - \phi_1(x)$, and $\varepsilon_{32} = \phi_3(x) - \phi_2(x)$

$$p(\boldsymbol{x}) = \frac{1}{\ln r_{21}}\left|ln\left|\frac{\varepsilon_{32}}{\varepsilon_{21}}\right| + q(p)\right| \tag{5.9}$$

$$q(p) = ln\left(\frac{r_{21}^{p} - s}{r_{32}^{p} - s}\right) \tag{5.10}$$

$$s = 1 * sign\left(\frac{\varepsilon_{32}}{\varepsilon_{21}}\right) \tag{5.11}$$

The equations in (5.9), (5.10), (5.11) can be solved using a fixed point iteration, with the initial guess equal to the first term.

The accuracy order p with this particular formulation is meaningfully in case of monotonic convergence and in case of oscillatory convergence. With this formulation, can be calculated a formally upper-order extrapolated valueϕ_{ext}^{21} from Eq.(5.8) only in case of monotonic convergence. However, the use of the extrapolated value $\phi_{ext}(\boldsymbol{x})$, is generally not recommended because of its calculation not always apply in practical problems. On the other hand, the estimator of the relative

approximate error Eq.(5.7), is a good parameter in order to give credibility to the numerical solution. Roache [27] includes a safety factor $F_s$into this estimator and defines the Grid Convergence Index (GCI). At a given point **x** of the computational domain, the GCI corresponding to the fine grid solution $\phi_1(\boldsymbol{x})$takes form in Eq.(5.12), with this formulation, it includes also the case of oscillatory convergence [28].

$$GCI_{fine}^{21} = \frac{F_s * e_a^{21}}{r_{21}^p - 1} \tag{5.12}$$

In a two-grid convergence study where $p(\boldsymbol{x})$ must be assumed according to the formal accuracy order, is recommended a $F_s = 3$ value. Using three or more grids, such as are presented in this work, and where $p(\boldsymbol{x})$can be estimate with Eq.(5.9) a value of $F_s = 1.25$ appears to be adequately conservative [29].

Numerical problems can arise when analyzing $\phi(\boldsymbol{x})$ values close to 0 or node with both solutions changes approaching to 0. It is useful to classify the calculation nodes into three groups according to the following conditions:

$$Richardson\ node\text{: } [\phi_2^*(\boldsymbol{x}) - \phi_3^*(\boldsymbol{x})][\phi_1^*(\boldsymbol{x}) - \phi_2^*(\boldsymbol{x})] > C_0 \tag{5.13}$$

$$Converged\ node\text{: } [\phi_2^*(\boldsymbol{x}) - \phi_3^*(\boldsymbol{x})][\phi_1^*(\boldsymbol{x}) - \phi_2^*(\boldsymbol{x})] < C_0 \tag{5.14}$$

$$Oscillatory\ node\text{: } [\phi_2^*(\boldsymbol{x}) - \phi_3^*(\boldsymbol{x})][\phi_1^*(\boldsymbol{x}) - \phi_2^*(\boldsymbol{x})] < -C_0 \tag{5.15}$$

Where the upper index * indicates the that the solutions have been normalized using the maximum absolute $\phi(\boldsymbol{x})$, and C_0 is a positive coefficient approaching 0 ($C_0 = 10^{-30}$, in this work where all the computations have been performed using double precision real numbers).

The formal or theoretical accuracy order depends on the accuracy of the numerical schemes used in the inner and boundary nodes for both the diffusive and convective terms. In some cases such as when the numerical scheme is fully first order (upwind differential scheme) or second order (central difference), the accuracy of these is formally known. Thus, it is expected an overall order of accuracy p bounded by the minimum and maximum theoretical values for the present numerical scheme $p_{min} = 1$ and $p_{max} = 2$, from [28].

Analysis in this work has been performed using the grids with the elements number reported in Table 5.2, the grid volume to calculate the characteristic grid spacing in Eq.(5.5) can be derived from the mesh set up in Chapter 4. The GCI algorithm has been implemented in Matlab R2015a code the script used is in Appendix C. It is made to calculate the error bars with the GCI index in the Nusselt profiles, it calculate the percentage of Richardson, Oscillatory and Converged nodes, the minimum, maximum and average accuracy order p from. It display also the minimum maximum and average GCI index in each case.

Table 5.2 grids elements used in this thesis

	Grid 1	Grid 2	Grid 3
Pe = 500	1556800	297010	70497
Pe = 1500	1556800	297010	70497
Pe = 2500	7346680	2135835	282500

Analysis has been performed on every case varying the model and the Peclét number from a total of 21 cases here follow the most representative and a table which recapitulates the results in the measurement plane with the uncertainties.

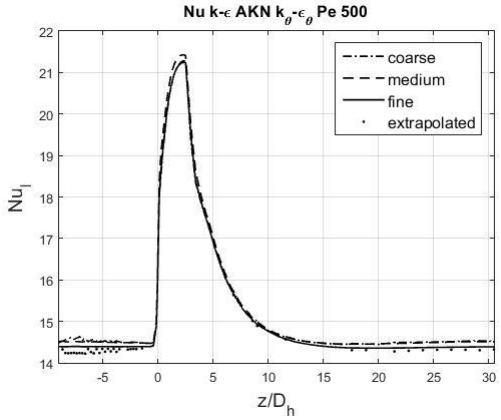

Fig. 5.35 Nusselt k-epsilon AKN, k theta epsilon theta Pe=500.

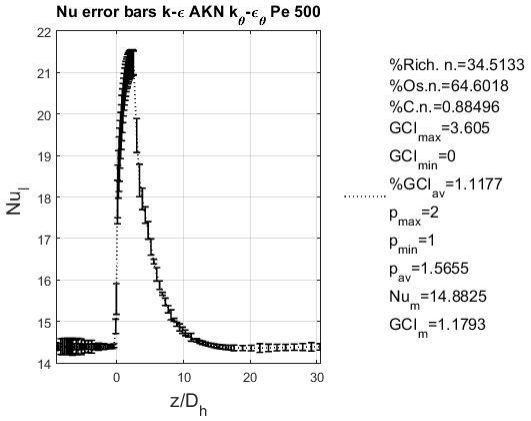

Fig. 5.36 Nusselt with GCI bars k-epsilon AKN, k theta epsilon theta Pe=500.

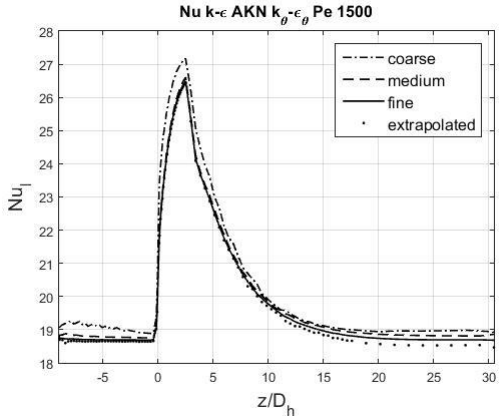

Fig. 5.37 Nusselt k-epsilon AKN, k theta epsilon theta Pe=1500.

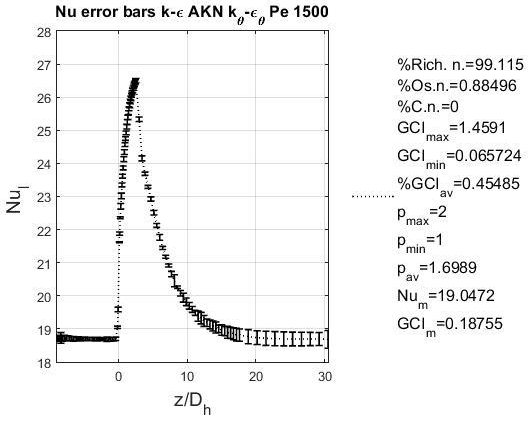

Fig. 5.38 Nusselt with GCI bars k-epsilon AKN, k theta epsilon theta Pe=1500.

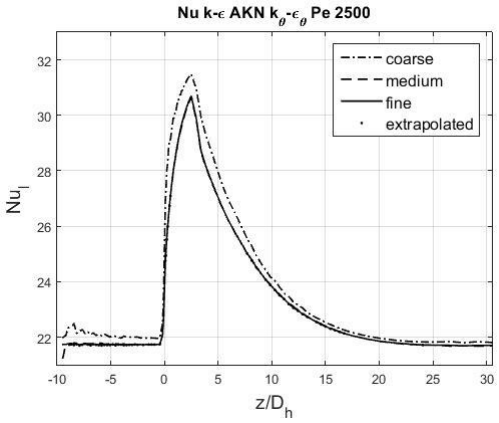

Fig. 5.39 Nusselt k-epsilon AKN, k theta epsilon theta Pe=2500.

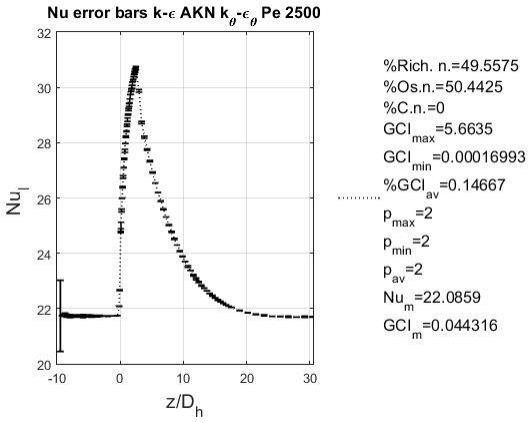

Fig. 5.40 Nusselt with GCI bars k-epsilon AKN, k theta epsilon theta Pe=2500.

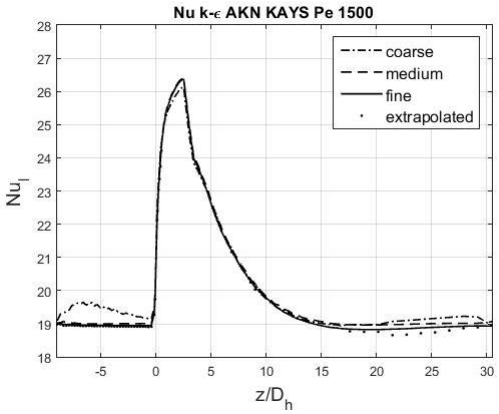

Fig. 5.41 Nusselt k epsilon AKN KAYS Pe=1500.

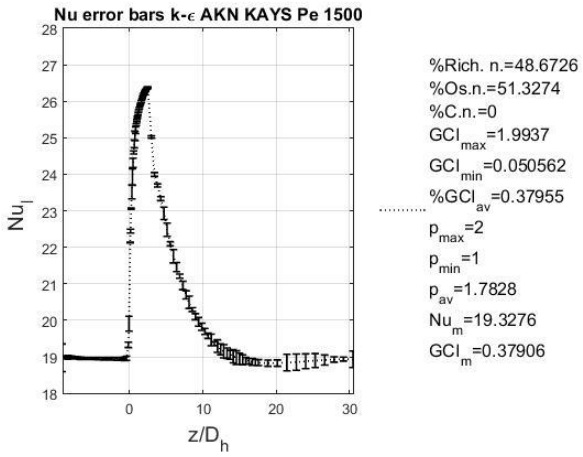

Fig. 5.42 Nusselt with GCI bars k epsilon AKN KAYS Pe=1500.

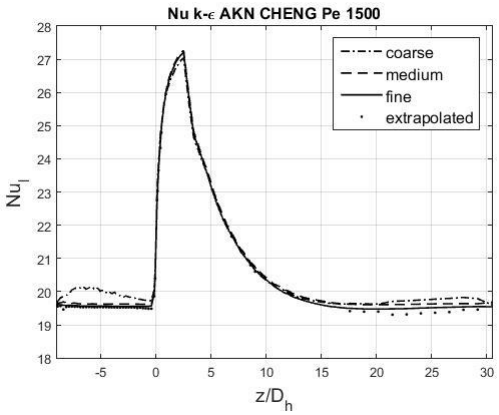

Fig. 5.43 Nusselt k epsilon AKN CHENG Pe=1500.

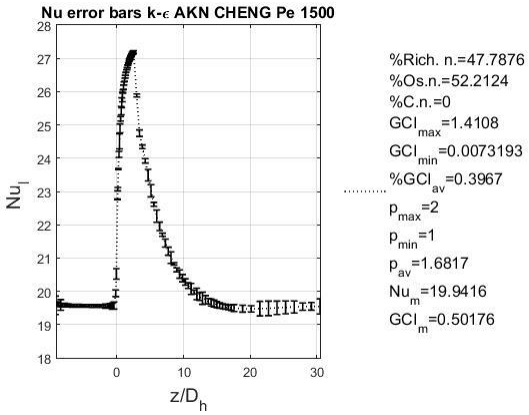

Fig. 5.44 Nusselt with GCI bars k epsilon AKN CHENG Pe=1500.

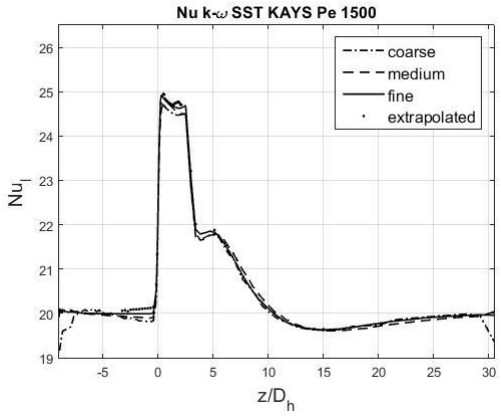

Fig. 5.45 Nusselt k omega AKN KAYS Pe=1500.

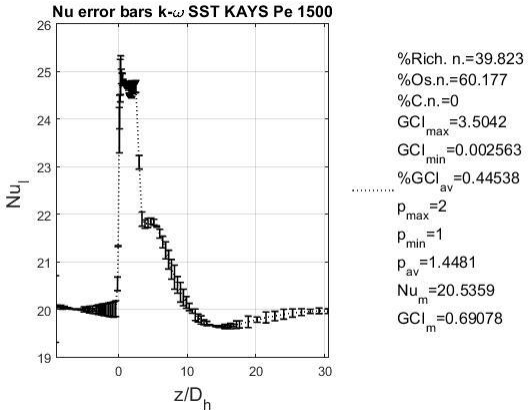

Fig. 5.46 Nusselt with GCI bars k omega AKN KAYS Pe=1500.

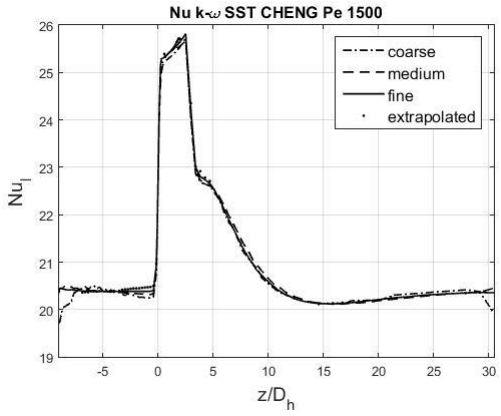

Fig. 5.47 Nusselt k omega AKN CHENG Pe=1500.

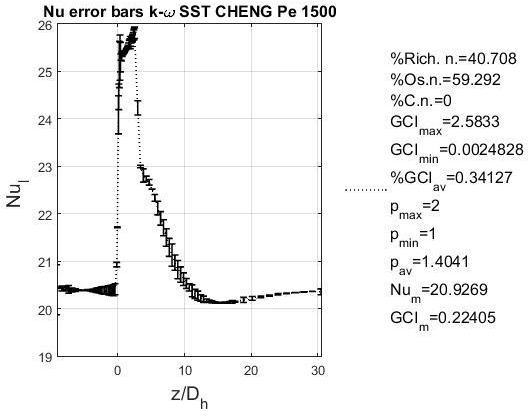

Fig. 5.48 Nusselt with GCI bars k omega AKN CHENG Pe=1500.

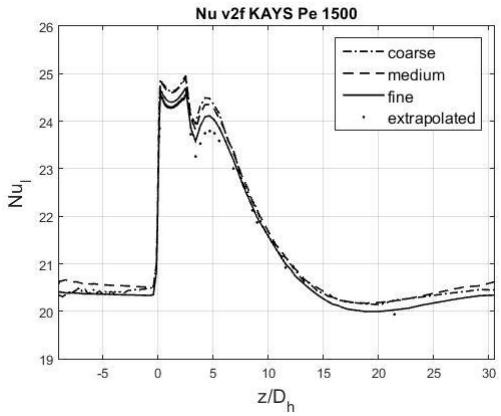

Fig. 5.49 Nusselt v2f KAYS Pe=1500.

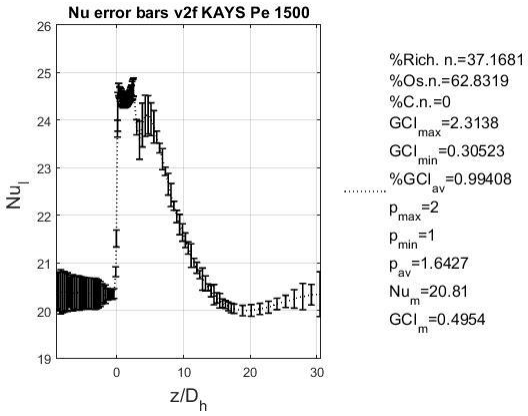

Fig. 5.50 Nusselt with GCI bars v2f KAYS Pe=1500.

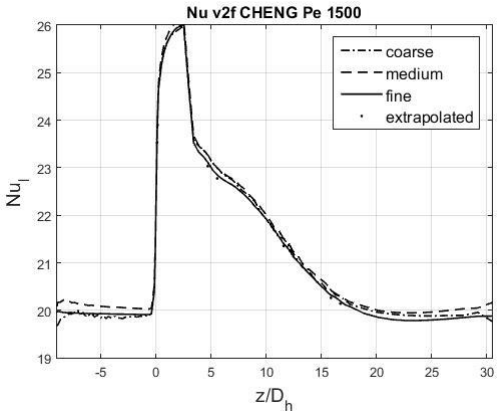

Fig. 5.51 Nusselt v2f CHENG Pe=1500.

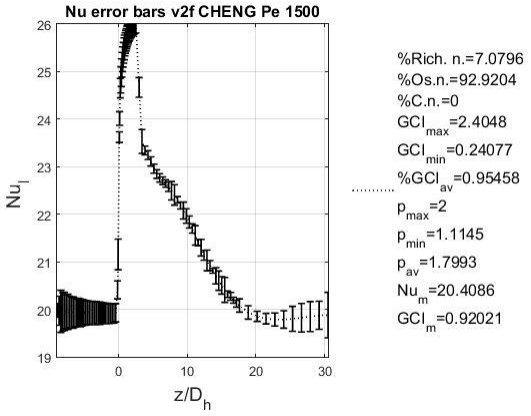

Fig. 5.52 Nusselt with GCI bars v2f CHENG Pe=1500.

Every case has two figures showing on the left side the three grids solutions and the extrapolated points because in this analysis the oscillatory nodes number is a great amount. The extrapolated curve is not defined on these points, thus oscillatory points don't have an extrapolated value. The right side figure is the fine grid plot with the error bars displaying the GCI value for each plane it plots and the relevant information on the case from the GCI study. Reducing the grid nodes number with an equal constant parameter h from Eq.(5.5) in every direction. The coarse grid results in some case don't follow the trend of the other two grids specially in the fluid zone upstream the spacer, this make a relevant part of the nodes to be classifies oscillatory nodes from Eq.(5.15).

The first consideration is on the $k-\varepsilon\ AKN\ k_\theta-\varepsilon_\theta$ reliability it is shown in Fig. 5.36, Fig. 5.38 and Fig. 5.40. The maximum GCI value is 5.66% on the greatest Peclét number because of the first cells in the inlet domain the medium grid discretization caused a non-homogenous profiles. The plots show a small GCI error especially in the measurement plane highlighted on the legends with the letter m in the subscript. Inside the spacer the error grows till reach its maximum value on the Nusselt pick. Downstream the spacer the GCI value grows slowly moving away from the spacer, the maximum GCI value is 5%, on the first node in the inlet section of the Pe= 2500 case. The maximum average GCI is 1.14% in the Pe=2500 case.

The $k-\varepsilon\ AKN\ KAYS$ and the $k-\varepsilon\ AKN\ CHENG$ in Fig. 5.42 and Fig. 5.44 have respectively an average GCI value of 0.38% and 0.4%, with a maximum value of 2% and 1.4 respectively. The widest error bars are downstream the spacer in the decreasing trend after the Nusselt maximum value inside the spacer and at the grid outlet section. In that grid zone the mesh resolution on the flow direction is coarser compared to the one close to the inlet and near the spacer zone because the temperature field is undisturbed.

The $k-\omega\ SST\ KAYS$ and the $k-\omega\ SST\ CHENG$ are in Fig. 5.46 and Fig. 5.48 respectively, they have an average GCI of 0.45% and 0.34% with a maximum value of 3.5% and 2.58%. These value are computed on the ascendant Nusselt profile zone close to the spacer inlet. The Nusslet growth is much more quick compared to the ones computed with the $k-\varepsilon\ AKN$ on the KAYS and CHENG cases. The coarse grid visible in Fig. 5.45 and Fig. 5.47 respectively shows a good trend as the medium and fine grid but underestimate their values close to the inlet and outlet section regions.

The worst converged cases are the ones computed using the $v2f$ model the medium grid has an oscillatory convergence. The Richardson nodes are 7%. The $CHENG$ case has an average GCI value of 0.95% and a maximum value of 2.4%. The widest Nusselt range error bars are at the inlet section and the outlet. The case computed using $KAYS$ model shows a similar error bars trend, the Richardson nodes are the 37%, the maximum and average GCI values are respectively 2.4% and 0.95%, the medium mesh convergence in both cases give worse result compared to the fine and coarse grid which have an almost overlapped profiles.

Table 5.3 is the Nusselt value calculated on the measurement plane upstream the spacer with their uncertainty range for all the simulated cases. The Nusselt number is computed with the average wall temperature in Eq.(4.1). The greatest result validity range is one magnitude order lower than the ones in the experiment. It shows that a cell number increase don't change the final simulated result. Thus the central rod of the bundle underestimates the mean Nusselt value from the rod bundle tested in the experiment.

Table 5.3 Nusselt number and their uncertainties in the measurement plane, from the mesh in Chapter(4.2.1)

	$Pe = 500$	$Pe = 1500$	$Pe = 2500$
$k-\varepsilon$ AKN $k_\theta - \varepsilon_\theta$	14.88 ± 0.17	19.05 ± 0.036	22.09 ± 0.0098
$k-\varepsilon$ AKN Kays	14.4 ± 0.04	19.32 ± 0.071	23.95 ± 0.045
$k-\varepsilon$ AKN Cheng	15.4 ± 0.05	19.94 ± 0.1	25.24 ± 0.04
$k-\omega\ SST$ Kays	14.89 ± 0.006	20.53 ± 0.014	25.95 ± 0.17
$k-\omega\ SST$ Cheng	15.93 ± 0.008	20.93 ± 0.047	27.07 ± 0.089
$k-\varepsilon\ v2f$ Kays	15.98 ± 0.11	20.81 ± 0.104	25.08 ± 0.067
$k-\varepsilon\ v2f$ Cheng	15.58 ± 0.087	20.40 ± 0.188	$26.62 \pm .053$

5.3. Complete mesh results

The analysis performed in Paragraph 5.2.1 shows the best compromise between the grid cells density and the results quality performing a simulation on the infinite rod bundle with spacer. Taking the case with a Pe=1500 as a reference the GCI analysis shows that the medium grid gives acceptable results with a small deviation compared to the fine one. Thus has been used the domain discretization on the medium grid to achieve a grid cells density similar in the complete mesh.

The mesh descripted in Paragraph 4.2.1 is 1/12 of a single rod while this one includes 3 complete rod and 1/6 of a single rod, the cell number should be at least: 297010 which is the cell number belonging to the mesh in Fig. 4.9, taking the value from the Table 5.2, and multiplying it for $3 * 1/6$, it comes out a cells amount of 10^6. Than it remains to mesh the two triangular channel and the external wall. In Fig. 5.53 are visible only the spacer walls and the external wall. The rods are plotted only inside the spacer. The mesh is showed on a plane upstream the spacer and on a plane inside the spacer. The yellow narrow and wired surface is frontal spacer wall, which is normal to the main flow direction.

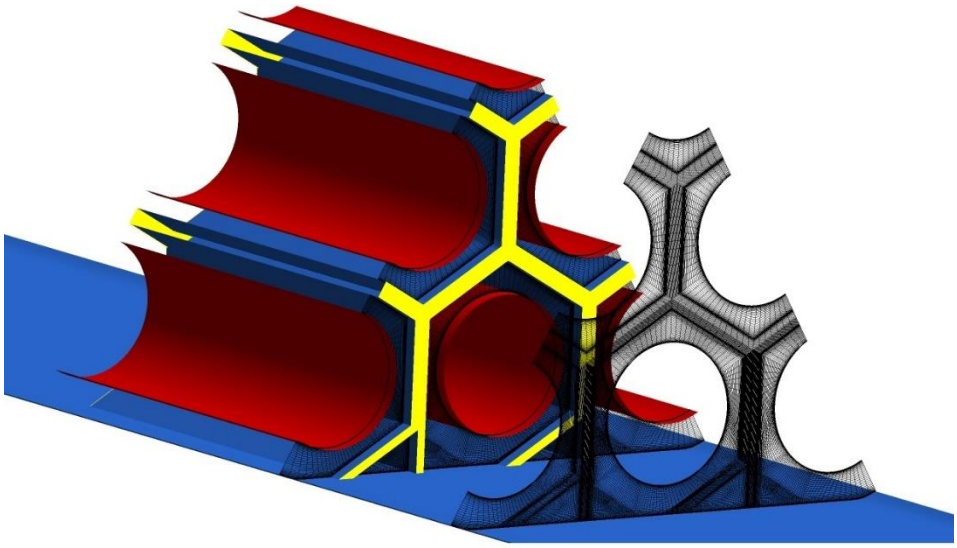

Fig. 5.53 Spacer grid, rods are visible only inside the spacer for displaying purpose, the mesh is visible on a plane upstream and inside the spacer.

The computational power available allows to use Fluent code in parallel up to $7 * 10^6$ cells, this value has been found after several attempts. Thus the grid has been built using all the $7 * 10^6$ cells, to have the best results. Simulations in this case are performed using the $k - \varepsilon\ AKN$ and the $k - \omega\ SST$, because the v2f model looking the GCI analysis in Paragraph 5.2.1 had the worst convergence. The $k - \varepsilon - k_\theta - \varepsilon_\theta$ using this mesh diverged in all the attempts performed. All the simulations are performed using a main Péclet number set to 1500.

The Fluent is set up using the discretization scheme to Second Order for the pressure, the momentum and the energy equations, the Least Square Cell Based for the continuity equation, the

turbulent models are all set to the First Order Upwind. Setting the turbulence equations to the Second Order Upwind the simulation diverges.

The under-relaxation-factors are set up to a lower values compared to the default ones. The under relaxation factors used in these simulations are available in Table 5.4.

Table 5.4 Under relaxation factors for the mesh descripted in Paragraph 4.2.2.

	$k-\varepsilon\ AKN$	$k-\omega\ SST$	Default values
Pressure	0.15	0.2	0.3
Momentum	0.4	0.5	0.7
Turbulent kinetic energy	0.3	0.6	0.8
Specific dissipation rate	0.3	0.6	0.8
Turbulent viscosity	0.7	0.8	1
Energy	1	1	1

It is visible from Table 5.4 that the under-relaxation-factors are set up to a lower values on the $k-\varepsilon\ AKN$ case because leaving them to the default ones the turbulence model doesn't converge. The turbulent viscosity needs to be under-relaxed too, to avoid the fluent bound in some critical cells. The $k-\omega\ SST$ is a more stable turbulence model but needs to be under-relaxed from the default values to reach the converge.

Both models reached the convergence with flat residuals profiles available in Table 5.5. These values are still great values compared to the previous case on the infinite rod bundle with spacer.

Table 5.5 Complete mesh residuals.

	$k-\varepsilon\ AKN$	$k-\omega\ SST$
continuity	$1.2*10^{-3}$	$8.89*10^{-4}$
x-velocity	$1.13*10^{-5}$	$5.24*10^{-6}$
y-velocity	$1.12*10^{-5}$	$3.98*10^{-6}$
z-velocity	$1.5*10^{-5}$	$7.13*10^{-6}$
k	$2.12*10^{-4}$	$7.76*10^{-5}$
Specific dissipation rate	$4.8*10^{-4}$	$2.72*10^{-5}$

The analysis starts from the velocity contours for the $k-\varepsilon\ AKN$ and the $k-\omega\ SST$ are respectively in Fig. 5.54 and Fig. 5.56. The contours are plotted in a plane orthogonal to the main flow upstream the spacer at $z/D_h=-5$ in Fig. 4.7, the same plane position as the previous case. The contours are plotted with the cell center values thus is visible in some areas the cells discretization. The dimensional velocity values are divided with the bulk velocity value. The velocities contorus are similar but the maximum values is greater in the the $k-\varepsilon\ AKN$ case, it is the same in the infinite rod bundle with spacer, the $k-\varepsilon\ AKN$ model reaches a greater velocity pick values.

The turbulent viscosity ratio plots are in Fig. 5.55 and Fig. 5.57 respectively for $k-\varepsilon\ AKN$ and the $k-\omega\ SST$. On the upper zone the $k-\omega\ SST$ has a contour more symmetric to the rod bundle geometry and also greater values compared to the $k-\varepsilon\ AKN$. On the bottom part close to

the external wall region the contours have both their maxima values and they aren't symmetric probably due to the triangular spacer channels which are in the same positions moving along the z coordinate. The $k - \varepsilon\ AKN$ on its bottom zone have a maximum range of values higher on the right zone.

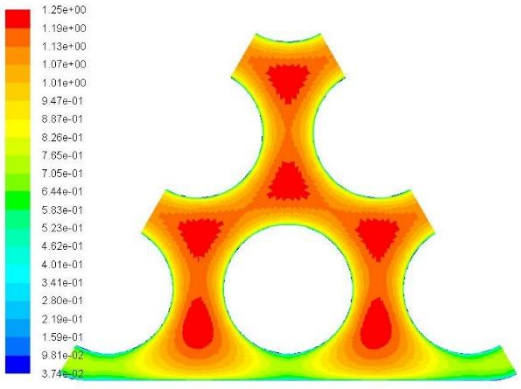

Fig. 5.54 Dimensionless velocity contour k-epsilon AKN, complete mesh.

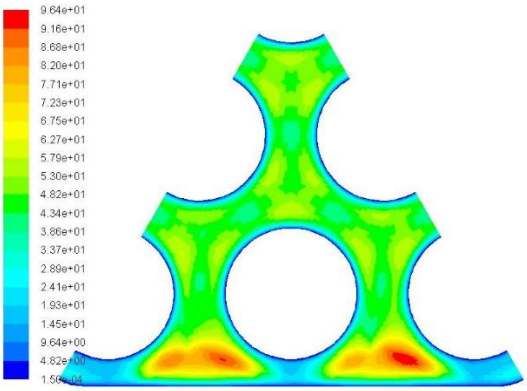

Fig. 5.55 Turbulent viscosity ratio k-epsilon AKN, complete mesh.

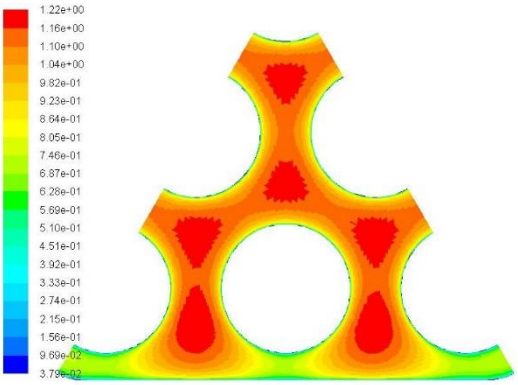

Fig. 5.56 Dimensionless velocity profile k-omega SST, complete mesh.

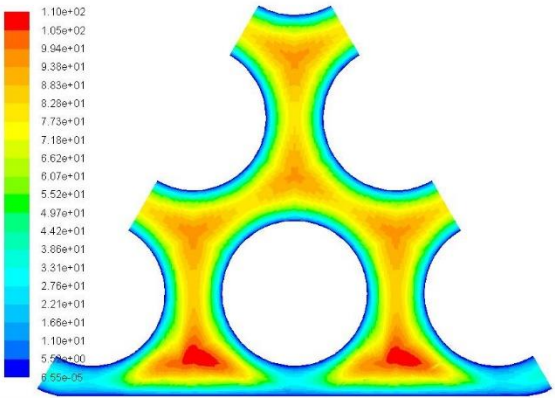

Fig. 5.57 Turbulent viscosity ratio k-omega SST Pe 1500, complete mesh.

Fig. 5.58 is the frontal rod bundle view with the red lines located to sample the thermodynamics and the kinematic quantities.

The sampling lines are placed in the same position in order to reproduce the contour of the infinite rod bundle with spacer analysis in Paragraph 5.2. The geometry used in the in the previous paragraph is thus repeated 5 times in order to sample the data from the central rod to the peripherals ones.

On the bottom zone lines ab4 and bc4 are symmetric to lines ab5 and bc5 respectively, in order to quantify the asymmetry visible in the contours. On the upper zone lines are all in different positions in order to quantify the changes from the central rod to the peripherals ones.

Lines ab1 and bc1 which belongs to the central rod of the bundle are supposed to give the closer results to the in finite rod bundle with spacer. On the following plots the variables values from the previous paragraph are reported on the legend using the word 'ref'.

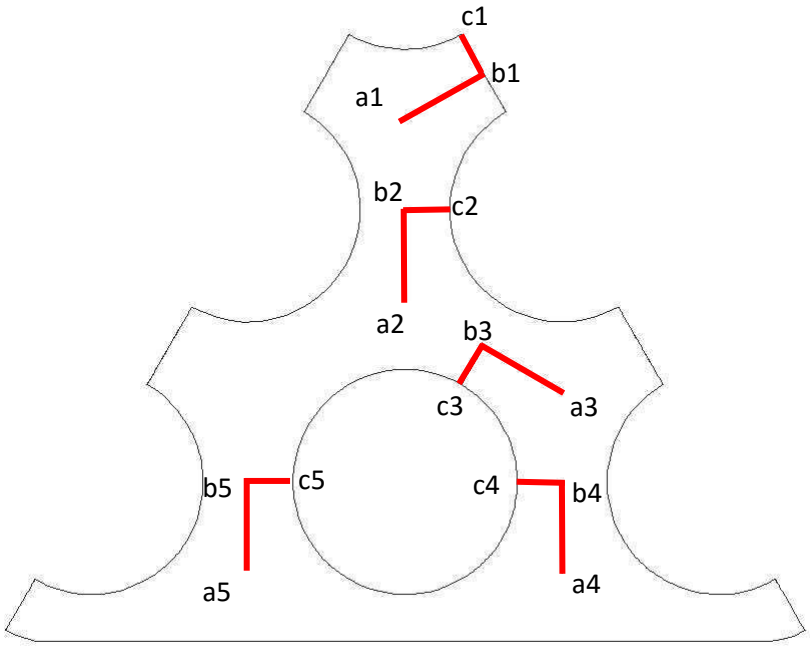

Fig. 5.58 Frontal rod bundle view with the red sampling lines.

The velocity profiles are plotted on the bc line, they are visible in Fig. 5.59 and Fig. 5.61. The lines bc1, bc2 and bc3 have an identical profile, the bc4 and bc5 lines have also an identical profile but it reaches greater values compared to the central rods profiles. Thus the velocity profile belonging to the first three rods from the upper zone can be considered independent from the external wall. Otherwise there would expected several profiles which converge to the central one.

The profiles plotted using small empty circles are the infinite rod bundle with spacer cases and they are the lowest ones in both cases.

Fig. 5.60 and Fig. 5.62 are the turbulent viscosity ratio profiles respectively for the $k-\varepsilon\ AKN$ and the $k-\omega\ SST$ sampled in the same lines. The general trend is similar to the velocity one, to greater velocity values correspond greater turbulent viscosity ratio values. The bc4 and bc5 lines trend are slightly different on both the turbulence models, confirming the contour asymmetry.

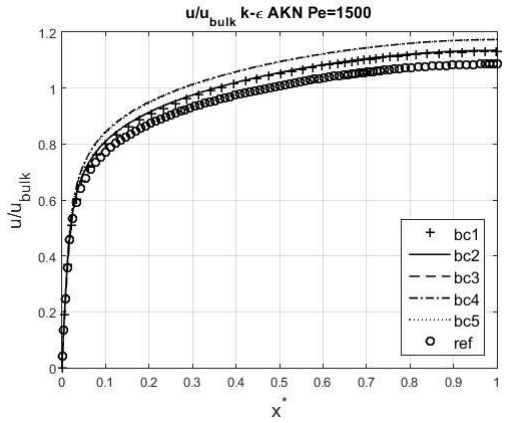

Fig. 5.59 Dimensionless velocity profiles, complete mesh k-epsilon AKN.

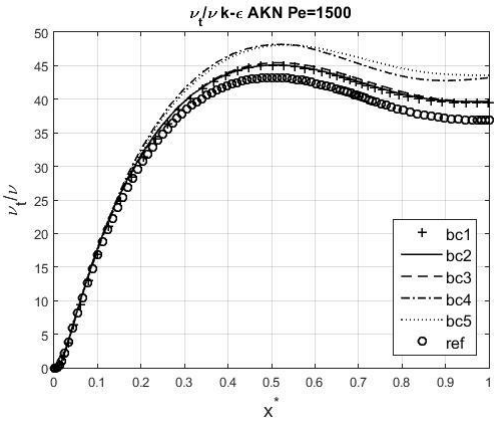

Fig. 5.60 Turbulent viscosity ratio profiles, complete mesh, k-epsilon AKN.

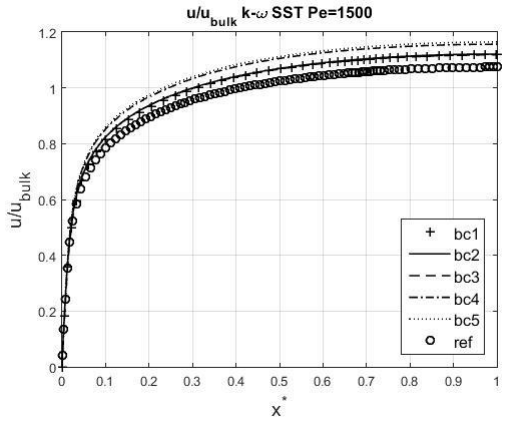

Fig. 5.61 Dimensionless velocity profiles, complete mesh k-omega SST.

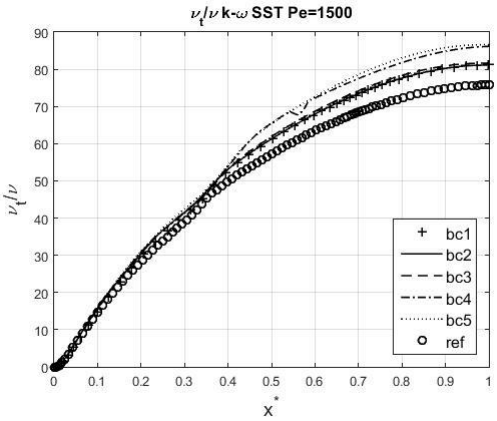

Fig. 5.62 Turbulent viscosity ratio profiles, complete mesh, k-omega SST.

The $k-\varepsilon\ AKN$ temperature contours are in Fig. 5.63 and Fig. 5.64 respectively using the turbulent Prandtl number correlation of CHENG and KAYS. The temperature contour is made non-dimensional using Eq.(5.15).

$$\theta^* = \frac{T - T_{a1}}{q\ D_h}\lambda \tag{5.16}$$

T_{a1} is the coldest point of the infinite rod bundle with spacer. To compare the infinite rod bundle with the central rod of the current case, the temperature on a_1 in Fig. 5.58 has been set to zero value.

The contours are similar, it is evident the asymmetry between the right bottom side and the left bottom side while the upper zone close to the central rod respects the geometry symmetry. The spacer grid is asymmetric on the bottom part such as is visible on Fig. 5.53. The coldest zone on the contour corresponds to the biggest flow area inside the spacer, thus the profile is clearly asymmetric even if the contour outside the spacer is symmetric. Thus the thermal field is not fully developed.

Fig. 5.65 and Fig. 5.66 are the non-dimensional temperature contour respectively for CHENG and KAYS using the $k-\omega\ SST$ flow turbulence model, considerations are dame to the $k-\varepsilon\ AKN$ but contours are on a lower temperature range values.

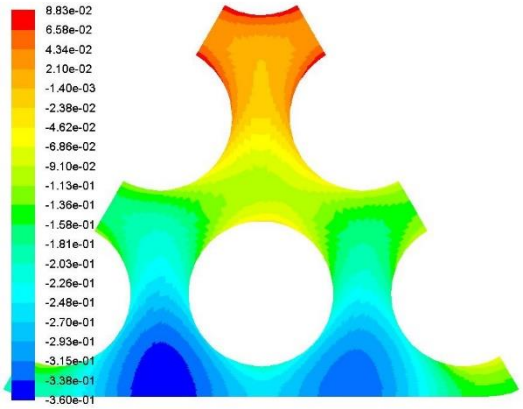

Fig. 5.63 Theta star contour, k-epsilon AKN CHENG, complete mesh.

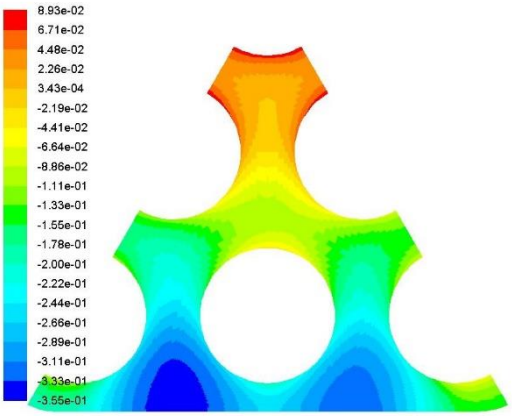

Fig. 5.64 Theta star contour, k-epsilon AKN KAYS, complete mesh.

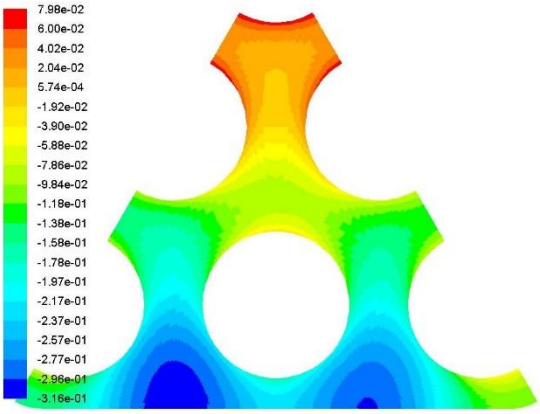

Fig. 5.65 Theta star contour k-omega SST CHENG, complete mesh.

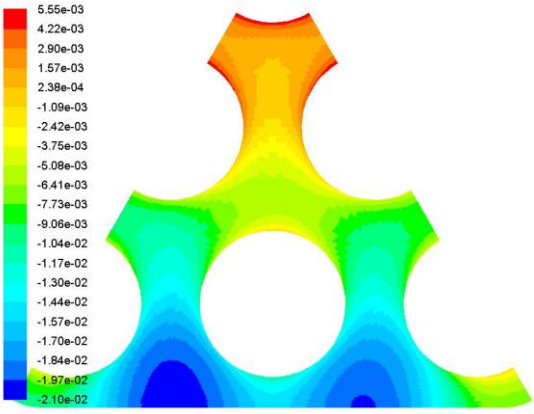

Fig. 5.66 Theta star contour k-omega SST KAYS, complete mesh.

The non-dimensional temperature profiles are plotted on the lines showed in Fig. 5.58. Temperature profiles are transformed to non-dimensional ones using Eq.(5.16), thus only the ab1 and bc1 profiles have positive values, the remaining profiles have negative temperature values.

In all the cases the on the line ab1 and bc1 the profile have the greatest temperature value the profile fit with the infinite rod bundle with spacer case. The wall temperature on $x^* = 1$ is approssimatively the 10% higher compared to the infinite rod bundle case.

Following the temperature profile from the warmest in a1, b1 and c1 and moving toward the external wall till arrive to the a4 b4 and c4 profile the curves gradient increases its magnitude. The abc1 has a flatter profile confronted with the abc4 and abc5.

The $k-\omega\ SST$ with CHENG and KAYS is plotted from Fig. 5.71, to Fig. 5.74 has its abc1 profile which fits better with the infinite rod bundle case compared to the $k-\varepsilon\ AKN$ visible from Fig. 5.67 to Fig. 5.70. The total temperature range is also lower and the abc4 profile is closer to the abc5 profile compared with the $k-\varepsilon\ AKN$ profiles.

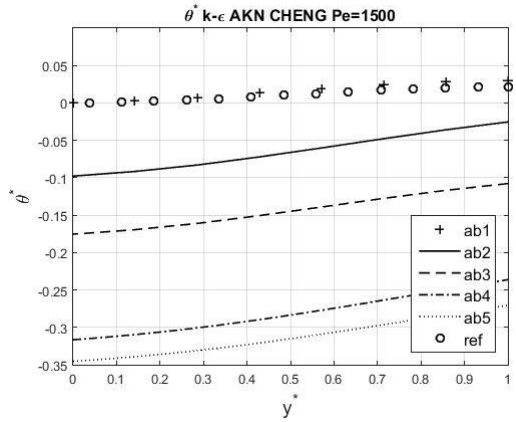

Fig. 5.67 Theta star k-epsilon AKN CHENG ab lines, complete mesh.

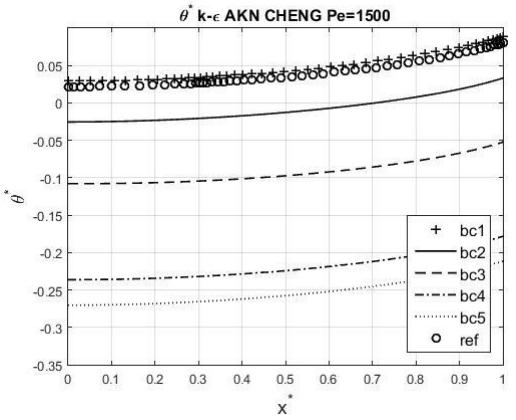

Fig. 5.68 Theta star k-epsilon AKN KAYS bc lines, complete mesh.

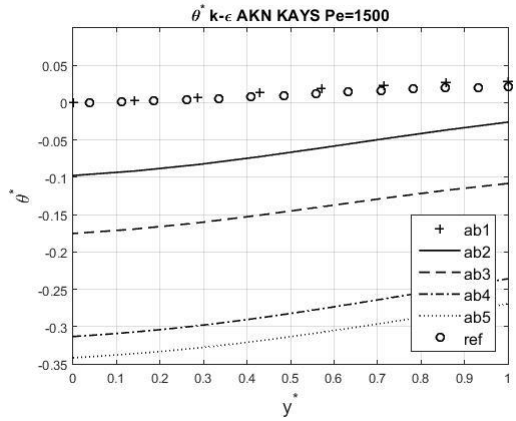

Fig. 5.69 Theta star k-epsilon AKN KAYS ab lines, complete mesh.

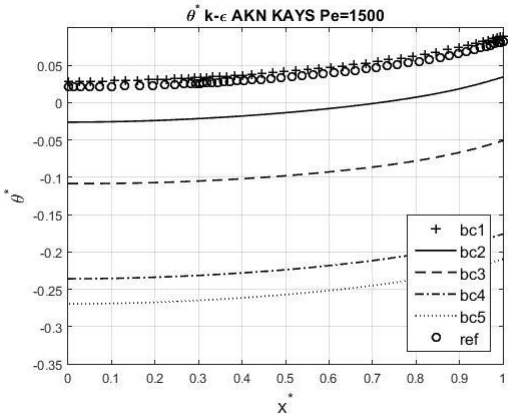

Fig. 5.70 Theta star k-epsilon AKN KAYS bc lines, complete mesh.

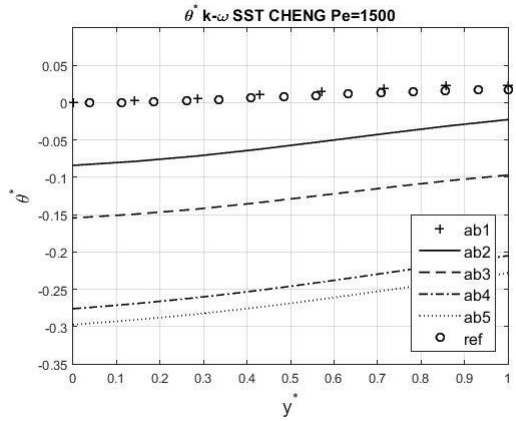

Fig. 5.71 Theta star k-omega SST CHENG ab lines, complete mesh.

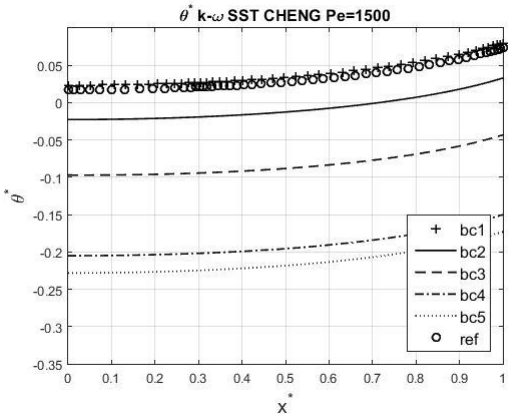

Fig. 5.72 Theta star k-omega SST CHENG bc lines, complete mesh.

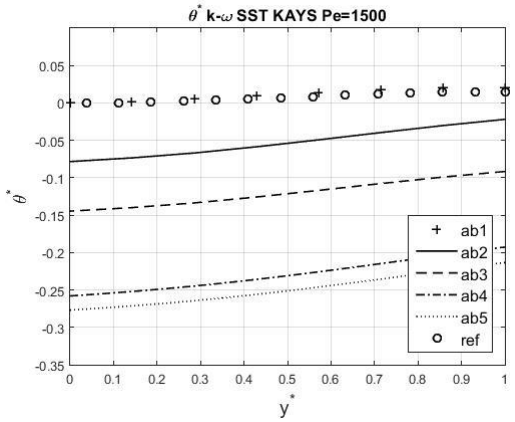

Fig. 5.73 Theta star k-omega SST KAYS ab lines, complete mesh.

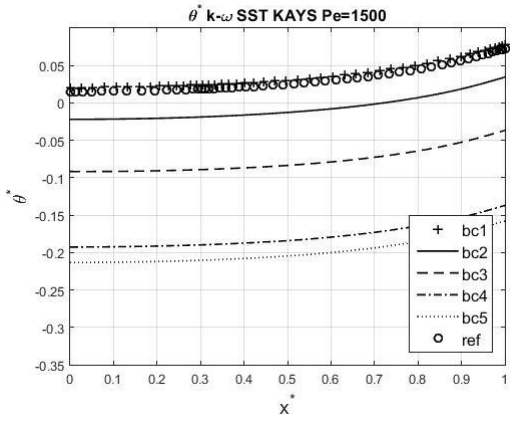

Fig. 5.74 Theta star k-omega SST KAYS bc lines, complete mesh.

Fig. 5.75 is the dimensionless average wall temperature moving along the flow main direction. Upstream the spacer the profile is univocal. Getting closer to the spacer the temperature profile grows and shows a maximum on the green line intersection, where are placed the thermocouples. Inside the spacer the profiles are different for each models and turbulent Prandtl correlations, downstream it there are two separate profiles grouped for the two flow turbulence models, KAYS and CHENG with the $k-\varepsilon\ AKN$ model are overlapped and the same for the $k-\omega\ SST$.

The difference with the infinite rod bundle with spacer in Fig. 5.30, crossing the spacer in this case the temperature profile decreases its magnitude locally. Upstream and downstream the profile is univocal. In the 19 rod bundle it has a further increase crossing the spacer and downstream the spacer there are two different profiles.

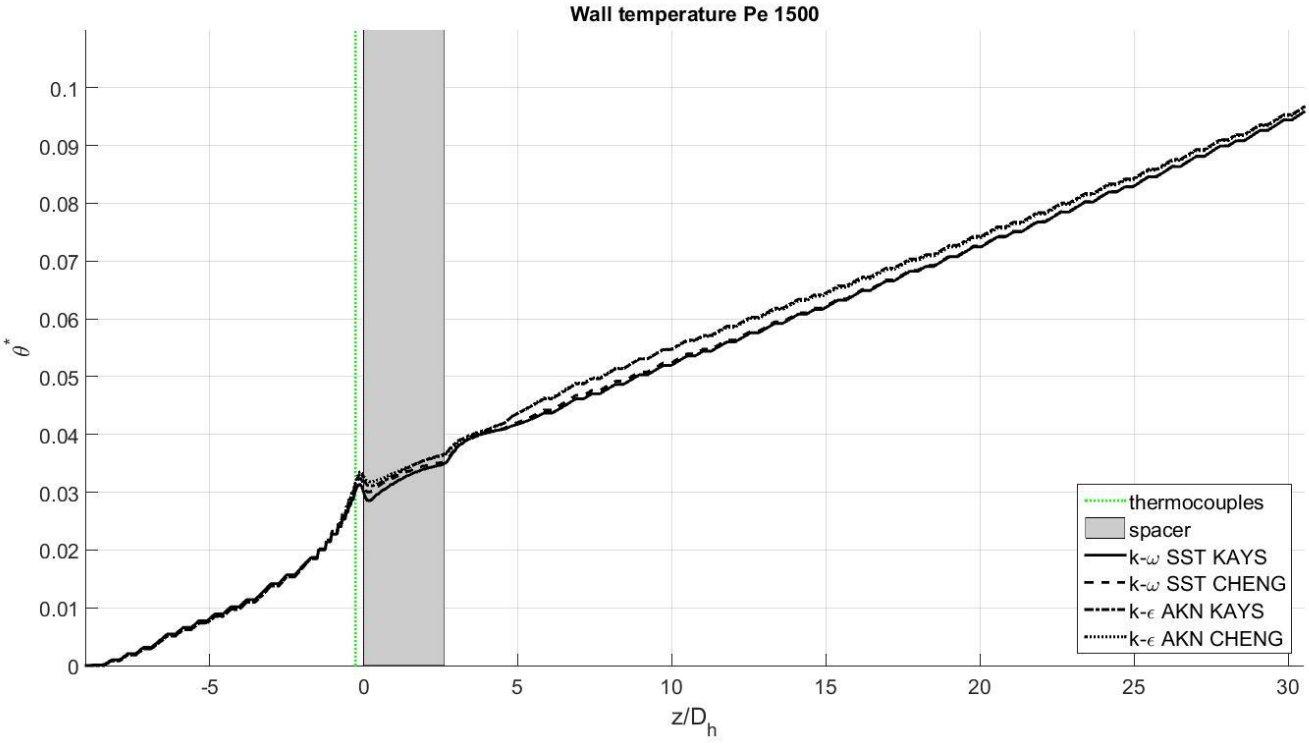

Fig. 5.75 Dimensionless wall temperature, complete mesh.

Fig. 5.76 is the local Nusselt number sampled along the main flow direction using Eq.(4.3). The first aspect to note is the general trend which is the opposite compared to the infinite rod bundle with spacer in Fig. 5.31 crossing the spacer in this case the Nusselt number decreases its magnitude and than increases again while on the infinite rod bundle, the spacer disturbance lead to a Nusselt profile increase followed by a decaying trend and stabilization on a undisturbed value.

In Fig. 5.76 can be note that every Nussel profiles are corrugated probably because of the coarse mesh discretization. The Nusselt plotted is an integral quantity, to an average wall temperature on the rod line for a determinate axial coordinate corresponds a plane in which is computed the bulk temperature. Taking three consecutive value for three consecutive coordinate the bulk temperature is different in the three different planes but the wall temperature is the same because is computed on the same cells. This is due to the low grid axial discretization. Taking the inner spacer zone in the grey area the profile is not corrugated because in that zone the grid resolution is fine to catch the flow changes.

From this figure is clear that the Nussel profile never became flat thus the thermal profile in this case is never fully developed.

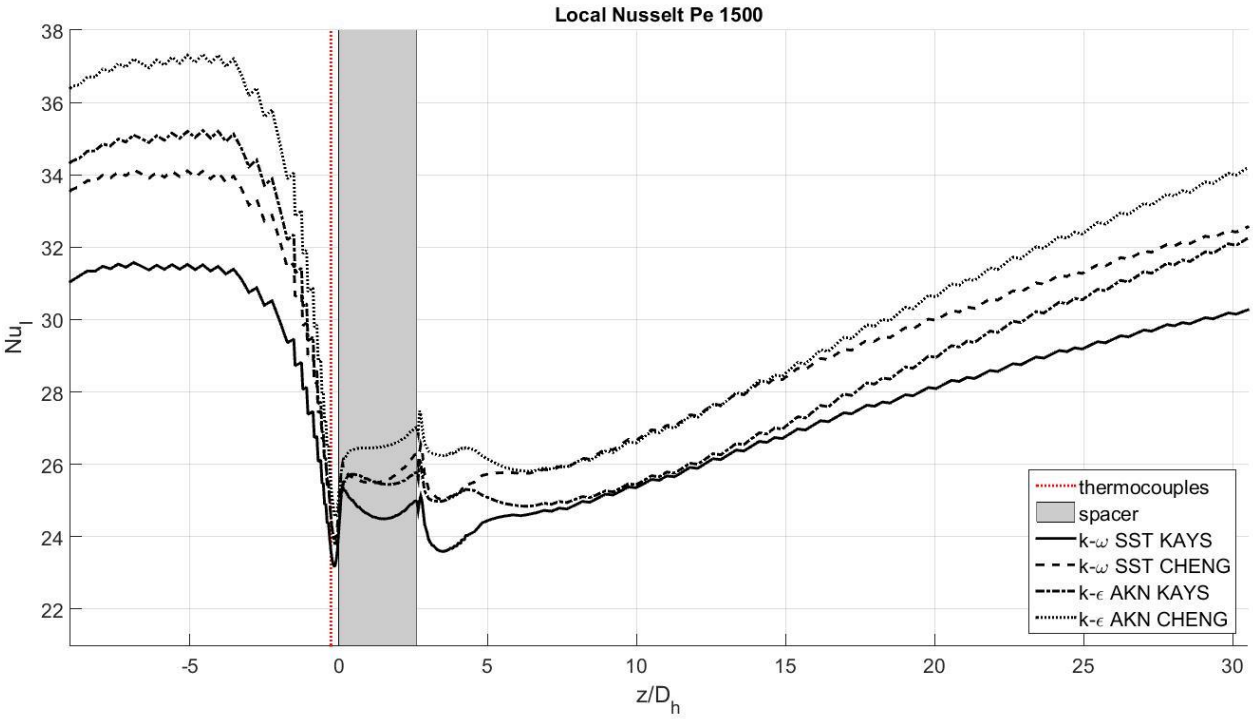

Fig. 5.76 Local Nusselt number, complete mesh.

To compare the computed cases with the experimental data it necessary to make dimensionless variables using the same forms. The Nusselt has been computed from the bulk temperature in the section highlighted by the green line and the wall temperature sampled by the thermocouples in the same plane. The wall temperature is sampled in the points highlight with the triangles in Fig. 5.77 (a) and reported in the computational domain in Fig. 5.77 (b) according to the

symmetry criteria. The same has been done with the red squares to sample the temperature at the central channel.

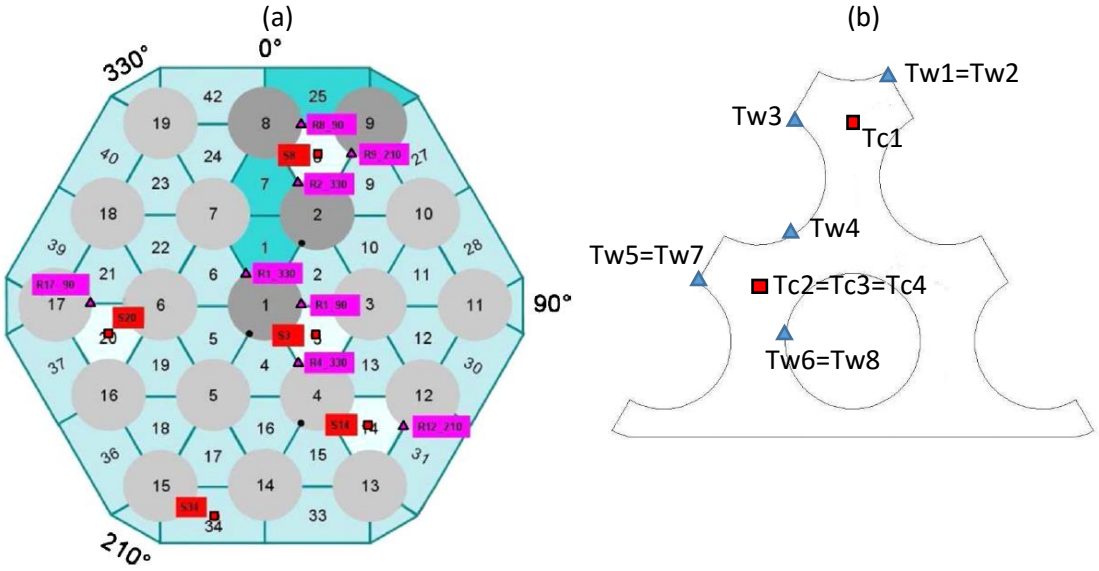

Fig. 5.77 Thermocouples scheme in (a) reported in the grid used in (b).

Thus the wall temperature in the Nusselt number in Eq.(4.3)has been computed performing an arithmetic mean of the Tw. Results are in Table 5.6.

The dimensionless temperature has been computed using Eq.(5.17) where T_b is the bulk temperature in the same plane, D_h the hydraulic diameter, q the wall heat flux and λ the laminar thermal conductivity.

$$\theta = \frac{T - T_b}{D_h\, q}\lambda \tag{5.17}$$

Results are in Table 5.6 with data belonging to the second and third spacers from the experiment. Results are different unfortunately there isn't the possibility to test the simulation reliability with a GCI study such as is performed on the previous case in Paragraph 5.2.

Table 5.6 Nusselt numbers and dimensionless temperature confronted with the experimental data, complete mesh.

	$k-\varepsilon AKN$ $CHENG$	$k-\varepsilon AKN$ $KAYS$	$k-\omega SST$ $CHENG$	$k-\omega SST$ $KAYS$	Experiment Sp 2	Experiment Sp 3
Nu	7.9568532	7.923413	8.650534	8.942569	20.3±2.6	19.8±4.4
$\theta_{w,max}$	0.2508588	0.250932	0.220154	0.208721	-0.54	-0.564
$\theta_{channel}$	0.0229147	0.02248	0.023288	0.021957	-0.162	-0.109

The mesh is still coarse specially on the z/D_h direction as is visible in the the Nusselt and wall temperature plots a further refinement up to $20 * 10^6$ cells should be tested to improve the results.

Chapter 6

6. Conclusions

The heat transfer in a 19-rod bundle with grid spacers operated with a liquid metal having a representative Prandtl number of 0.025 has been numerically analyzed.

First of all the operation of a rod bundle with grid spacer has been outlined in Section (2.1.2), in particular has been studied the spacer details and their discretization on the RANS approach in Section(4). Since the grid spacer represent a relevant perturbation on the velocity and in particular the temperature field, the applicability of Nusselt correlation developed for fully developed thermal field isn't aviable.

The analysis has been focused on the spacer geometry study, how it influences the thermal field and the liquid metals characteristic heat transfer. The Reynolds analogy which assumes a characteristic and constant turbulent Prandtl number close to unity is not valid, the characteristic liquid metals physical properties lead to peculiar heat transfer. A crucial point for the RANS analysis has been to follow a suitable approach of computing the heat transfer flux.

Different approaches has been analyzed in Section (3) and assessed, in particular a recently proposed $k_\theta - \varepsilon_\theta$ model which is specifically calibrated for liquid metal has been implemented and coupled to the solver (Fluent v.14). Besides the equations for the turbulent kinetic energy and its dissipation rate, have been solved, in order to locally calculate the turbulent thermal diffusivity.

Other approaches lead to use two semi empirical correlations to compute the turbulent thermal diffusivity the first developed from Cheng and Tak in Section (3.3.1) and the second developed from Kays in Section (3.3.2).

These correlations were coupled with several flow turbulence model already implemented in the Fluent code and descripted in Section (3.2). The correlations and the thermal turbulence model results are confronted in order to quantify the differences and find the best agreement with the experimental data champing performed at the KALLA laboratory at the KIT institute in Karlsruhe (Germany).

The $k_\theta - \varepsilon_\theta$ model and the correlations show very similar results in the infinite rod bundle case without grid spacer with fully developed velocity and temperature fields in Section (5.1), in this case has been used only the turbulence flow model $k - \varepsilon$ AKN.

The second case studied is the infinite rod bundle with grid spacer in Section (5.2), in this case has been tested the several flow models the results are inside the band of uncertainties computed from the experimental data. The $k_\theta - \varepsilon_\theta$ model has low a result trend compared to the other correlations. Considering the three Péclet number cases tested the greater Péclet which corresponds to 2500 the $k_\theta - \varepsilon_\theta$ give the lowest Nusselt number profile compared to the other case and the experimental data out from the uncertainties band. All simulation perfume in this case downstream the spacer show a residual perturbation lower than 5% on the measured value in the thermocouples plane, the thermal field can be considered fully developed taking in account that the Nusselt variation on the same case changing the models is greater than 5%.

The third case studied is the complete mesh of a spacer, the cell number amount has been bounded from the maximum computational power available. The grid discretization wasn't satisfying for the $k_\theta - \varepsilon_\theta$ model convergence, thus has been used the CHENG and KAYS correlations with the $k - \varepsilon$ AKN and $k - \omega\, SST$ flow turbulence models. The results don't match the experimental data, they show a not fully developed Nusselt profile, in the upstream measuring plane the values are influenced from the spacer presence, the Nusselt number downstream the spacer never became fully developed.

This work has been carried out in collaboration with the KALLA team of the Institute for Nuclear Energy Technology IKET at KIT, where the experiments were performed in the THEADES loop descripted in Section (2.1).

The spacer geometry has a great influence on the crossing spacer flow thus need to be simulated in detail to achieve reliable results. Future work could simulate the whole test section with the $k_\theta - \varepsilon_\theta$ in order to produce detailed results which are not available with the experimental tests due to a several complications on the data sampling.

Appendix A

User Defined Function to implement the $k_\theta - \varepsilon_\theta$ model from paragraph 3.3.3 into the Fluent code.

```
/*
 * UDF for the LRN model of Abe-Kondoh-Nagano according to the
following papers:
 * [1] Abe K., Kondoh T., Nagano Y. (1994) A new turbulence model for
predicting fluid flow and heat transfer in separating and reattaching
flows - I. Flow field calculations, Int. J. Heat Mass Transfer,
37(1), 139-151
 * [2] Abe K., Kondoh T., Nagano Y. (1995) A new turbulence model for
predicting fluid flow and heat transfer in separating and reattaching
flows - I. Thermal field calculations, Int. J. Heat Mass Transfer,
38(8), 1467-1481
 * [3] Manservisi S. Menghini F. (2014) A CFD four parameter heat
transfer turbulence model for engineering applications in HLM, In.
Jou. of Heat and Mass Transfer, 69, 312-326
 * [4] Manservisi S. Menghini F. (2014) Triangular rod bundle
simulations of a CFD k-e-kt-et heat transfer turbulence model for
heavy liquid metals, Nuclear engineering and Design 273 (2014) 251-
270
*/

/*    This is the implementation for ANSYS Fluent of the turbulent
heat transfer model presented in article [3] and [4].
      This implementation concerns only the thermal field, you can use
it with any k-e model.
      However the constants are setted for Pr=0.025 starting from a
flow field computed using the turbulence model (AKN) presented in
article [1].
      Thus the results obtained using a flow field computed using
other turbulence models might be not trustworthy.
      If Pr differs from 0.025 some changes are needed.
 */

/* Loading flow specification */
#include <udf.h>
#include <math.h>

/* Turbulence model constants for K_t and TDR_t*/
#define SIG_KT 1.4
#define SIG_DT 1.4
#define Cp1 0.925
#define Cp2 0.9
#define Cd1 1
#define C_EMME 0.3
#define C_LAMBDA 0.1
#define Prt_inf 0.9

typedef enum
{
```

```
 KT = 0,
 TDR_KT = 1,
 N_REQUIRED_UDS
}UDS_Scalars;

typedef enum
{
 TAU_U = 0,
 TAU_T = 1,
 P_KT = 2,
 ALPHA_T = 3,
 PR_T = 4,
 P_TKE = 5,
 SOURCE_Kt = 6,
 SOURCE_TDR_KT = 7,
 MUt = 8,
 tau_lT = 9,
 N_REQUIRED_UDM
}UDM_Memory;

#define C_Kt(c,t) C_UDSI(c,t,KT)
#define C_TDR_KT(c,t) C_UDSI(c,t,TDR_KT)
#define C_PKT(c,t) C_UDMI(c,t,P_KT)

/*********************************************************************
                        DEFINITIONS USEFUL QUANTITIES
*********************************************************************/

real ni(cell_t c, Thread *t)
{ return C_MU_L(c,t)/C_R(c,t); }

real alpha(cell_t c, Thread *t)
{ return C_K_L(c,t)/(C_R(c,t)*C_CP(c,t)); }

real Pr(cell_t c, Thread *t)
{ return ni(c,t)/alpha(c,t); }

real Re_d(cell_t c, Thread *t)
{ return C_WALL_DIST(c,t)*pow(C_D(c,t)*ni(c,t),0.25)/ni(c,t); }

real Re_t(cell_t c, Thread *t)
{ return SQR(C_K(c,t))/(ni(c,t)*C_D(c,t)); }

real tau_u(cell_t c, Thread *t)
{ return C_K(c,t)/C_D(c,t); }

real tau_t(cell_t c, Thread *t)
{ return C_Kt(c,t)/C_TDR_KT(c,t); }

real R(cell_t c, Thread *t)
{ return tau_t(c,t)/tau_u(c,t); }

real C_PTKE(cell_t c, Thread *t)
{ return C_UDMI(c,t,MUt)/C_R(c,t) * SQR(C_STRAIN_RATE_MAG(c,t)); }

/*********************************************************************
```

```
                        DAMPING FUNCTIONS
************************************************************************

real f_1a(cell_t c, Thread *t)
{ return (1.0-exp(-0.0714*Re_d(c,t))); }

/*Errata corrige Pr^(0.5) */
           real f_2a(cell_t c, Thread *t)
           { return (1.0-exp(-(0.0526*Re_d(c,t))*sqrt(Pr(c,t)))); }


real f1t(cell_t c, Thread *t)
{ return (f_1a(c,t)*f_2a(c,t)); }

real B1t(cell_t c, Thread *t)
{ return (tau_u(c,t)*Prt_inf); }

real f_2ao(cell_t c, Thread *t)
{ return (f1t(c,t)*exp(-4E-6*SQR(Re_t(c,t)))); }

/*Errata corrige Re_t instead of Re_d */
           real f_2bo(cell_t c, Thread *t)
           { return (f1t(c,t)*exp(-2.5E-5*SQR(Re_t(c,t)))); }

// /* Originale Manservisi*/
           // real f_2bo(cell_t c, Thread *t)
           // { return (f1t(c,t)*exp(-2.5E-5*SQR(Re_d(c,t)))); }

real f2tB2t(cell_t c, Thread *t)
{ return
tau_u(c,t)*(f_2ao(c,t)*(2.0*R(c,t)/(R(c,t)+C_EMME))+f_2bo(c,t)*sqrt(2
*R(c,t)/Pr(c,t))*(1.3/(sqrt(Pr(c,t))*pow(Re_t(c,t),0.75)))); }

real Cd2(cell_t c, Thread *t)
{ return SQR(1-exp(-0.1754*Re_d(c,t)))*(1.9*(1-0.3*exp(-
0.0237*SQR(Re_t(c,t))))-1); }


/*********************************************************************
                        DEFINE UDS SOURCES
*********************************************************************

DEFINE_SOURCE(KT_src,c,t,dS,eqn)
{
 real source = C_R(c,t) * (C_PKT(c,t) - C_TDR_KT(c,t));
 C_UDMI(c,t,SOURCE_Kt)=source;
 dS[eqn] = 0;
 return source;
}


DEFINE_SOURCE(TDR_KT_src_mans,c,t,dS,eqn)
{
 real source1 = (C_TDR_KT(c,t)/C_Kt(c,t))*(Cp1*C_PKT(c,t)-
Cd1*C_TDR_KT(c,t));
```

```
 real source2 = (C_TDR_KT(c,t)/C_K(c,t))*(Cp2*C_PTKE(c,t)-
Cd2(c,t)*C_D(c,t));
 real source = C_R(c,t)*(source1 + source2);
 C_UDMI(c,t,SOURCE_TDR_KT)=source;
 dS[eqn] = C_R(c,t)*((Cp2*C_PTKE(c,t)-
Cd2(c,t)*C_D(c,t))/C_K(c,t)+(Cp1*C_PKT(c,t))/C_Kt(c,t)-
2.0*C_TDR_KT(c,t)*(Cd1/C_Kt(c,t)));
 return source;
}


/*****************************************************************
                DEFINE UDS FLUXES AND DIFFUSIVITY

*****************************************************************
DEFINE_DIFFUSIVITY(keMANS_diffusivity,c,t,eqn)
{
      switch(eqn)
      {
            case KT:  return C_R(c,t)*(C_UDMI(c,t,ALPHA_T)/SIG_KT +
alpha(c,t)); break;
            case TDR_KT:  return C_R(c,t)*(C_UDMI(c,t,ALPHA_T)/SIG_DT
+ alpha(c,t)); break;
            default: return 0;
      }
}

DEFINE_UDS_FLUX(UDS_flux_keMANS, f, t, eqn)
{
      switch(eqn)
            {
            case KT: return F_FLUX(f,t); break;
            case TDR_KT: return F_FLUX(f,t); break;
            default: return 0;
            }
}

/*****************************************************************
                      ADJUST FUNCTIONS
*****************************************************************

DEFINE_ADJUST(adjust_keMANS,d)
{
      Thread *t;
      cell_t c;
      real tau_lu, tau_lt;
      real term1, term2, term3;

      thread_loop_c(t,d)
            if (FLUID_THREAD_P(t))
            {
                  begin_c_loop(c,t)
                        {
                              C_UDMI(c,t,TAU_U) = tau_u(c,t);
                              C_UDMI(c,t,TAU_T) = tau_t(c,t);
                              tau_lt = f1t(c,t)*B1t(c,t) + f2tB2t(c,t);
```

```
                              C_UDMI(c,t,tau_lT)=tau_lt;
                              C_UDMI(c,t,ALPHA_T) =
C_LAMBDA*C_K(c,t)*tau_lt;
                              C_UDMI(c,t,P_TKE) = C_PTKE(c,t);

                              if ( NULL != THREAD_STORAGE(t,SV_T_G) )
                                    { C_UDMI(c,t,P_KT) =
C_UDMI(c,t,ALPHA_T) * NV_MAG2(C_T_G(c,t)); }
                              else
                              {
                                    Message("\nAllocated temperature
gradients!\n");
                                    MD_Alloc_Storage_Vars(d, SV_T_RG,
SV_T_G, SV_NULL);
                                    C_UDMI(c,t,P_KT) =
C_UDMI(c,t,ALPHA_T) * NV_MAG2(C_T_G(c,t));
                              }
                              C_UDMI(c,t,PR_T) =
C_UDMI(c,t,MUt)/C_R(c,t)/C_UDMI(c,t,ALPHA_T);
                        }
                  end_c_loop(c,t)
                  }
}/* end of function */


/************************************************************************
                        DEFINE TURBULENT PRANDTL NUMBER
************************************************************************/

DEFINE_PRANDTL_T(pr_t_MANS,c,t)
{ return C_UDMI(c,t,PR_T); }


/************************************************************************
                        BOUNDARY CONDITIONS
************************************************************************/

DEFINE_PROFILE(TDR_KT_BC_CHF, t, i)
{
face_t f;
cell_t c0;
Thread *t0;

begin_f_loop(f,t)
      {
            t0 = THREAD_T0(t);
            c0 = F_C0(f,t);
            F_PROFILE(f,t,i) =
2.0*alpha(c0,t0)*C_Kt(c0,t0)/SQR(C_WALL_DIST(c0,t0));
      }
end_f_loop(f,t)
} /* end of function */


/************************************************************************
                              DEFINE ON DEMAND FUNCTIONS
```

```
************************************************************************

DEFINE_ON_DEMAND(check_UDS_UDM)
{
/*    Domain *d = Get_Domain(1);*/
      check_uds_udm();
}/* end of function */


/*    The thermal field must be computed performing few iteration with
a model already
      implemented in Fluent. Then this function is needed to
initialise all the quantities
      in order to perform the first iteration. */

DEFINE_ON_DEMAND(interpolation_energy)
{
Domain *d = Get_Domain(1);
Thread *t;
cell_t c;
real tau_lt;
real term1, term2;

thread_loop_c(t,d)
      {
            if (FLUID_THREAD_P(t))
            {     begin_c_loop(c,t)
                  {
                        C_UDSI(c,t,KT) = C_K(c,t);
                        C_UDSI(c,t,TDR_KT)=C_D(c,t);
                        C_UDMI(c,t,TAU_U) = tau_u(c,t);
                        C_UDMI(c,t,TAU_T) = tau_t(c,t);
                        C_UDMI(c,t,ALPHA_T) =
C_R(c,t)*C_UDMI(c,t,MUt)/0.85;
                        if ( NULL != THREAD_STORAGE(t,SV_T_G) )
                        {     C_UDMI(c,t,P_KT) = C_UDMI(c,t,ALPHA_T) *
NV_MAG2(C_T_G(c,t)); }
                        else
                        {
                              Message("\nAllocated temperature
gradients!\n");
                              MD_Alloc_Storage_Vars(d, SV_T_RG, SV_T_G,
SV_NULL);
                              C_UDMI(c,t,P_KT) = C_UDMI(c,t,ALPHA_T) *
NV_MAG2(C_T_G(c,t));

                        }
                              C_UDMI(c,t,PR_T) =
C_UDMI(c,t,MUt)/C_R(c,t)/C_UDMI(c,t,ALPHA_T);
                  }
            end_c_loop(c,t)
            }
      } /* end of thread_loop_c */

 Message("\nInterpolation successfully executed\n");
} /* end of function */
```

```
DEFINE_ON_DEMAND(instruction)
{
      Message("\nSome iteration with the energy equation enabled using
Prt=constant must be performed\n");
      Message("\nIf the flow field has been computed using UDS unload
this library and read first patchingTKEtdr.jou\n");
      Message("\nIn any case you must define %d UDM and read the file
patchingMUT.jou that patch the values of the turbulent viscosity in
udm-8 \n",N_REQUIRED_UDM);
      Message("\nYou must define %d UDS", N_REQUIRED_UDS);
      Message("\nDefine->user defined scalar->Flux-function:
UDS_flux_keMANS\n");
      Message("\nDefine->function Hooks: adjust_keMANS\n");
      Message("\nIf you start from the V2F model implemented in fluent
you must change the turbulence model (for example with a k-e one
because the v2f model doesn´t allow you to set a user-defined Energy
Pr Number\n");
      Message("\nModels->Energy Prandtl Number :pr_t_MANS\n");
      Message("\nMaterials->UDS diffusivity->user-
defined:keMANS_diffusivity\n");
      Message("\nCell-zone-condition->fluid->enable Sources Terms->
set UDS sources: (KT_src, TDR_KT_src)\n");
      Message("\nDefine->User-Defined->Execute-on-Demand->
interpolation_energy\n");
      Message("\nBoundary conditions-> wall-> UDS-> specified value
(KT=0, TDR_KT=TDR_KT_BC_CHF)\n");
      Message("\nBe careful the boundary conditions for the UDS at the
wall must be set to 'Specified Flux=0' before doing the
initialization.\nThey must be turned in to the right value after
performing the initialization\n");
      Message("\nYou can start from a solution of the thermal field
computed using the AKNT model (article [2]). In this case if UDS are
used to compute Kt and TDR-Kt no interpolation is needed. The
convergence is faster\n");
}
/*    Setting the boundary condition is always the last thing to do
because the UDS fields are initialized to values that
      do not fit the new boundary condition. Thus if the boundary
condition are setted before initialising the UDS fields
      a "Segmentation Fault" error will occur. *\




/************************************************************************
**                          AUXILIARY FUNCTIONS                         **
************************************************************************

void check_uds_udm(void)
{
/* Check for minimum defined UDS and UDM */

      if (n_uds < N_REQUIRED_UDS || n_udm < N_REQUIRED_UDM)
      {
```

```
                Message("nERROR: You must define at least %d UDS and
%d UDM\n", N_REQUIRED_UDS, N_REQUIRED_UDM);
                Internal_Error("Not enough UDSs defined\n");
      }
      else
      { Message("\nCheck completed succesfully.\nEnough UDS and/or UDM
allocated!\n"); }

} /* end of check_uds_udm */
```

Appendix B

User Defined Function to implement the Kays correlation in Paragraph 3.3.2 into the Fluent code.

```
#include <udf.h>
#include <math.h>


real ni(cell_t c, Thread *t)
{ return C_MU_L(c,t)/C_R(c,t); }

real alpha(cell_t c, Thread *t)
{ return C_K_L(c,t)/(C_R(c,t)*C_CP(c,t)); }

real Pr(cell_t c, Thread *t)
{ return ni(c,t)/alpha(c,t); }

DEFINE_PRANDTL_T(pr_t_KAYS,c,t)
{ return 0.85+0.7/(Pr(c,t)*C_MU_T(c,t)/C_MU_L(c,t)); }
```

Appendix C

Matlab script to implement the GCI study in Pragraph 5.2.1

```
% NB vectors must be already interpolated

function [a,b,c,d,e,f] = GCI(fi_3, fi_2, fi_1, n3, n2, n1, vol)

% a = extraapolated values
%b = GCI_2_1_fine all nodes
%c = percentual of converged nodes
%d = percentual of oscillatory nodes

%f1 f2 f3 variables
%n1 n2 n3 number of nodes



%%%%%%%%%%%%%%%%%%%%%%%%%%%% GCI SCRIPT %%%%%%%%%%%%%%%%%%%%%%%%%%%%

% volmume mesh
vol_mesh = vol;

% number of cells
n_cell_grid_3 = n3;
n_cell_grid_2 = n2;
n_cell_grid_1 = n1;

h_grid_3 = (vol_mesh / n_cell_grid_3)^(1/3);
h_grid_2 = (vol_mesh / n_cell_grid_2)^(1/3);
h_grid_1 = (vol_mesh / n_cell_grid_1)^(1/3);

r_2_1 = h_grid_2 / h_grid_1;
r_3_2 = h_grid_3 / h_grid_2;


epsilon_3_2 = (fi_3 - fi_2) ;
epsilon_2_1 = (fi_2 - fi_1) ;



nn = size(epsilon_3_2);
n = max(nn);


%used vectors
os_n = 0;
conv_n=0;
r_n=0;
```

```
os_nodes = zeros(1,n);
GCI_2_1_fine_os = zeros(1,n);
GCI_3_2_coarse_os = zeros(1,n);
GCI_2_1_fine_n = zeros(1,n);
GCI_3_2_coarse_n = zeros(1,n);

p = zeros(1,n);
iii=1;

% minimum value for epsilon
err = 1e-40;



% if os_nodes = 1 solution is oscillation if is = 2 epsilon32 or
epsilon 21
% are lower than err



for i = 1:n
    if ( abs(epsilon_3_2(i)) > err & abs(epsilon_2_1(i)) > err)


        s(i) = 1* sign(epsilon_3_2(i) / epsilon_2_1(i));


    fun = @(pp) (-pp + 1 / log(r_2_1) * abs(log(abs(epsilon_3_2(i) /
epsilon_2_1(i)) + log((r_2_1^(pp) - s(i)) / (r_3_2^(pp) - s(i))))));
    pp0 = 0.1;

    xx = fzero(fun , pp0);

    %bound 1 < xx < 2
    if (xx < 1)
        xx = 1;
    end
    if (xx > 2)
        xx = 2;
    end

    p(i) = xx;


    fi_2_1_ext(i) = (r_2_1^p(i) .* fi_1(i) - fi_2(i)) ./ (r_2_1^p(i)
- 1);
    fi_3_2_ext(i) = (r_3_2^p(i) .* fi_2(i) - fi_3(i)) ./ (r_3_2^p(i)
- 1);

    e_2_1_a(i) = abs((fi_1(i) - fi_2(i)) ./ fi_1(i));
    e_3_2_a(i) = abs((fi_2(i) - fi_3(i)) ./ fi_2(i));

    e_2_1_ext(i) = abs((fi_2_1_ext(i) - fi_1(i)) ./ fi_2_1_ext(i));
    e_3_2_ext(i) = abs((fi_3_2_ext(i) - fi_2(i)) ./ fi_3_2_ext(i));

    GCI_2_1_fine(i) = 1.25 .* e_2_1_a(i) ./ (r_2_1^p(i) - 1);
```

```
    GCI_3_2_coarse(i) = 1.25 .* e_3_2_a(i) ./ (r_3_2^p(i) - 1);

    else
      GCI_2_1_fine(i) = 0;
      GCI_3_2_coarse(i) = 0;

    end



    C0 = 1e-30;
    max_abs = max(max(abs([fi_1, fi_2, fi_3])));

    %richarrdson node index == 1
    %extrapolated curve only bild with richardson and converged nodes
    %oscillatory are set to 0 value
    if ((fi_1(i)/max_abs - fi_2(i)/max_abs) .* (fi_2(i)/max_abs  -
fi_3(i)/max_abs) > C0)
    os_nodes(i) = 1;
    extt(i) = fi_2_1_ext(i);
    pp(iii)=p(i);
    iii=iii+1;
    r_n = r_n + 1;
    end
    %converged node index == 2
    if(abs((fi_1(i)/max_abs - fi_2(i)/max_abs) .* (fi_2(i)/max_abs  -
fi_3(i)/max_abs)) < C0)
    os_nodes(i) = 2;
    extt(i)=fi_1(i);
    conv_n = conv_n + 1;
    end

    %oscillatory node index == 3
    if ((fi_1(i)/max_abs - fi_2(i)/max_abs) .* (fi_2(i)/max_abs  -
fi_3(i)/max_abs) < -C0)
        os_nodes(i) = 3;
      os_n = os_n + 1;
      extt(i)=0;
    end
end

GCI_2_1_fine;
GCI_3_2_coarse;
GCI_2_1_fine_os;
GCI_3_2_coarse_os;
GCI_2_1_fine_n;
GCI_3_2_coarse_n;
os_nodes;

p;

r_2_1;
r_3_2;


epsilon_2_1;
```

```
epsilon_3_2;

a = extt;
b = GCI_2_1_fine;
c = conv_n / n * 100;
d = os_n / n * 100;
e = pp;
f = r_n / n * 100;
end

%%%%%%%%%%%%%%%%%%%%%%%%%%%%%%%%%% END %%%%%%%%%%%%%%%%%%%%%%%%%%%%%%%%%%
```

List of figures

Fig. 1.1 THEADES LBE loop at KALLA laboratory, [9]. 4
Fig. 1.2 7 Wire wrapped rods in a hexagonal lattice, [11] the black arrow is the main flow direction 5
Fig. 1.3 Frontal view of the grid spacer used in [1]. 6
Fig. 2.1 Schematic representation of the THEADES LBE loop, its set-up for this experiment [1]. 7
Fig. 2.2 Side view of the test section from [1]. 8
Fig. 2.3 Exploded view of the test section [1]. 9
Fig. 2.4 Schematic representation of the thermocouples in the measuring plane upstream the three spacers [1]. 10
Fig. 2.5 Illustration of the influence of the Prandtl number on the magnitude of the viscous and thermal boundary layers in a two dimensional flow over a plate with constant wall temperature [16] 12
Fig. 2.6 Sketch of three dimensional energy spectra E(k) for velocity fluctuations and temperature fluctuations $E_T(k)$ in a forced channel flow at Pr<1, [18]. 15
Fig. 2.7 LES at $Re\tau = 2000$: Visualization of the instantaneous velocity field (top) θ field at Pr=0.01(middle) and at Pr=0.025(bottom) in an arbitrary x-y plane, all at the same time, [19]. 15
Fig. 2.8 Fluid packet moving in a 2D flow with $U2 = 0$ 16
Fig. 3.1 DNS data of u plus against y plus in a channel flow with $Re\tau = 640$ and Pr= 0.025, from the Kawamura database [21] 21
Fig. 3.2 DNS data of theta plus against y plus in a channel flow with $Re\tau = 640$ and Pr= 0.025, from the Kawamura database [21] 21
Fig. 3.3 Comparison of CFX results with test data in Mercury, [18]. 27
Fig. 4.1 Cartesian grid of a circle 31
Fig. 4.2 body fitted grid of a circle. 31
Fig. 4.3 Block-structured grid of a circle (5 blocks). 31
Fig. 4.4 Unstructured grid of a circle. 32
Fig. 4.5 Result of Nusselt number from the experimental campaign at KALLA laboratory, the line is the Mikityuk(2009) correlation for Nu in fully developed flow [1]. 34
Fig. 4.6 Result for Nusselt number moving the third spacer [1]. 34
Fig. 4.7 Longitudinal domain representation. 35
Fig. 4.8 Spacer rendering, only one rod is visible for displaying purpose, the red part is the domain. 36
Fig. 4.9 Mesh domain is the red fluid zone in Fig. 4.8. 36
Fig. 4.10 Block distribution from the mesh showed in Fig. 4.9. 36
Fig. 4.11 Quadrilateral cell in the x-y plane. 38
Fig. 4.12 Icem Aspect Ratio of the grid in Fig. 4.9. 38
Fig. 4.13 Icem, Quality criteria applied to the grid in Fig. 4.9. 38
Fig. 4.14 First structured spacer grid. 39
Fig. 4.15 Detailed grid of the bottom right corner of Fig. 4.14. 39
Fig. 4.16 detailed view of the highlighted area in Fig. 4.15. 40
Fig. 4.17 Icem mesh Quality criteria from the mesh showed in Fig. 4.14. 40

Fig. 4.18 spacer rendering with the new fluid domain which is the red part inside, rods are not displayed for viewing purpose. 41
Fig. 4.19 frontal grid view of the red fluid domain in Fig. 4.18Fig. 4.19. 41
Fig. 4.20 Detailed view of Fig. 4.19 contained in the red rectangular. 41
Fig. 4.21 Detailed view of Fig. 4.19 contained in the red rectangular, three central blocks are unstructured..... 42
Fig. 4.22 Icem mesh Quality from the mesh showed in Fig. 4.21. 43
Fig. 4.23 Icem Mesh Quality from the mesh showed Fig. 4.20. 43
Fig. 5.1 Ab, bc and cd lines on a triangular rod bundle lattice. 46
Fig. 5.2 Theta star, ab line Pe=360, p/d=1.3. 46
Fig. 5.3 Theta star bc line Pe=360, p/d=1.3. 46
Fig. 5.4 Theta star ab lin,e Pe=530, p/d=1.3. 46
Fig. 5.5 Theta star, bc line Pe=530 p/d=1.3. 46
Fig. 5.6 Theta star, ab line Pe=1470, p/d=1.3. 47
Fig. 5.7 5.8 Theta star, bc line Pe=1470 p/d=1.3. 47
Fig. 5.9 5.10 Turbulent Prandtl ab line Pe=360 p/d=1.3. 47
Fig. 5.11 Turbulent Prandtl line Pe=360 p/d=1.3. 47
Fig. 5.12 Turbulent Prandtl ab line Pe=530 p/d=1.3. 47
Fig. 5.13Turbulent Prandtl bc line Pe=530 p/d=1.3. 47
Fig. 5.14 Turbulent Prandtl ab line Pe=1470 p/d=1.3. 48
Fig. 5.15 Turbulent Prandtl bc line Pe=1470 $pd = 1.3$ 48
Fig. 5.16 R, ab line, p/d=1.3. 49
Fig. 5.17 R, bc line, p/d=1.3. 49
Fig. 5.18 Theta rsm, ab line, p/d=1.3 50
Fig. 5.19 Theta rsm, bc line, p/d=1.3. 50
Fig. 5.20 Dimensionless velocity against x plus ,Pe=1500, bc line, infinite rod bundle with spacer, z/Dh=-5. 51
Fig. 5.21 Turbulent viscosity ratio against x plus, Pe=1500, bc line infinite rod bindle with spacer, z/Dh=-5. 51
Fig. 5.22 theta star ab line Pe=1500, infinite rod bundle with spacer z/Dh=-5. 52
Fig. 5.23 Theta star bc line Pe=1500, infinite rod bundle with spacer, z/Dh=-5. 52
Fig. 5.24 Theta star, cd line, Pe=1500, infinite rod bundle with spacer, z/Dh=-5. 52
Fig. 5.25 Turbulent Prandtl ab line Pe=1500, infinite rod bundle with spacer, z/Dh=-5. 53
Fig. 5.26 Turbulent Prandtl number bc line Pe=1500, infinite rod bundle with spacer, z/Dh=-5. 53
Fig. 5.27 Theta star ab line v2f KAYS, infinite rod bundle with spacer, z/Dh=-5. 53
Fig. 5.28 Theta star bc line v2f KAYS, infinite rod bundle with spacer, z/Dh=-5. 53
Fig. 5.29 Theta star bc line v2f KAYS, infinite rod bundle with spacer, z/Dh=-5. 54
Fig. 5.30 Wall non-dimensional temperature profiles z-coordinate, Pe 1500 infinite rod bundle with spacer. 55
Fig. 5.31 Local Nusselt number Pe 1500, infinite rod bundle with spacer. 56
Fig. 5.32 Local Nusselt number Pe 500, infinite rod bundle with spacer. 57
Fig. 5.33 Local Nusselt number Pe 2500, infinite rod bundle with spacer. 58
Fig. 5.34 Nusslet number value on the green line intersection varying the Peclét number 59
Fig. 5.35 Nusselt k-epsilon AKN, k theta epsilon theta Pe=500. 62
Fig. 5.36 Nusselt with GCI bars k-epsilon AKN, k theta epsilon theta Pe=500. 62
Fig. 5.37 Nusselt k-epsilon AKN, k theta epsilon theta Pe=1500. 62

Fig. 5.38 Nusselt with GCI bars k-epsilon AKN, k theta epsilon theta Pe=1500. 62
Fig. 5.39 Nusselt k-epsilon AKN, k theta epsilon theta Pe=2500. 63
Fig. 5.40 Nusselt with GCI bars k-epsilon AKN, k theta epsilon theta Pe=2500. 63
Fig. 5.41 Nusselt k epsilon AKN KAYS Pe=1500. 63
Fig. 5.42 Nusselt with GCI bars k epsilon AKN KAYS Pe=1500. 63
Fig. 5.43 Nusselt k epsilon AKN CHENG Pe=1500. 63
Fig. 5.44 Nusselt with GCI bars k epsilon AKN CHENG Pe=1500. 63
Fig. 5.45 Nusselt k omega AKN KAYS Pe=1500. 64
Fig. 5.46 Nusselt with GCI bars k omega AKN KAYS Pe=1500. 64
Fig. 5.47 Nusselt k omega AKN CHENG Pe=1500. 64
Fig. 5.48 Nusselt with GCI bars k omega AKN CHENG Pe=1500. 64
Fig. 5.49 Nusselt v2f KAYS Pe=1500. 64
Fig. 5.50 Nusselt with GCI bars v2f KAYS Pe=1500. 64
Fig. 5.51 Nusselt v2f CHENG Pe=1500. 65
Fig. 5.52 Nusselt with GCI bars v2f CHENG Pe=1500. 65
Fig. 5.53 Spacer grid, rods are visible only inside the spacer for displaying purpose, the mesh is visible on a plane upstream and inside the spacer. 67
Fig. 5.54 Dimensionless velocity contour k-epsilon AKN, complete mesh. 69
Fig. 5.55 Turbulent viscosity ratio k-epsilon AKN, complete mesh. 69
Fig. 5.56 Dimensionless velocity profile k-omega SST, complete mesh. 69
Fig. 5.57 Turbulent viscosity ratio k-omega SST Pe 1500, complete mesh. 69
Fig. 5.58 Frontal rod bundle view with the red sampling lines. 70
Fig. 5.59 Dimensionless velocity profiles, complete mesh k-epsilon AKN. 71
Fig. 5.60 Turbulent viscosity ratio profiles, complete mesh, k-epsilon AKN. 71
Fig. 5.61 Dimensionless velocity profiles, complete mesh k-omega SST. 71
Fig. 5.62 Turbulent viscosity ratio profiles, complete mesh, k-omega SST. 71
Fig. 5.63 Theta star contour, k-epsilon AKN CHENG, complete mesh. 72
Fig. 5.64 Theta star contour, k-epsilon AKN KAYS, complete mesh. 72
Fig. 5.65 Theta star contour k-omega SST CHENG, complete mesh. 72
Fig. 5.66 Theta star contour k-omega SST KAYS, complete mesh. 72
Fig. 5.67 Theta star k-epsilon AKN CHENG ab lines, complete mesh. 73
Fig. 5.68 Theta star k-epsilon AKN KAYS bc lines, complete mesh. 73
Fig. 5.69 Theta star k-epsilon AKN KAYS ab lines, complete mesh. 73
Fig. 5.70 Theta star k-epsilon AKN KAYS bc lines, complete mesh. 73
Fig. 5.71 Theta star k-omega SST CHENG ab lines, complete mesh. 73
Fig. 5.72 Theta star k-omega SST CHENG bc lines, complete mesh. 73
Fig. 5.73 Theta star k-omega SST KAYS ab lines, complete mesh. 74
Fig. 5.74 Theta star k-omega SST KAYS bc lines, complete mesh. 74
Fig. 5.75 Dimensionless wall temperature, complete mesh. 75
Fig. 5.76 Local Nusselt number, complete mesh. 75
Fig. 5.77 Thermocouples scheme in (a) reported in the grid used in (b). 76

List of tables

Table 2.1 Geometrical parameter of the section test [1]. 9
Table 2.2 Proprieties of Air, Mercury, and Water at 20°C. 11
Table 5.1 Nusselt number varying the Péclet number and the models..... 49
Table 5.2 grids elements used in this thesis..... 62
Table 5.3 Nusselt number and their uncertainties in the measurement plane, from the mesh in Chapter(4.2.1) 66
Table 5.4 Under relaxation factors for the mesh descripted in Paragraph 4.2.2..... 68
Table 5.5 Complete mesh residuals. 68
Table 5.6 Nusselt numbers and dimensionless temperature confronted with the experimental data, complete mesh..... 76

Bibliography

[1] J. Pacio, M.Daubner, F.Fellmoser, K.Litfin, L.Marocco, R.Stieglitz, S. Taufall e Th.Wetzel, «Heavy-liquid metal heat transfer experimentin a 19-rod bundle with grid spacers,» *Nuclear Engineering and Design,* pp. 1-14, 2014.

[2] S. Manservisi e F. Menghini, «A CFD four parameter heat transfer turbulence model for engineering applicatios in heavy liquid metals,» *International Journal of Heat and Mass Transfer ,* vol. 69, pp. 312-326, 2014.

[3] X. Cheng e N. I. Tak, «CFD analysis of thermal-hydraulic behavior of heavy liquid metals in sub-channels,» *Nuclear Engineering and Design,* 2006.

[4] W. Kays, «Turbulent Prandtl Number - Where Are We?,» *Journal of Heat Transfer,* vol. 116, pp. 284-295, 1994.

[5] X. Cheng, A. Batta, G. Bnadini, F. Roelofs, K. Van Tichelen, A. Gerschenfeld, M. Prasser, A. Papukchiev, U. Hampel e W.M. Ma, «European activities on crosscutting thermal-hydraulic phenomena for innovative nuclear systems,» *Nuclear Engineering and Design,* pp. 1-3, 2015.

[6] W. Jaeger , M. Boettcher e V. H. Sanchez Espinoza, «Thermal-hydraulic evaluation of an LBE cooled 19-pin bundle in the frame of TRACE validation,» in *International COnference on Nuclear Engineering*, Chengdu, 2013.

[7] T. Abram e S. Ion, «Generation-IV nuclear power: A review of the state of the science,» *Energy Policy,* pp. 1-2, 2008.

[8] IAEA, «Development of Innovative Nuclear Tecnology,» in *General Conference*, 2004.

[9] T. Wetzel, «KArlsruhe Liquid Metal LAboratory, KALLA,» IKET, [Online]. Available: www.iket.kit.edu/english/140.php.

[10] B.F. Gromov, Yu.S. Belomitcev, E.I. Yefimov, M.P. Leonchuk, P.N. Martinov, YU.I. Orlov, D.V. Pankratov, Yu.G. Pashkin, G.I. Toshinsky, V.V. Chekunov, B.A. Shmatko e V.S. Stepanov, «Use of lead-bismuth in nuclear reactors and accelerator-driven systems,» *Nuclear Engineeering and Design,* pp. 1-2, 1997.

[11] T. Sreenivasulu e BVSSS Prasad, «Flow and Heat Transfer Characteristics in a Seven TubeBundle,» *International Journal of Advancements in Technology ,* pp. 350-381, 2011.

[12] N. Govindha Rasu, K. Velusam, T. Sundararajan e P. Chellapandi, «Simultaneous development of flow and temperature fields in wire-wrapped fuel pin bundles of sodium cooled fast reactor,» *Nuclear Engineering and Design,* vol. 267, pp. 44-60, 2014.

[13] C.C. Liu, Y.M. Ferng e C.K. Shih, «CFD evaluation of turbulence models for flow simulation of the fuel rod bundle with spacer assembly,» *Applied Thermal Engineering,* vol. 40, pp. 389-396, 2012.

[14] W. Jaeger e V. Sànchez, «Validation of the heat transfer enhancement models for spacer grids in the system code TRACE,» *Nuclear Engineering and Design,* vol. 265, pp. 272-287, 2013.

[15] S. Manservisi e F. Menghini, «Triangular rod bundle simulations of a CFD k epsilon k-theta epsilon-theta heat transfer turbulence model for heavy liquid metals,» *Nuclear Engineering and Design,* pp. 5-7, 2014.

[16] R. Stieglitz, «Low prandtl number thermal hydraulics,» in *Handbook on Lead-bismuth Eutectic and lead properties, Material Compatibility, Thermal Hydraulics and Technologies*, NEA Nuclear Energy Agency, OECD Organization for Economic Co.Operation and Development, 2007, pp. 399-478.

[17] H. K. Versteeg e W. Malalasekera, An Introduction to Computational Fluid Dynamics, Harlow: Edinburgh Gate, 2007.

[18] G. Grötzbach, «Challenges in low-Prandtl number heat transfer simulation and model,» *Nuclear Engineering and Design,* vol. 264, pp. 41-55, 2013.

[19] M. Duponcheel, L. Bricteux, M. Manconi, G. Winckelmans e Y. Bartosiewicz, «Assessment of RANS and improved near-wall modeling for forced convection at low Prandtl numbers based on LES up to Ret=2000,» *International Journal of Heat and Mass Transfer,* vol. 75, pp. 470-482, 2014.

[20] S. B. Pope, Turbulernt Flows, Cambridge: Cambridge Univesity Press, 2011.

[21] H. Abe e H. Kawamura, «Direct Numerical Simulation Data Base for Turbulent Channel Flow with Heat Transfer,» Tokyo University of Science, Tokyo, 2004.

[22] K. Abe, T. Kondoh e Y. Nagano, «A new turbulence model for preedicting fluid flow and heat transfer in separating and reattaching flows,» *Internationa Journal of Heat and Mass transfer,* vol. 37, pp. 139-151, 1994.

[23] ANSYS, ANSYS Fluent V2F Turbulence Model Manual, Canonsburg: ANSYS, Inc., 2013.

[24] Y. Nagano e M. Shimada, «Development of a two-equation heat transfer model based on direct numerical simulation of turbulent flows with different Prandtl numbers,» *Physics of Fluids,* vol. 8, pp. 3379-3402, 1996.

[25] M. W. Maresca e O. E. Dwyer, «Heat transfer to mercury flowing in-line through a boundle of circular rods,» *Journal of Heat Transfer,* vol. 86, pp. 180-186, 1964.

[26] A. Inc, «ANSYS ICEM CFD Help Manual,» Southpointe, Canonsburg, 2013.

[27] Roache P. J., «Verification of Codes and Calculations,» *AIAA,* vol. 5, pp. 696-702, 1998.

[28] Ismail Celik e Ozgur Karatekin, «Numerical Experiment on Application of Richardson Extrapolation with Nonuniform Grids,» *Journal of Fluids Engineering ,* vol. 119, pp. 584-590, 1997.

[29] J. Cadafalc, C. D. Pérez-Segarra, R. Consul e A. Oliva, «Verification of Finite Volume Computations on Steady-State Fluid Flow and Heat Transfer,» *Journal of Fluids and Engineering,* vol. 124, pp. 11-21, 2002.